Roll, Pitch and Yaw Torque Control for a Robotic Bee

Citation	Finio, Benjamin. 2012. Roll, Pitch and Yaw Torque Control for a Robotic Bee. Doctoral dissertation, Harvard University.
Accessed	April 17, 2018 3:28:45 PM EDT
Citable Link	http://nrs.harvard.edu/urn-3:HUL.InstRepos:9920663
Terms of Use	This article was downloaded from Harvard University's DASH repository, and is made available under the terms and conditions applicable to Other Posted Material, as set forth at http://nrs.harvard.edu/urn-3:HUL.InstRepos:dash.current.terms-of-use#LAA

Thesis advisor | Author

Robert J. Wood | **Benjamin Michael Finio**

Roll, Pitch and Yaw Torque Control for a Robotic Bee

Abstract

In the last decade, the robotics community has pushed to develop increasingly small, autonomous flapping-wing robotic vehicles for a variety of civilian and military applications. The miniaturization of these vehicles has pushed the boundaries of technology in many areas, including electronics, artificial intelligence, and mechanics; as well as our understanding of biology. In particular, at the insect scale, fabrication, actuation, and flight control of a flapping-wing robot become especially challenging. This thesis addresses these challenges in the context of the "RoboBee" project, which has the goal of creating an autonomous swarm of at-scale robotic bees. A 100mg robot with a 3cm wingspan capable of generating roll, pitch and yaw torques in the range of $\pm 1\mu$Nm by using a large, central power actuator to flap the wings and smaller control actuators to steer is presented. A dynamic model is used to predict torque generation capabilities, and custom instrumentation is developed to measure and characterize the vehicle's control torques. Finally, controlled flight experiments are presented, and the vehicle is capable of maintaining a stable pitch and roll attitude during ascending vertical flight. This is the first successful controlled flight of a truly insect-scale flapping-wing robot.

Contents

Acknowledgments

First, I must thank Prof. Robert Wood for being both an excellent advisor and a friend, and for admitting me to the Harvard Microrobotics Lab in its formative years. None of what I've accomplished would have been possible without his efforts to establish himself in the field prior to my arrival. I also owe many thanks to the generations of graduate students before him, his advisor Ron Fearing and his other colleagues at U.C. Berkeley for laying the foundations that allowed the field of microrobotics to reach the point it has today. Feedback from my committee, Profs. Conor Walsh, Stacey Combes, and L. Mahadevan has also proven invaluable in developing this thesis into its final form.

Second, I would like to thank all the members of the Harvard Microrobotics Lab, without whom this entire experience (both academic and personal) would have been much less rewarding. They have all been with me through both the highs and lows of the last five years, sharing in both the excitement and the frustration of the research process. The efforts of Hetchen Ehrenfeld and Mike Smith have saved me countless hours and headaches over the years. The results presented in this thesis would not have been possible without the fabrication process developed by Peter Whitney and Pratheev Sreetharan, design and fabrication support from Kevin Galloway, nearly constant troubleshooting and technical support from Mike Karpelson regarding all things electronic, and support from Katie Hoffman and Rebecca Kramer on all graduate-school related crises.

Finally, I could not have done this without support from all of those in my life outside of the lab. I would not be where I am today without the constant love and support I have had from my parents and grandparents over the last 25 years. My

roommate Andrew has provided a daily much-needed reality check upon my return from lab, my dog Bruce has always greeted me with a wagging tail even after a catastrophic day of failed experiments, and my brother Nick a constant sense of humor and reminder that engineers do not, in fact, rule the world. Finally, my girlfriend Erin has been with me the entire way through this process - and I hope she can say that there has been some apparent improvement between my undergraduate thesis and this one.

To my parents - without their love and support over the last 25 years, I never would have made it this far.

Chapter 1

Introduction and Motivations

1.1 Background

Over the last century, humankind has mastered flight in the realm of large-scale machines such as airplanes, helicopters, and rockets. It is not until the last decade that, inspired by agile natural fliers such as bats, birds and insects, we have started to pursue the creation of small-scale flying machines. This has driven engineers to work closely with biologists and given rise to the field of biologically-inspired engineering. The seminal works of Ellington [38], Dudley [35], and Dickinson [31, 46] laid out the fundamental understanding of the aerodynamics and biomechanics of insect flight that has allowed engineers to understand and reverse-engineer these remarkably complex systems.

Several fully-operational flapping-wing micro air vehicles (FWMAVs) have recently been developed, notably the Festo Smartbird [41], Aerovironment Nano Hummingbird [56], and the Delft University Delfly [26]. These vehicles are shown in Fig.

(a) (b) (c)

Figure 1.1: Recently developed flapping-wing micro air vehicles (FWMAVs) include (a) the Festo Smartbird [41], the Aerovironment Nano Hummingbird [56], and the Delfly [26].

1.1. While subject to stringent weight requirements and various engineering design challenges, these vehicles are large enough that they can rely on traditional mechanical components such as DC motors and gears for actuation and operation, as well as carrying small off-the-shelf electrical components like lithium-ion batteries, radio transmitters, and microprocessors.

Development of an insect-scale vehicle presents additional design challenges, as the vehicle becomes too small for traditional macro scale components, but still too large for truly microscopic processes such as those used for microelectromechanical systems (MEMS). The Harvard RoboBee project seeks to develop a swarm of autonomous, insect-scale flapping-wing robots - this requires innovation in all related areas including fabrication, control, actuation and power electronics. A recent prototype of the vehicle is shown in Fig. 1.2. To emphasize the sense of scale and the resulting engineering challenges, the RoboBee is compared to the three previously mentioned FWMAVs in Table 1.1.

A general goal in the field of robotics is to use robots for things that are “dull, dirty and dangerous” for humans to do. This includes numerous tasks ranging from civilian operations such as environmental monitoring and crop pollination, to military and law

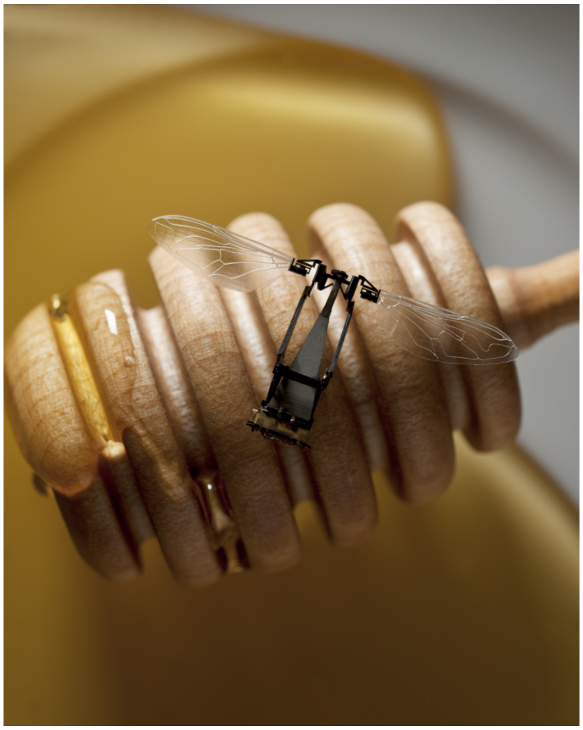

Figure 1.2: A RoboBee prototype from 2011. Photo courtesy of Christopher Harting.

enforcement operations such as surveillance, security, and direct combat operations. Larger robots such as the iRobot packbot [51] are already widely used for such tasks. While the idea that a large number of small, cheap robots could more effectively explore an area since a swarm will be robust to failure of individual robots was originally proposed over two decades ago [21], such robot swarms have yet to make it out of the lab and into the field. This thesis does not directly address potential applications for the RoboBee. Instead, we seek to develop a versatile platform that could be applied in different scenarios by different users. More information about potential applications can be found in government grant program announcements [5] and concept videos [60].

Table 1.1: Recently developed FWMAVs

Vehicle	Smartbird	Nano Hummingbird	Delfly Micro	RoboBee
Developer	Festo	Aerovironment	Delft University	Harvard
Mass (g)	450	19	3	0.1
Wingspan (cm)	200	16.5	10	3

1.2 Thesis Statement and Contribution

This dissertation focuses on the mechanical design, actuation and fabrication of a RoboBee prototype that is capable of controlled, free flight. To date this is the first vehicle of this scale capable of directly controlling all three body torques (roll, pitch and yaw) and using flapping wing motions to stabilize flight.

1.3 Thesis Outline

The remainder of this chapter presents a brief overview of insect flight that will be useful to any reader not familiar with the subject. A brief overview of prior work in the development of insect-sized FWMAVs, primarily at the Harvard Microrobotics Lab and the Berkeley Biomimetic Millisystems lab, is also included. The rest of the thesis is broken down as follows:

- Chapters 2 and 3 present mechanical designs, analysis and preliminary testing of RoboBee designs that use wing motions to steer.
- Chapter 4 presents a linearized dynamic model that is used as a design tool and to better understand experimental data.
- Chapter 5 presents the detailed design, analysis and fabrication of a custom

micro torque sensor used for characterization of RoboBee prototypes.

- Chapter 6 presents open-loop torque measurements and the first free-flight steering maneuvers of the RoboBee.
- Chapter 7 presents closed-loop controlled flight experiments.

1.4 Insect Flight

The basic mechanism of flapping-wing flight in Dipteran insects is shown in Fig. 1.3. The motion of insect wings during hover resembles a back-and-forth paddling motion more so than the up-and-down motion we typically envision when thinking of more familiar avian flight. The wings translate at a high angle of attack and rapidly flip at the end of each stroke (typically in the range of 100's of Hz for a RoboBee-sized vehicle, with stroke amplitudes exceeding 100°), allowing them to generate lift in both directions of flapping. The degrees of freedom used to parameterize this motion are defined in Fig. 1.4. In robotics the stroke plane deviation angle θ is frequently ignored and the wing is assumed to flap in a plane, as this greatly simplifies the flapping mechanism (a design for actuated stroke-plane deviation is discussed in Appendix B). For a thorough and detailed analysis of the aerodynamics of flapping-wing flight, the interested reader is referred to [38] and [31].

Beyond the basic mechanism for lift generation, two additional elements are crucial for understanding insect flight and reproducing it mechanically: the muscle structure that drives the wings, and how the insect uses its muscle-wing system to stabilize and maneuver. In the case of Dipteran insects, muscles are divided into two morpho-

Figure 1.3: Artist's rendering of a Dipteran insect in hovering flight. The wings flap back and forth in an approximately horizontal plane while rotating about their spanwise axes, generating lift in both directions of the stroke. The wings flap from the head toward the abdomen on the "upstroke", and from the abdomen toward the head on the "downstroke".

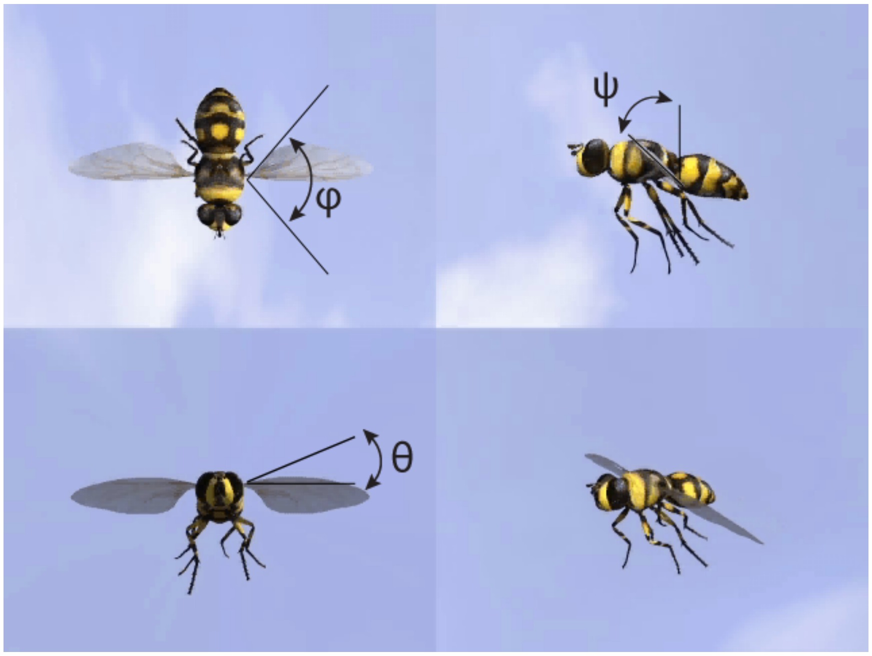

Figure 1.4: The three degrees of freedom typically used to parameterize flapping wing motion. The *stroke angle* ϕ defines the forward-and-backward flapping of the wing, the *rotation angle* ψ the rotation of the wing about its longitudinal axis (roughly coincident with the leading edge depending on the shape of the wing), and the *deviation angle* θ defines the angle of the wing relative to a flat, horizontal stroke plane.

logically and functionally distinct groups: power muscles and control muscles [30]. Contained within the thorax, the power muscles drive the wings at the resonant frequency of the combined muscle-thorax-wing system, but do so symmetrically, and are not used for steering. Smaller, lower-power control muscles are directly connected to the wing root and can fine-tune wing motions that result in asymmetric wing motions, leading to the generation of net body torques and allowing the insect to steer. While it appears that many insects use secondary mechanisms such as moving their abdomen and legs to shift their center of mass and aerodynamic drag profile, asymmetric wing kinematics are the *primary* mechanism by which insects maneuver. Several studies such as [46], [85] and [36] investigate this phenomenon in greater detail.

1.5 Prior Work

The RoboBee project at Harvard was preceded by the Micromechanical Flying Insect (MFI) Project at the U.C. Berkeley Biomimetic Millisystems Lab [77, 27, 29, 28, 98, 40, 9, 78]. They pioneered many technologies vital to the developing field of microrobotics, including a composite manufacturing method that relied on flexures for moving joints [8, 94] and piezoelectric materials for actuation [22, 97]. The result was a two-winged vehicle with four actuators, one for each degree of freedom of each wing (Fig. 1.5). This allowed independent drive of each wing's flapping angle ϕ and rotation angle ψ. While in theory this vehicle should have been fully controllable, difficulties with dynamic coupling between the wing degrees of freedom, along with limitations of the fabrication process at the time, lead to underperformance and the vehicle could not generate sufficient thrust to lift its own weight. Despite this, the

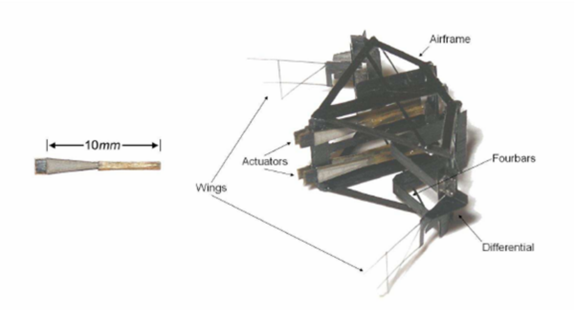

Figure 1.5: An MFI prototype from 2003 (image courtesy of the Berkeley Biomimetic Millisystems Lab). Two wings are driven through a transmission mechanism by four total piezoelectric actuators, with all components mounted on a carbon fiber airframe.

project laid the foundations for the work that followed at Harvard.

In 2007, Biomimetic Millisystems Lab alumnus Prof. Robert Wood took a new approach to vehicle design at the newly founded Harvard Microrobotics Lab. He redesigned the vehicle such that the flapping motion ϕ of both wings was driven by a single piezoelectric actuator through a mechanical transmission, and the rotation ψ was entirely passive. Each wing rests on a hinge that acts as a torsional spring, allowing it to rotate as a result of inertial and aerodynamic forces during flapping. While this approach has the advantage of simplifying mechanical design, fabrication, and operation of the device, it does not leave enough controlled degrees of freedom for controllable free flight. Thus, the vehicle was able to lift off with external power, but was constrained to two vertical guide wires that restricted any rotational motions, artificially stabilizing the flight. The details about the design, fabrication, testing and first flight of the Harvard Microrobotic Fly are presented in [92, 91, 93]. A labeled schematic and photograph of the fly are shown in Fig. 1.6. A schematic of a piezoelectric actuator, a key component of the design, is shown in Fig. 1.7. The work leading up to this dissertation began in 2007 with the Harvard Microrobotic

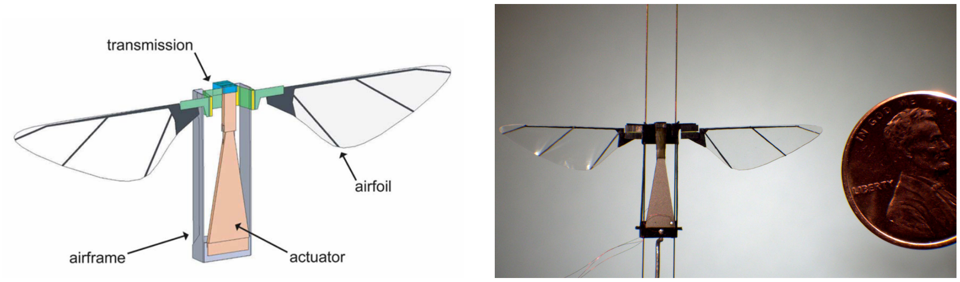

Figure 1.6: (left) A labeled diagram of the Harvard Microrobotic Fly. Both wings are driven by a single piezoelectric actuator through a transmission mechanism. (right) A prototype fly from 2007 mounted on two vertical guidewires for liftoff tests.

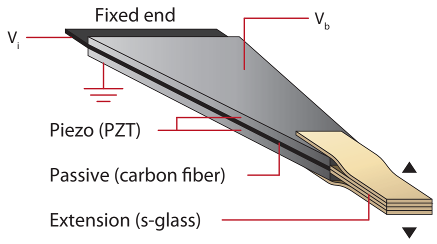

Figure 1.7: Electromechanical schematic for a typical cantilever bimorph piezoelectric actuator. The actuator is mechanically grounded at the proximal end, resulting in motion of the distal end when a signal voltage V_i is applied to the center electrode. Constant bias V_b and ground voltages are applied to the top and bottom electrodes.

Fly as the current state-of-the art, with the goal of maintaining the simplicity of the original design, but reintroducing some mechanism for controllability, inherent in the Berkeley MFI design.

1.6 A note on the structure of this thesis

The content of this thesis is drawn almost entirely from the following publications.

- Chapter 2: *Body torque modulation for a microrobotic fly*, B. Finio, J. Shang, and R.J. Wood. IEEE International Conference on Robotics and Automation, 2009.

- Chapter 3: *Asymmetric flapping for a robotic fly using a hybrid power-control actuator*, B. Finio, B. Eum, C. Oland, and R.J. Wood. IEEE/RSJ International Conference on Intelligent Robots and Systems, 2009.

- Chapter 4: *System identification and linear time-invariant modeling of an insect-sized flapping-wing micro air vehicle*, B. Finio, N.O. Perez-Arancibia, and R.J. Wood. IEEE/RSJ International Conference on Intelligent Robots and Systems, 2011.

- Chapter 5: *An ultra-high precision, high bandwidth torque sensor for microrobotics applications*, B. Finio, K.C. Galloway, and R.J. Wood. IEEE/RSJ International Conference on Intelligent Robots and Systems, 2011.

- Chapter 6: *Open-loop roll, pitch and yaw torques for a robotic bee*, B. Finio and R.J. Wood. IEEE/RSJ International Conference on Intelligent Robots and

Systems, 2012. (submitted and under review as of May 2012)

In some of the earlier publications, the axis convention for roll and yaw torques was reversed. This convention has been edited in this thesis to be consistent with the most recent publications throughout the entire document. The published versions of the earlier chapters also refer to my design as a "new" version of the Harvard Microrobotic Fly, whereas later papers refer to it as the "RoboBee". For consistency, in this document the Harvard Microrobotic Fly refers to Prof. Robert Wood's design from 2007, and RoboBee is used to refer to my design.

Chapter 2

Mechanism Design

2.1 Introduction

This chapter presents initial design of the RoboBee, featuring modifications of the original Harvard Microrobotic Fly (HMF) design to control roll torques with asymmetric wing amplitudes. The results presented here include measured wing kinematics and predicted torques based on an aerodynamic model. However, a direct mechanism for measuring these torques had not been developed at the time. For actual torque measurements, see Chapter 6.

While much work has been done to develop and simulate control algorithms for the Berkeley MFI [77, 27, 29, 28], preliminary work on the Harvard Microrobotic Fly focused on achieving liftoff by minimizing weight and maximizing the propulsive efficiency. Since both wings are driven by the same power actuator and a symmetric 1-DOF mechanical transmission, flapping is ideally symmetric (though manufacturing imperfections exist) and thus only pitch torque can be controlled directly (explained in Chapter 5). The convention for roll, pitch and yaw axes in the body frame is defined in Fig. 2.1. As a step toward developing control laws for stable hovering, it is desirable to develop a method to independently modulate the trajectory, and thus the resulting forces, of each wing while continuing to utilize passive rotation and thus avoiding the need for additional power actuators. One possible solution is the introduction of two "control" actuators, to change the 1-DOF transmission to 3-DOF (Fig. 2.2), creating a 5-DOF system (one power, two control, two passive). A single power actuator will still act as the primary source of mechanical power for flapping, while two control actuators modify transmission kinematics independently, creating asymmetries in wing motion. The small displacement of the wing pivot required to alter the wing kinematics implies that the control actuators can be significantly lower power and mass than the power actuator. This actuation method is directly analogous to Dipteran thoracic mechanics, in which large indirect power muscles are the primary source of mechanical energy, and small adjustments to the thorax are made using direct control muscles for steering purposes [30]. The approach of using separate power and control actuators is also seen in larger-scale mechanical vehicles (e.g. the steering wheel of a car and control surfaces on an airplane are separate from the engines responsible for primary drive or thrust generation).

2.2 Kinematics

Since the transmission is symmetric, it is sufficient to derive the forward kinematics for only one side, mapping the linear input from the power actuator to the flapping motion of the wing. This was first done by Wood in [91] and is expanded here to

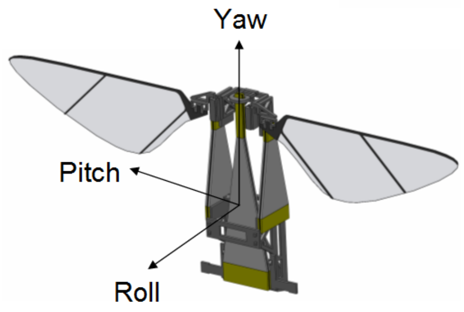

Figure 2.1: The roll, pitch and yaw axis convention used throughout this thesis.

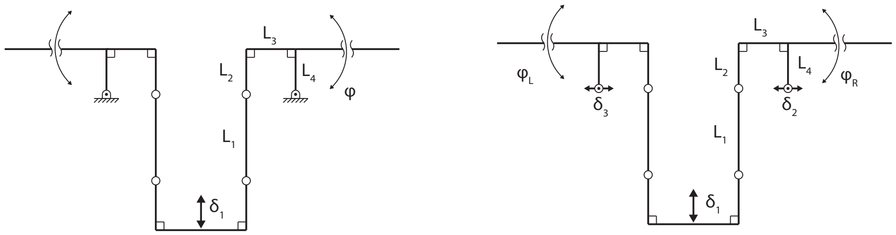

(a)

(b)

Figure 2.2: In the original microrobotic fly design, both wings are driven by a single power actuator δ_1 through a 1-DOF symmetric transmission, resulting in symmetric flapping ϕ (a). The pivots at the base of each wing are connected to ground, i.e. the airframe. In the proposed design, the wing pivots are connected to two new control actuators (which are then connected to ground) - creating control inputs δ_2 and δ_3 (b). This allows independent modulation of each side of the transmission.

include the second input from the control actuator. Thus, the stroke angle of the wing, θ_w, can be given explicitly as a function of the two linear actuator inputs, δ_1 and δ_2 (power and control, respectively - note the sign conventions that positive θ_w corresponds to positive δ_1, and δ_2 is positive outward away from the vehicle center of mass). Note that in [91], L_2 and L_4 are assumed to be equal, so the expression presented here is somewhat more complicated:

$$\begin{aligned}\phi = -\frac{\pi}{2} + \arccos\Bigg[& \Big((L_3+\delta_2)^2 + (L_1+L_2-L_4-\delta_1)^2 \\ & + L_3^2 + (L_2-L_4)^2 - L_1^2\Big)\Bigg(2\sqrt{L_3^2+(L_2-L_4)^2}\times \\ & \sqrt{(L_3+\delta_2)^2+(L_1+L_2-L_4-\delta_1)^2}\Bigg)^{-1}\Bigg] \\ & + \arctan\left(\frac{L_3+\delta_2}{L_1+L_2-L_4-\delta_1}\right) \\ & + \arctan\left(\frac{L_2-L_4}{L_3}\right) \qquad (2.1)\end{aligned}$$

where L_i are the respective link lengths as shown in Fig. 2.2.

In [91], the primary design consideration was maximizing the total stroke angle in order to maximize lift. Transmission geometry was optimized to give maximum stroke angle for a given linear actuator input (note that this approach does not properly account for dynamic effects, this mistake is addressed in Chapter 4). A secondary goal is dorsoventrally symmetric flapping, meaning that the mean stroke angle is approximately zero. This ensures that the center of lift vector (averaged over one wing stroke) for the two wings intersects with the body's center of mass, preventing undesired generation of a net pitch torque (Fig. 2.3a). With a single actuator, the total and mean stroke angles could be adjusted for both wings symmetrically by

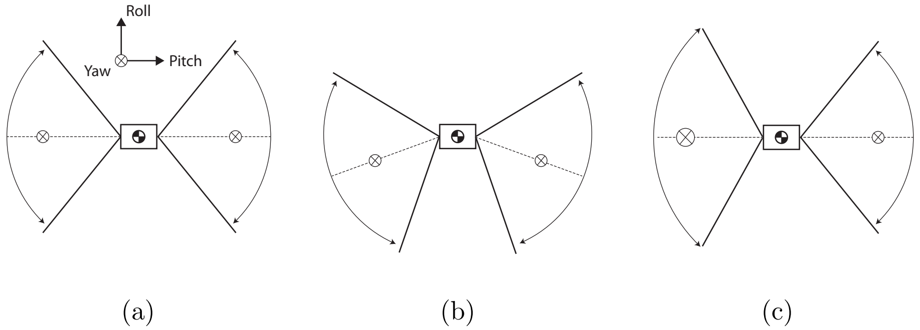

Figure 2.3: In the first generation design (a), the center of lift could be shifted forward or backward relative to the body's center of mass to create pitch torques (b). With the addition of control actuators, lift forces on each wing can be modulated asymmetrically to generate roll torques (c).

changing the amplitude and DC offset, respectively, of the driving voltage signal (see [97] for details). This allowed modulation of the thrust vector and torque about the pitch axis only (Fig. 2.3b).

The introduction of a second degree of freedom to each side of the transmission allows coupled modulation of both stroke amplitude and mean stroke angle. The lift force on a wing will increase with wing velocity (Eqs. 2.15-2.15), so it follows that increasing stroke amplitude while holding frequency constant will increase lift (conversely, increasing frequency with fixed amplitude will also increase wing velocity and thus increase lift). This means that asymmetrically changing the wing stroke amplitudes will create asymmetric lift forces, and thus a net body torque about the roll axis (Fig. 2.3b). It will be shown later that control actuator motion has a much larger effect on total stroke angle than mean stroke angle, and thus can effectively be used to control torques about the roll axis independent of the pitch torque. In conjunction with changing the DC offset of the power actuator signal to control torques about the pitch axis, this gives controllability of torques about two of the three body axes. The generation of yaw torque requires an additional mechanism such as control over the relative phase of wing rotation, or “split-cycle” flapping where the wings flap with asymmetric velocities on the upstroke and downstroke. Yaw torques are addressed in Chapter 6.

As a design parameter for the new transmission, it is useful to define another quantity in addition to the transmission ratio – the control power C. This is defined as the *change* in total stroke angle per unit displacement of the control actuator:

$$C = \frac{\triangle\theta_{total}}{\delta_2} \tag{2.2}$$

In addition to maximizing the transmission ratio to achieve higher lift, it is also desirable to maximize the control power. It is shown in [91] that T depends primarily on L_3^{-1}; thus, as a starting point for the new design, L_3 is minimized in order to maximize T (the lower bound being 300μm due to manufacturing limitations). It can be seen in (2.1) that (a) the kinematics are scale-invariant and (b) only the relative value $L_2 - L_4$, not the absolute value of L_2 or L_4, is significant. Therefore C can be calculated as a function of two nondimensional variables, $\frac{L_1}{L_3}$ and $\frac{L_2-L_4}{L_3}$, assuming a fixed power actuator input $\pm\delta_1$ and control actuator range $\pm\delta_2$. The objective is then to find the maximum absolute value of C and choose the corresponding transmission geometry (Fig. 2.4). The peak in the plot indicates that the transmission will pass through a singularity, which is undesirable. Therefore, designs near the peak are avoided, despite the relatively large value of C. The following geometry is selected to give $|C| \approx 2000$ rad·m^{-1}: $L_1 = 400\mu$m, $L_2 = 300\mu$m, $L_3 = 300\mu$m, and $L_4 = 450\mu$m.

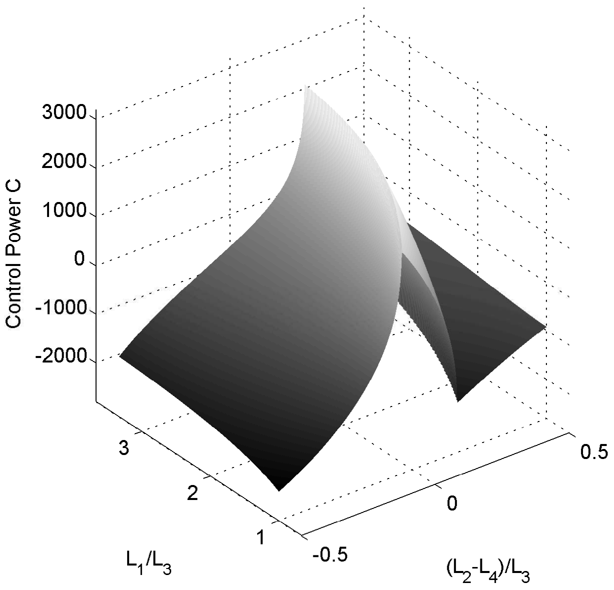

Figure 2.4: Control power C is plotted as a function of nondimensional transmission geometric parameters L_1/L_3 and $(L_2 - L_4)/L_3$, with fixed actuator inputs $\pm\delta_1$ and $\pm\delta_2$.

Once the transmission design is selected, (2.1) can be used to calculate the expected wing trajectory over fixed ranges for the power and control actuators (Fig. 2.5). The kinematics predict that, holding power actuator input constant at $\pm 300\mu$m, a change in total stroke angle of $\sim 30°$ can be achieved with $\pm 100\mu$m control actuator motion.

Based on the selected transmission geometry, actuators can be designed to generate the desired total stroke angle (120°, the value obtained with the original HMF). Actuator geometry can be selected based on the model shown in [97] to give the desired displacement, stiffness, and blocked force while minimizing mass and thus optimizing energy density. The actuators used here are over-designed to have a larger force and displacement than is required, allowing the device to serve as a robust

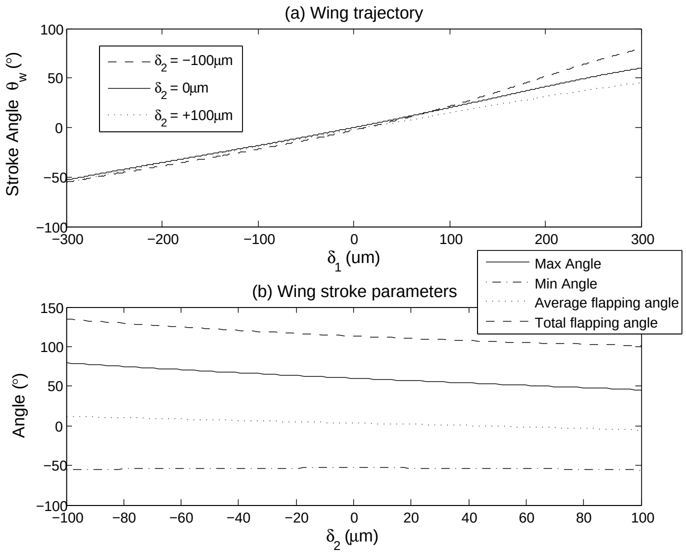

Figure 2.5: Wing angle as a function of power actuator displacement δ_1 for various fixed δ_2 (a); maximum, minimum, mean and total stroke angles for a range of δ_2 and fixed $\delta_1 = \pm 300\mu$m (b).

Table 2.1: Power and control actuator design parameters.

	Power Actuator	Control Actuator
Mass (mg)	143	41
$\pm\delta_1$ (μm)	415	110
k (N/m)	514	2094
F_b (mN)	430	473

testbed for this new actuation method. The power and control actuators are shown in Fig. 2.6, and the relevant design parameters are shown in Table 2.1.

2.3 Dynamics

While the transmission kinematics are a useful design tool, they assume the power actuator acts as a linear displacement source. While the unloaded actuator tip dis-

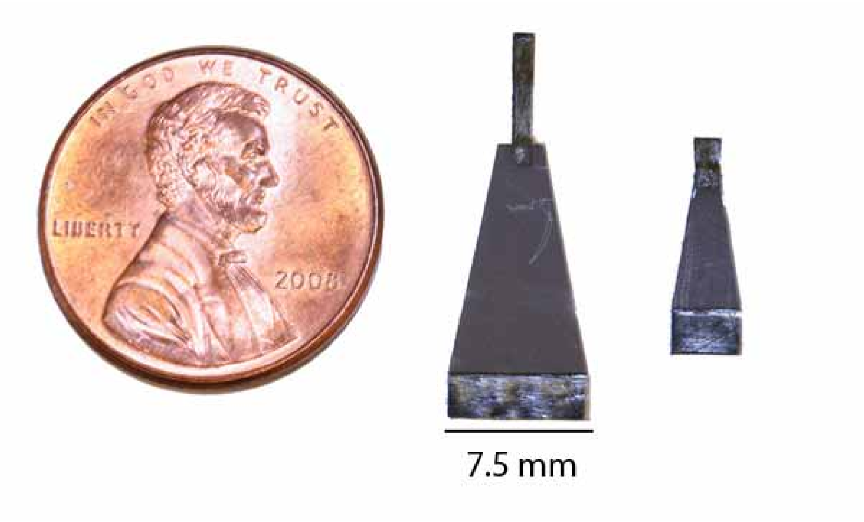

Figure 2.6: Example power (left) and control (right) piezoelectric bimorph actuators.

placement can be predicted [97], under loading conditions it is more realistic to model the actuator as a sinusoidal force input. This also allows us to analyze the effects of drive frequency and system resonance, which cannot be done with the kinematic model. This can be accomplished through the use of an Euler-Lagrange formulation:

$$\frac{d}{dt}\left(\frac{\partial L}{\partial \dot{q}}\right) - \frac{\partial L}{\partial q} = \frac{\partial W_{ext}}{\partial q} \tag{2.3}$$

where $L = KE - PE$, W_{ext} is the work done on the system and q is a generalized system position vector, the size of q being equal to the number of degrees of freedom of the system (for an example showing the full derivation of the Euler-Lagrange formulation for the Berkeley MFI, see [7]). Holding the control actuator position fixed reduces the transmission system to 1-DOF; either ϕ or δ_1 can be used as the generalized position coordinate since they are related explicitly via (2.1). It will be seen later that it is more convenient to work in the wing space than the actuator space, meaning (2.3) will evaluate to a nonlinear second-order ODE in θ_w:

$$\ddot{\phi} = f(\phi, \dot{\phi}, t) \tag{2.4}$$

This necessitates writing the system kinetic energy, potential energy, and work terms as functions of ϕ and time. The actuator's applied force, stiffness due to elastic deformation, damping due to hysteresis, and work done on the system are given as:

$$F_{act} = F_b \sin(\omega \cdot t) \tag{2.5}$$

$$F_{spring} = -k_{act}\delta_1 \tag{2.6}$$

$$F_{damp} = -b_{act}\dot{\delta}_1 \tag{2.7}$$

$$dW_{act} = (F_{act} + F_{spring} + F_{damp})d\delta_1 \tag{2.8}$$

where F_b is the actuator blocked force, ω is the frequency of the driving voltage signal, and k_{act} and b_{act} are the actuator's equivalent linear spring and damping constants, respectively. Equations (2.6-2.8) can be written in terms of ϕ via the inverse of (2.1) for consistency with the selection of q in the Euler-Lagrange formulation. Using the full nonlinear kinematic equation becomes computationally expensive due to the complicated nature of the derivatives, therefore a quadratic fit is used:

$$\delta_1 = A\phi^2 + B\phi + C \tag{2.9}$$

where A, B and C are intrinsic functions of δ_2. The kinetic energies of the transmission and actuator are negligible compared with that of the wings, and the stiffness of the flexure hinges is negligible relative to the actuator, and thus these terms are ignored. The kinetic energy of the wing is given as:

$$KE_{wing} = \frac{1}{2}\upsilon \cdot (J\upsilon) \tag{2.10}$$

where υ is the rotational velocity vector and J is the inertia tensor about the pivot point at the base of the wing. The wing has two rotational degrees of freedom – stroke angle ϕ and angle of attack α (Fig. 1.4). To simplify the wing motion to 1-DOF mathematically, the angle of attack can be correlated to stroke angle by empirical observation the HMF, and is shown to be about 45° at the mid-stroke ($\phi = 0$) and 90° at the ends of the stroke ($|\phi| = \phi_{max}$), giving the following form:

$$\alpha = \frac{\pi}{2} - \frac{\pi}{4}\cos\left(\arcsin\left(\frac{\phi}{\phi_{max}}\right)\right) \tag{2.11}$$

A quasi-steady blade element method [38] can then be used to approximate the aerodynamic force on the wing:

$$C_N = a \cdot \sin(\alpha) \tag{2.12}$$

$$C_T = b \cdot \cos^2(2\alpha) \tag{2.13}$$

$$F_N = c \cdot \dot{\phi}^2 C_N \tag{2.14}$$

$$F_T = c \cdot \dot{\phi}^2 C_T \tag{2.15}$$

where C_N and C_T are the force coefficients for the normal and tangential forces on the wing (F_N and F_T respectively), and a, b, and c are constants that depend on wing

$$\begin{aligned} \ddot{\phi} = \Big[& \Big(F_0 \sin(\omega t) - b_{act}\dot{\delta}_1 - k_{act}\delta_1 \Big) \frac{\partial \delta_1}{\partial \phi} \\ & - \Big(ca\dot{\phi}^2 \sin^2(\alpha) + cb\dot{\phi}^2 \cos^3(\alpha) \Big) r_{cp} \cdot sign(\dot{\phi}) \\ & - \frac{\pi^2 \phi \dot{\phi} \cos(\psi) \sin(\psi)}{16 \psi \phi_{max}^2} \left(J_{zz} - J_{yy} \right) \Big] \left(J_{yy} \cos^2(\psi) + J_{zz} \sin^2(\psi) \right)^{-1} \end{aligned} \tag{2.18}$$

geometry. The drag and lift forces can then be written as follows:

$$\begin{bmatrix} F_{drag} \\ F_{lift} \end{bmatrix} = R(\alpha) \begin{bmatrix} F_n \\ F_t \end{bmatrix} \tag{2.16}$$

where $R(\alpha)\epsilon SO(2)$. The lift force acts perpendicular to the plane of the transmission, therefore does no work against the actuator and is not included in the energy formulation. The drag force is exerted in the plane of the transmission and acts as a damping force against the actuator. The work done by the drag force is given by:

$$dW_{drag} = F_{drag} r_{cp} d\phi \tag{2.17}$$

where r_{cp} is the radius from the base of the wing to the aerodynamic center of pressure.

The terms in (2.6)-(2.17) can be inserted into the Euler-Lagrange formulation (2.3), which evaluates to the full equation shown in (2.18); where $\psi = \frac{\pi}{2} - \alpha$, and the sign($\dot{\phi}$) term ensures that the drag force always does negative work on the system (by convention, F_{drag} is defined to always be positive). Equation (2.18) can then be solved numerically to give the wing position as a function of time (Fig. 2.7). The output displacement is approximately sinusoidal (not a perfect sinusoid since this is

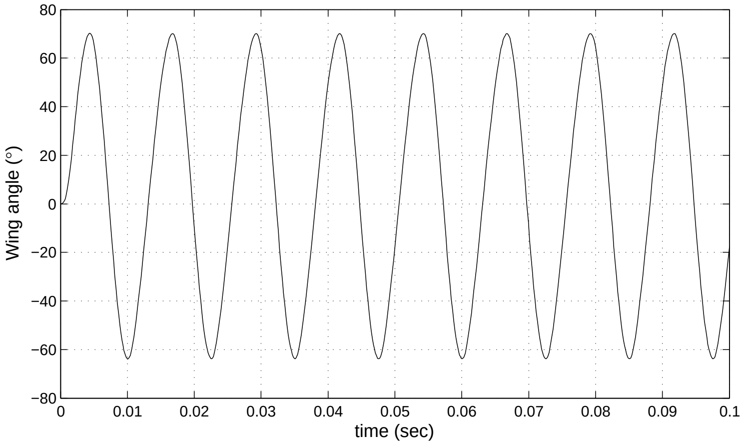

Figure 2.7: Wing trajectory as a function of time, solved numerically using (2.18). Actuator drive frequency is 80Hz.

a nonlinear system) with an amplitude of roughly ±70°.

As with the kinematics, it is of interest to determine the effects of control actuator motion on the total and mean stroke angles, which will then determine body torques. This can be done by running multiple simulations with a fixed driving force and frequency, and varying δ_2 as an input parameter (Fig. 2.8). The results follow the same trend as is predicted by the kinematic model (Fig. 2.5), showing a change in total flapping of 24° and a very small change in mean stroke angle over the full range of the control actuator, on the order of several degrees.

The dynamic simulation can also be used to determine the frequency response of the system over the range of the control actuator motion (Fig. 2.9). This shows that the control actuator is expected to have a large impact on the system resonant frequency, shifting the resonant peak from 55Hz at δ_2 =-100μm to 100Hz at δ_2 =+100μm. This is because the control actuators effectively modulate the transmission ratio between the power actuators and the wings, affecting the system dynamics.

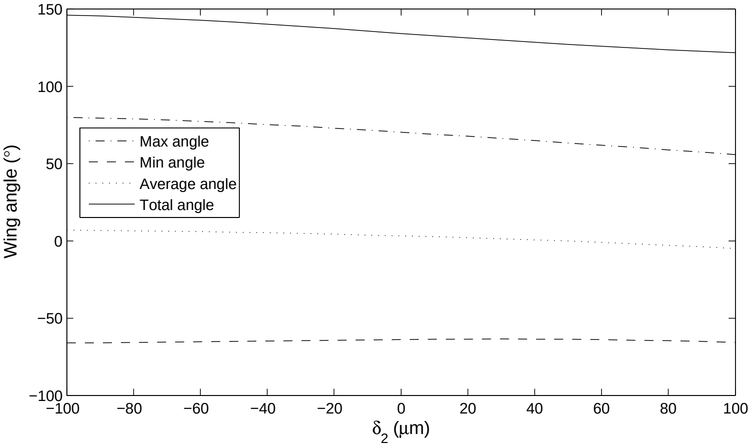

Figure 2.8: Numerical simulation results showing maximum, minimum, mean and total stroke angles over the range of the control actuator motion, while holding the power actuator's driving force and frequency constant at 80Hz.

This is discussed further in Chapter 4.

Note that this dynamic model is for one side of the transmission only and assumes that the second control actuator remains fixed or is nonexistent ($\delta_3 = 0$). In practice, the addition of a second control actuator is kinematically redundant, but *not* dynamically redundant - the use of two control actuators out-of-phase can keep the net load seen by the power actuator, and thus the resonant frequency of the system, constant.

Finally, (2.16) can be time-averaged to estimate the average lift force on each wing. Assuming δ_2 varies for one wing while holding δ_3 constant, and that the radius to the aerodynamic center of pressure, r_{cp} is known ($\sim$ 10.7mm), this can be used to predict resultant body torques about the yaw axis. The average total lift (both wings) for $\delta_2 = \delta_3 = 0$ is 1.2mN, which is in accordance with experimental measurements from [91]. The lift force on one wing can be varied from .5-.8mN with control actuator motion (Fig. 2.10a). This means body torques up to 1.7mN·mm can be generated with the motion of only one control actuator (Fig. 2.10b).

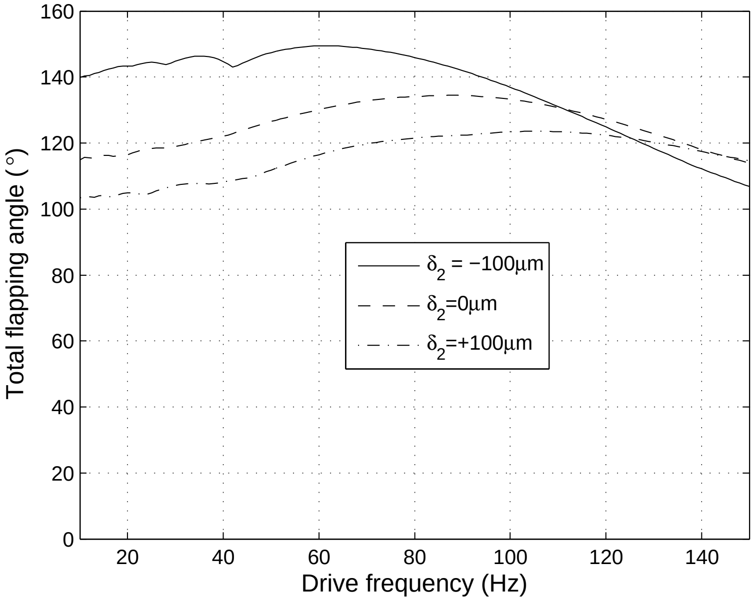

Figure 2.9: Frequency response of the system over the range of control actuator motion, $\delta_2 = \pm 100\mu$m. The resonant peak is shown to shift from approximately 55 to 100Hz.

(a) Lift force on one wing

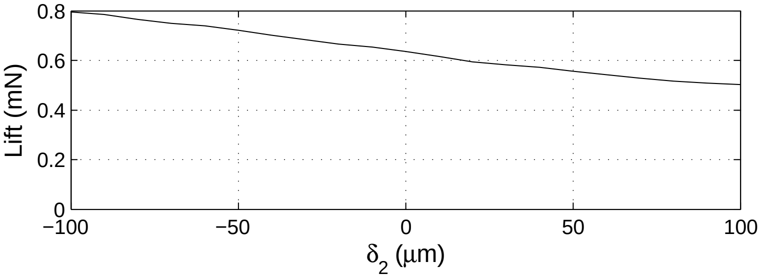

(b) Net body torque

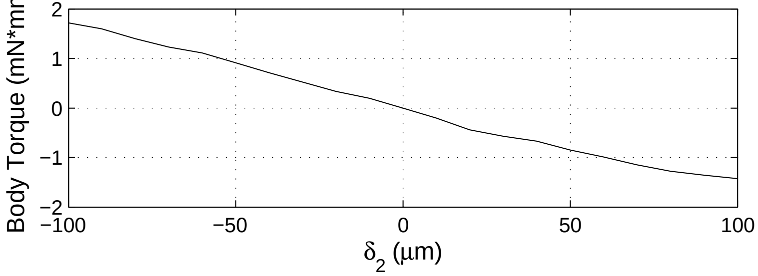

Figure 2.10: Variation in lift force on one wing with control actuator motion (a) and net body torque generated about the yaw axis assuming δ_3 is held constant while δ_2 is varied (b).

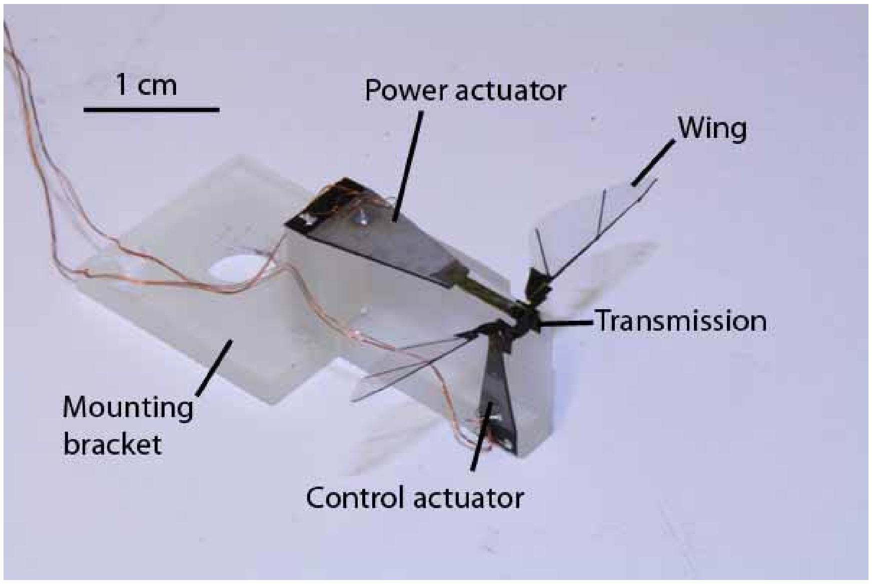

Figure 2.11: The complete test setup.

2.4 Experiments and Results

A prototype RoboBee device was constructed in order to test the predictions of the kinematic and dynamic analyses. The complete test apparatus is shown in Fig. 2.11. Rather than a flightweight airframe, the actuators and transmission were mounted to a rapid-prototyped acrylic block. Only one control actuator was used, with the opposite wing pivot being attached to ground.

High-speed video of the wing flapping was taken (Fig. 2.12) and the wing trajectories were extracted using a custom Matlab script, in order to compare to the trajectories predicted by the kinematic and dynamic analyses. For consistency, all trials were run at the expected resonant frequency of 80 Hz (predicted at δ_2=0). The power actuator drive amplitude was held constant at $\pm 300\mu$m.

The kinematic model assumes that the central link connecting the two sides of the transmission is rigid and can only move vertically; this means that control actuator

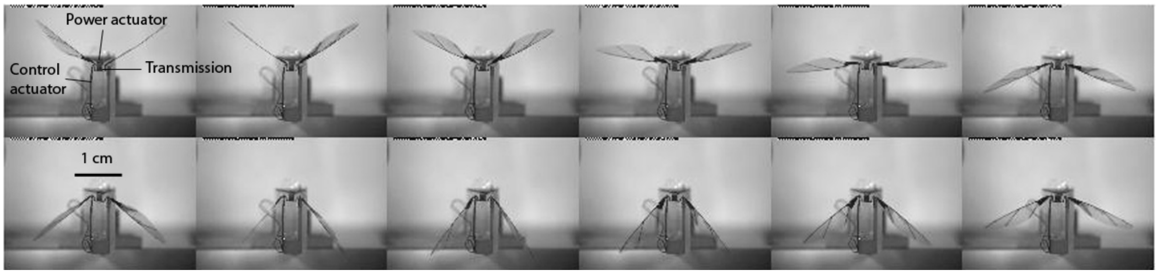

Figure 2.12: Frames from a typical high-speed video trial showing the actuated flapping of the wing and passive rotation about the spanwise axis. Flapping is at 110 Hz, video shot at 1600 fps.

motion should have no effect on the opposite wing. To test the validity of this assumption, the trajectories of both wings are tracked at the extremes of the control actuator motion, $\delta_2 = \pm 100\mu$m while holding the power actuator signal constant at 80Hz, $\pm 300\mu$m (Fig. 2.13). Analyzing the trajectories of the left (attached to control actuator) and right (attached to ground) wings shows that the lateral stiffness of the transmission is not infinite, as assumed in the kinematics, and the control actuator has a small effect on the opposite wing. However, this change is negligible compared to the effect on the proximal wing – showing changes in amplitude of roughly 30° and 4° on the left and right wings, respectively (Table 2.2).

Table 2.2: Stroke amplitude ϕ_{total} for each wing at extremes of control actuator motion

	δ_2 = +100μm	δ_2 = -100μm	$\Delta\phi_{total}$
Left wing	89°	118°	29°
Right wing	102°	98°	4°

Once the influence of the control actuator on the two wings has been verified at the motion extremes, tests are then performed over the full range of motion. Again, the power actuator signal is held constant at 80Hz and $\delta_1 = \pm 300\mu$m while the control actuator position is varied from -100μm to +100μm. The total and average

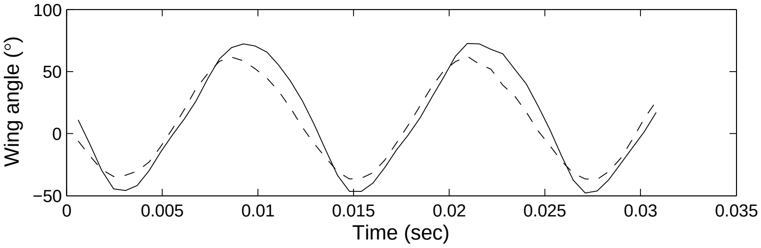
(a) $\delta_2 = -100\mu m$

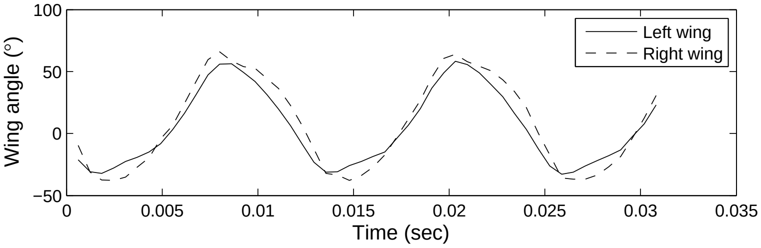
(b) $\delta_2 = +100\mu m$

Figure 2.13: The trajectories of the left and right wings (attached to the control actuator and ground respectively) are tracked at both extremes of the control actuator motion. This shows that the impact of the control actuator on the opposite wing, while not zero as predicted by the pseudo-rigid body model, is negligible compared to the influence on the proximal wing. Note that the stroke trajectories are not perfectly in phase, potentially due to nonlinear system behavior.

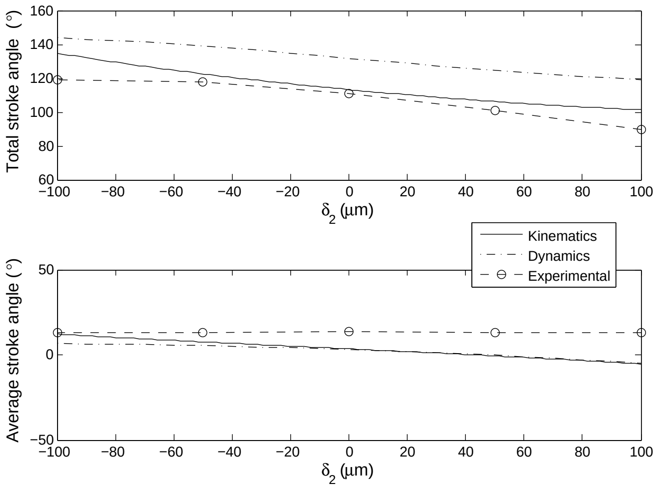

Figure 2.14: Measured mean and total stroke angles compared to kinematic and dynamic predictions at 80Hz.

stroke angles of the orthogonally actuated wing are extracted for each trial since they will influence body torque generation; these results are compared to both kinematic and dynamic predictions (Fig. 2.14). For total stroke angle, the kinematic, dynamic and experimental measurements all show the same trend – control actuator motion increases or decreases stroke angle with $\delta_2 < 0$ or $\delta_2 > 0$ respectively. However, while both kinematic and dynamic models predict a change in the average stroke angle, experimental results show the average angle to hold relatively constant over the range of control actuator motion. This relatively constant nonzero average stroke angle is most likely due to a manufacturing imperfection - a small misalignment when manually mounting the transmission to the airframe and connecting it to the actuators can have a non-negligible impact on the neutral stroke angle. Work is ongoing to increase the accuracy and level of automation of assembly steps in order to minimize such errors.

Table 2.3: Kinematic, dynamic and experimental results for effect of control actuator motion on total stroke angle at 80 Hz

Method	δ_2 = +100μm	δ_2 = -100μm	$\Delta\phi$
Kinematics	101°	134°	33°
Dynamics	119°	144°	25°
Experimental	90°	119°	29°

The changes in total stroke angle are summarized in Table 2.3. The observed magnitude of stroke angle is lower than that predicted by both kinematics and dynamics. This can likely be attributed to an over-estimation of the power actuator force and displacement, as well as minor manufacturing defects such as debris and epoxy in the flexure gaps, which can impede motion. However, the observed *change* in total stroke angle over the range of control actuator motion lies about halfway between the kinematic and dynamic predictions.

It is therefore instrumental to eliminate resonant effects by running the tests quasi-statically at a very low frequency (1Hz), at which aerodynamic and inertial forces will be negligible due to the low wing velocity. The same information is then collected over the range of control actuator motion (Fig. 2.15). The changes in total stroke angle are summarized in Table 2.4. As expected, the dynamic model converges to the kinematic model as the drive frequency approaches zero. While both models still overestimate the observed total stroke angle, the effect of the control actuator still follows the same trend. These results justify the use of control actuators to asymmetrically modify wing stroke amplitude.

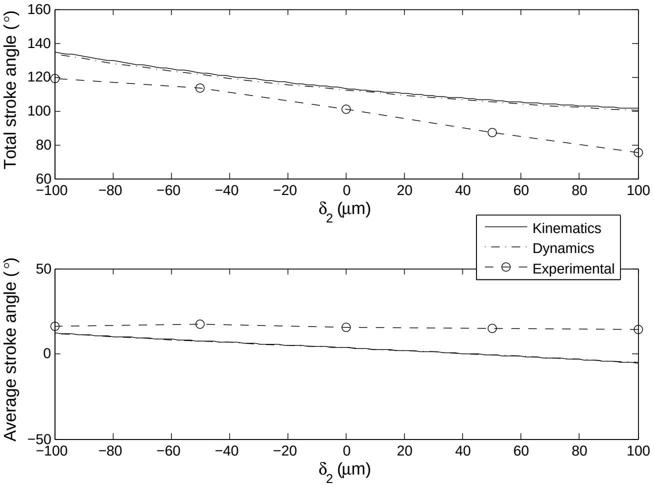

Figure 2.15: Measured mean and total stroke angles compared to kinematic and dynamic predictions at 1Hz.

Table 2.4: Kinematic, dynamic and experimental results for effect of control actuator motion on total stroke angle at 1 Hz

Method	@δ_2 = +100μm	@δ_2 = -100μm	$\Delta\theta_w$
Kinematics	101°	134°	33°
Dynamics	101°	134°	33°
Experimental	75°	119°	44°

2.5 Flight-weight mechanism design

Initial attempts (circa 2009) to scale down the design to a flight-weight (130mg) prototype (Fig. 2.17) were unsuccessful primarily due to limitations in the fabrication process used at the time. A drastically improved fabrication process [90] allowed the development of higher-performance prototypes (Fig. 2.18). A 110mg prototype developed in 2011 was used to collect torque data (presented in Chapter 5) and an 83mg prototype developed in 2012 was used for the controlled flight experiments presented in Chapter 7. All parts were laser-machined and constructed using the process from [90], but hand-assembled and did not utilize the pop-up process presented in [80]. Detailed fabrication instructions for the final prototype are presented in Appendix A. Individual parts and a completed prototype of the 110mg bee are shown in Fig. 2.16.

2.6 Discussion

The device presented in this chapter is a proof-of concept for a transmission mechanism using separate power and control actuators to generate stroke amplitude asymmetries, which should lead to roll torques according to an aerodynamic model. The results in this chapter are limited because no experimental torque data was collected, and the 130mg prototype did not function well enough for flight tests. Chapter 5 addresses the development of a custom micro-torque sensor for characterizing the torque output, and Chapters 6 and 7 present torque measurement results and open and closed-loop flight experiments.

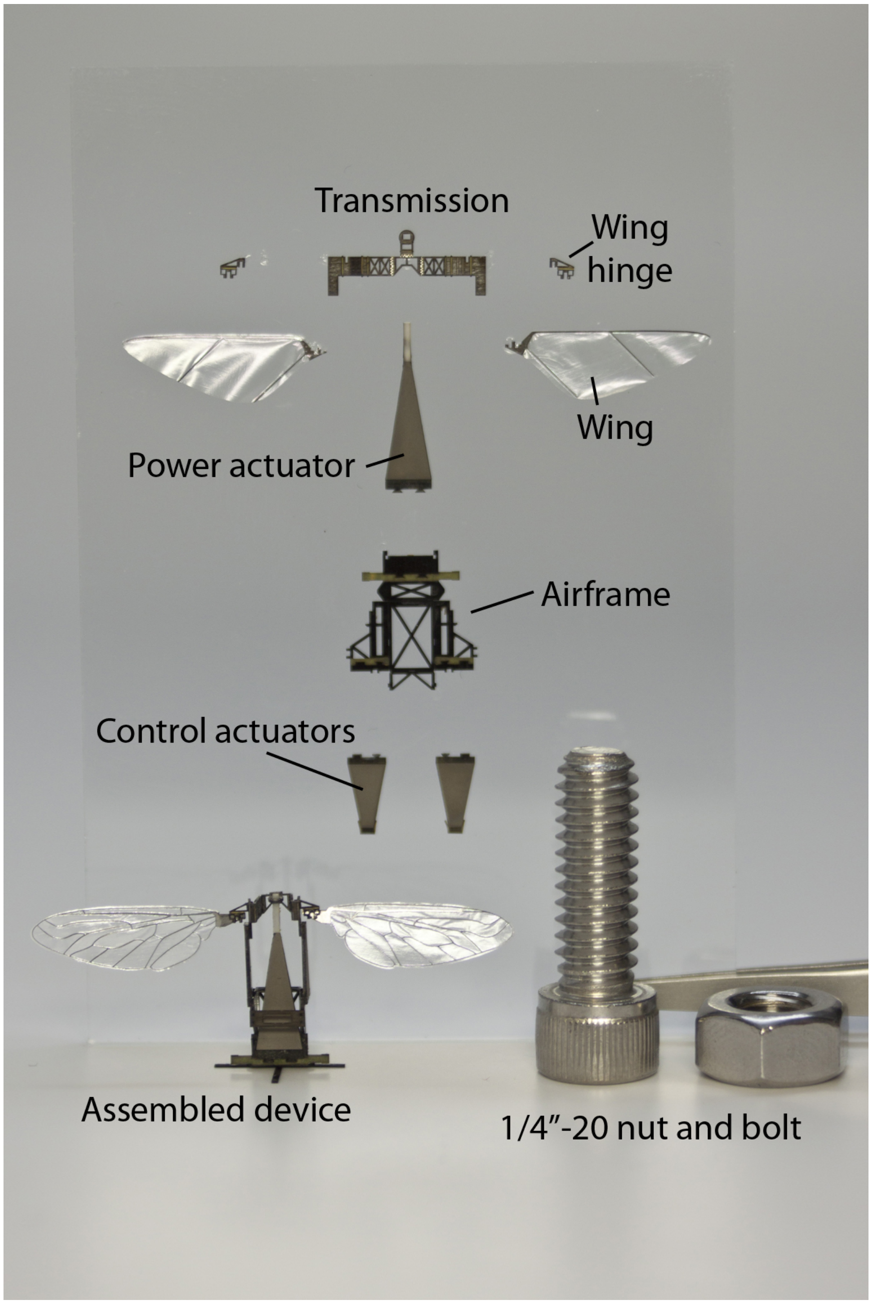

Figure 2.16: Individual components and a completed Robobee prototype, next to a 1/4"-20 nut and bolt for scale. This prototype has a mass of 110mg with no onboard electronics. Photo courtesy of Eliza Grinnell.

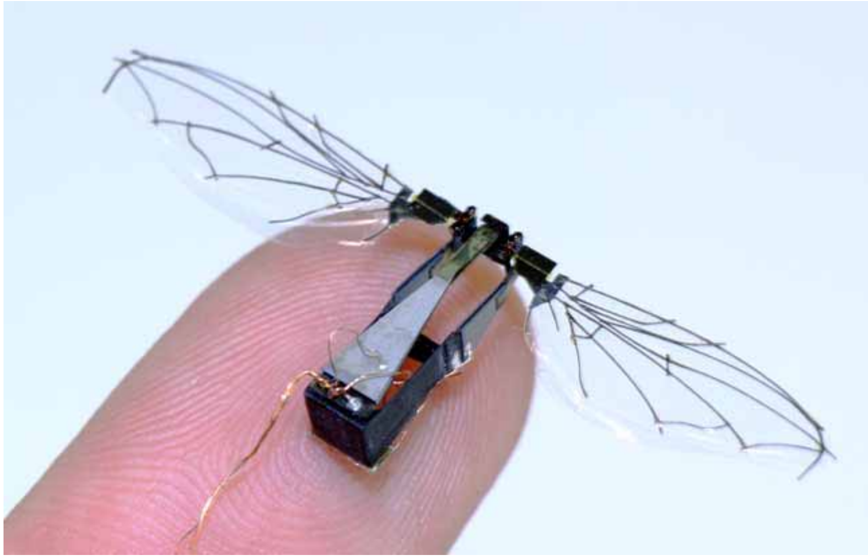

Figure 2.17: The first RoboBee prototype to include control actuators. Built in 2009, this version had a mass of 130mg and a 4cm wingspan, but did not function well enough for torque measurements or flight control tests.

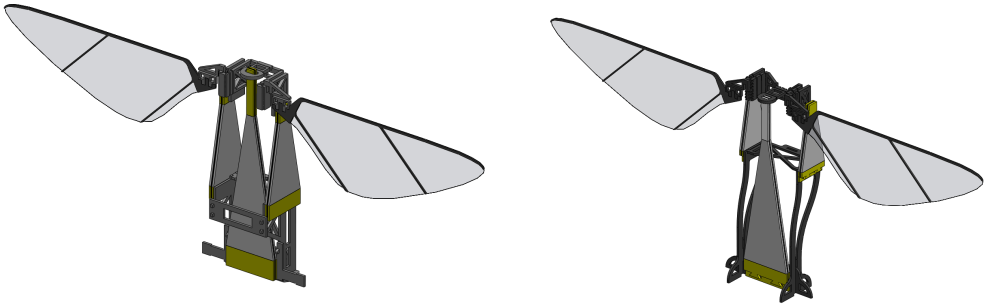

Figure 2.18: Solidworks models of a 110mg RoboBee prototype used for torque characterization (left) and an 83mg prototype used for flight experiments.

Chapter 3

Alternative Mechanical Design

3.1 Introduction

This chapter presents an alternative mechanical design to that presented in Chapter 2. The use of two control actuators is kinematically redundant. In this chapter a “hybrid” power-control actuator is used to accomplish the same goal - asymmetric stroke amplitudes to generate roll torques.

3.2 Mechanical Design

The design introduced in Chapter 2 made use of two smaller control actuators in addition to the primary power actuator to modulate roll torques. These actuators introduced control inputs δ_2 and δ_3, allowing movement of the previously grounded wing pivots and asymmetric modulation of wing kinematics (Fig. 3.1b). The design presented in this chapter uses a coupled 2-DOF power-control actuator structure,

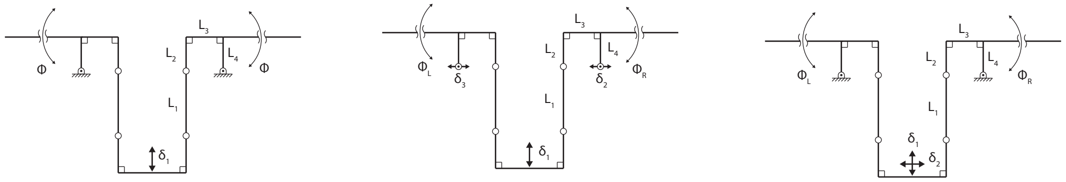

(a) (b) (c)

Figure 3.1: The original 1-DOF transmission design with only one power actuator input and no control inputs (a), a 3-DOF design that uses a single power actuator and two control inputs (b), and a 2-DOF design which uses a coupled power-control input (c). Note that in (a) and (b), the central link of the transmission is constrained to move vertically.

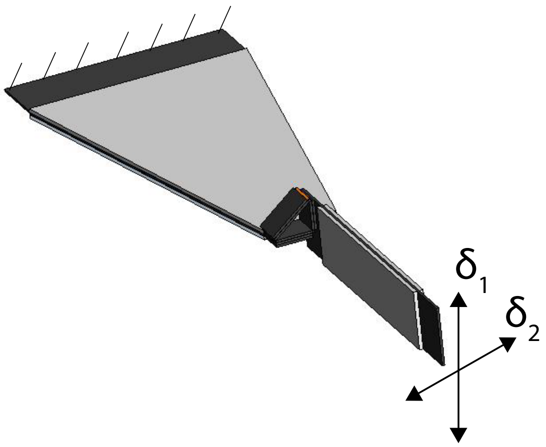

Figure 3.2: A hybrid power-control actuator, consisting of two piezoelectric bimorphs connected by a 90° angle bracket.

which allows the central link of the transmission to be moved orthogonal to the primary actuation mode (Fig. 4.9c). This permits a coupled change in stroke angles of the left and right wings, ϕ_L and ϕ_R. The "hybrid" power-control actuator (Fig. 3.2) consists of two bimorphs connected by a 90° angle bracket, and requires four electrical inputs: two constant voltages (bias and ground), shared between the bimorphs, and two independent signal voltages (power and control).

3.3 Kinematics

Based on the kinematic analysis in Chapter 2, transmission link lengths (as labeled in Fig. 4.9) are selected to be $L_1 = 400\mu$m, $L_2 = 300\mu$m, $L_3 = 300\mu$m, and $L_4 = 450\mu$m. The stroke angle ϕ can be written as a function of transmission geometry and actuator inputs δ_1 and δ_2 as follows:

$$\begin{aligned} \phi = acos\left(\frac{(L_y-\delta_1)^2+C_1}{C_2\sqrt{L_x^2+(L_y-\delta_1)^2}}\right) \\ +atan\left(\frac{L_x}{L_y-\delta_1}\right)+atan\left(\frac{L_2-L_4}{L_3}\right)-\frac{\pi}{2} \end{aligned} \tag{3.1}$$

where $L_x = L_3 + \delta_2$ or $L_x = L_3 - \delta_2$ for the left and right wings, respectively, and

$$L_y = L_1 + L_2 - L_4 \tag{3.2}$$

$$C_1 = L_3^2 + (L_2 - L_4)^2 - L_1^2 + L_x^2 \tag{3.3}$$

$$C_2 = 2\sqrt{L_3^2 + (L_2 - L_4)^2} \tag{3.4}$$

Using (4.2), the effect of control actuator movement on wing stroke amplitude can be predicted (Fig. 3.3). In the control actuator's neutral position, the stroke amplitudes of the left and right wings are equal and thus there will be no net roll torque. When the control actuator moves in either direction, it increases one wing's stroke amplitude while decreasing the other. This difference in amplitude will create different average lift forces on each wing, and thus a roll torque (as shown above in Fig. 2.3).

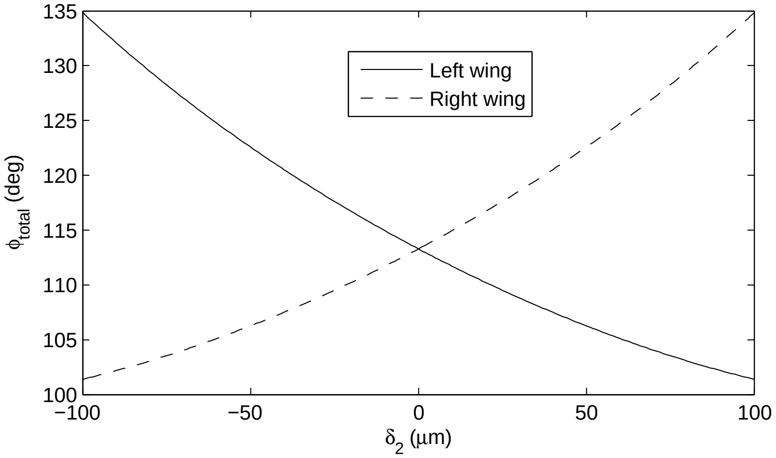

Figure 3.3: Kinematic model for stroke amplitude of the left and right wings plotted over a range of control actuator motion, for a fixed power actuator input ($\delta_1 = \pm 300\mu m$).

3.4 Dynamics

An Euler-Lagrange formulation can be used in the same manner as Chapter 2 to derive the equations of motion for the system. This derivation is not reproduced in this chapter. A sketch of the dynamic model is shown in Fig. 3.4. Numerically solved wing trajectories are shown in Fig. 3.5 for three different control actuator positions. As expected, the dynamic model shows that control actuator motion will create asymmetric wingstroke amplitudes. This is illustrated in Fig. 3.6, which shows stroke amplitudes for the left and right wings as a function of both power actuator frequency and control actuator position. The control actuator motion has the same effect as predicted by the kinematic model (increased $\phi_{R,tot}$ and decreased $\phi_{L,tot}$ for δ_2 >0, vice versa for δ_2 <0), but here we also see that there is a clear resonant peak for wing amplitude. However, the *difference* between stroke amplitudes depends primarily on control actuator position and is fairly independent of drive frequency (Fig. 3.7). Note that the resonant frequency for this model is much lower than that

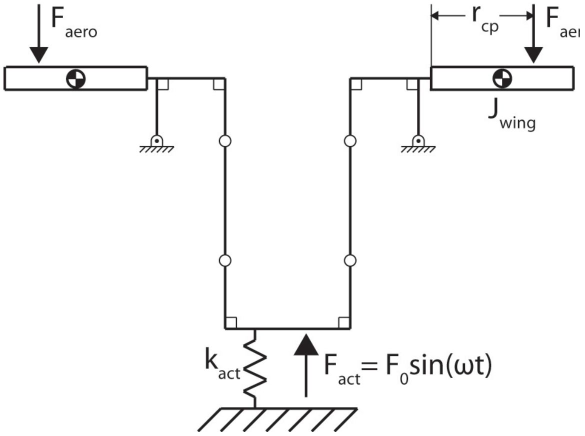

Figure 3.4: Diagram for the dynamic model of the actuator, transmission and wing system (not to scale).

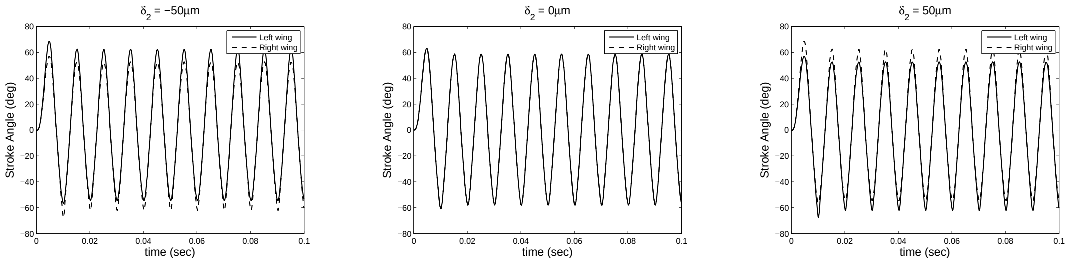

Figure 3.5: Numerical solutions for wing trajectory as a function of time for three different control actuator positions. As predicted with the kinematic model, the dynamic model shows that the control actuator will create an asymmetry in stroke amplitude.

predicted in Chaper 2 due to the larger (thus heavier and less stiff) actuator structure.

Most important from a control standpoint, the blade-element aerodynamic model can be used to calculate the lift force on each wing. This allows calculation of net body torques, and thus angular acceleration using a rough first-order approximation that ignores any rotational aerodynamic damping on the body. Predicted body torques are on the order of 1mN·mm. This is consistent with dynamic simulations from [43] and experimental results presented in Chapter 6. Due to the robotic bee's low

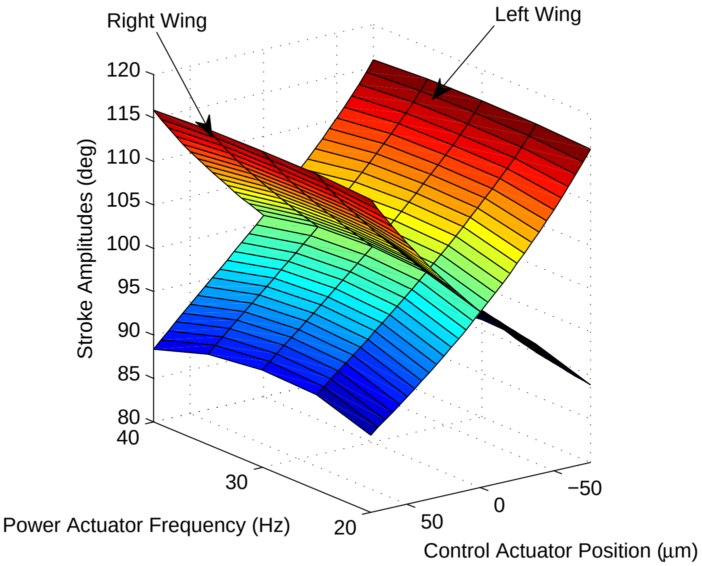

Figure 3.6: Results of numerical simulations showing left and right wing stroke amplitudes as a function of both power actuator frequency and control actuator position. A shallow resonant peak in stroke amplitude is evident around 30Hz.

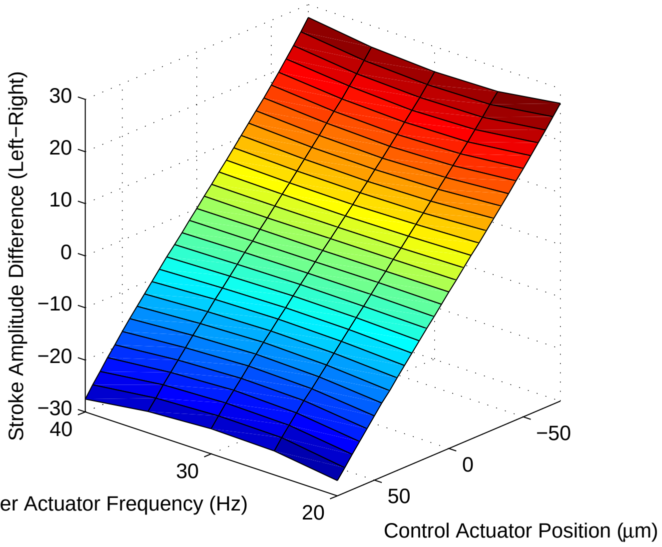

Figure 3.7: Numerical simulations showing the *difference* between wing stroke amplitudes.

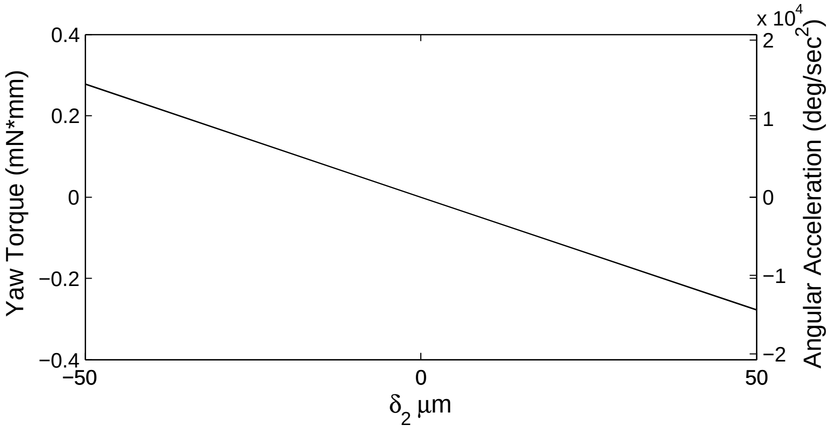

Figure 3.8: Net yaw torques and resulting angular accelerations as a function of control actuator position (at constant power actuator frequency), from numerical simulations.

mass moment of inertia about the roll axis (1.1g·mm^2 as calculated with a Solidworks model), this allows for high angular accelerations on the order of thousands of deg/sec^2 (Fig. 3.8). Previous work has shown that rapid turns during insect flight are actually inertia-dominated and not viscous-dominated [46], so ignoring rotational aerodynamic damping in this calculation is not an unreasonable assumption.

3.5 Experiments and Results

While kinematic and dynamic models are useful as design tools and for conceptualizing different control strategies, experimental validation of their predictions is vital. Inaccuracies arise in both the kinematic and dynamic modeling approaches that limit their applicability. For example, the kinematic model assumes the transmission structure consists of rigid links connected by ideal revolute joints, while in reality there is a finite compliance in the mechanism and the flexure joints may experience axis drift. It also assumes perfect geometric construction (exact 90° angles, symmetric

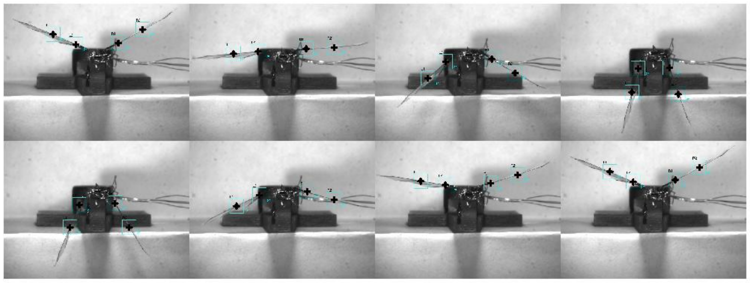

Figure 3.9: Sample screenshots from ProAnalyst software showing wing markers being tracked through a video. Stroke angles are automatically calculated with the software based on marker positions.

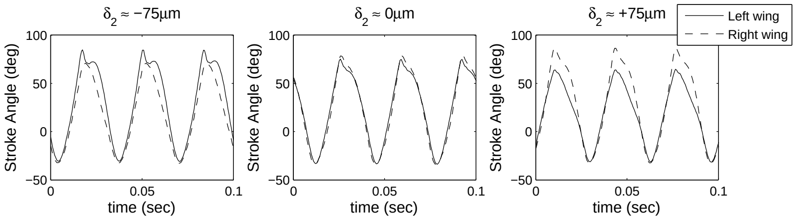

Figure 3.10: Wing trajectories extracted from videos using the ProAnalyst software. While not perfectly symmetric due to minor manufacturing defects, the resulting wing motion is comparable to that of the dynamic simulations as shown in Fig. 3.5.

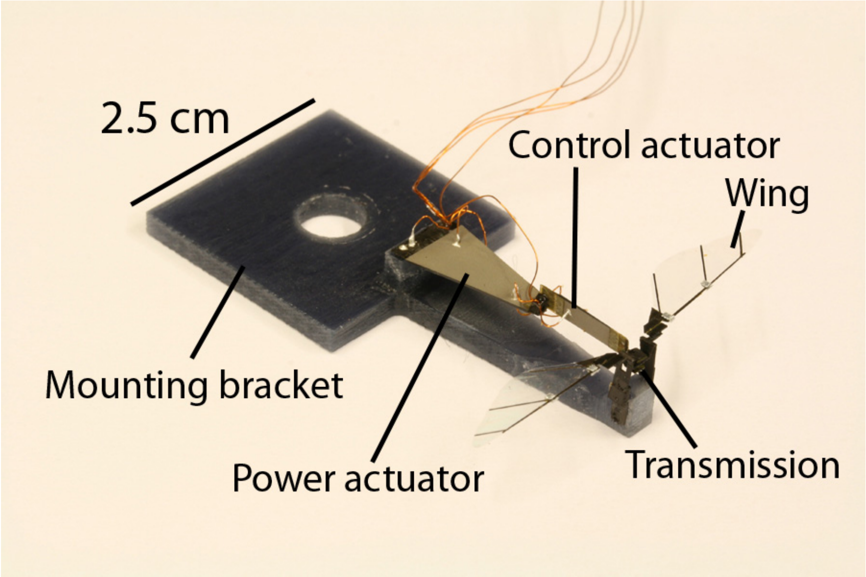

Figure 3.11: The complete test device. The hybrid actuator and transmission structure are mounted to rapid-prototyped rigid acrylic base. Retroreflective markers are placed on the leading edge of each wing in order to enhance automated data collection capabilities.

alignment etc.), which is currently difficult to achieve when manufacturing devices at such a small scale. The dynamic model is limited both due to difficulties in accurately predicting actuator force and stiffness, and assumptions inherent in the quasi-steady aerodynamic model, e.g. neglecting spanwise flow along the wing, vortex shedding, wake capture, and other aerodynamic effects that are known to be beneficial to insect lift generation.

Therefore, a test device was constructed to empirically determine the effects of control actuator motion on wing trajectory (Fig. 3.11). The structure was designed with over-sized actuators and built on a rapid-prototyped acrylic base in order to serve as a robust test bed and proof of concept. Future designs will incorporate optimal-energy density actuators onto a lightweight carbon fiber airframe.

Two retroreflective markers (small pieces cut from Reflexite tape [1]) were placed on the leading edge of each wing. Note that these markers significantly increase the inertia of the wings, which is compensated for by the oversized power actuator. This has the effect of significantly lowering the system resonant frequency (about 30Hz for this test structure, compared to 110Hz in previous designs). Since the markers are used only for data collection and serve no other functional purpose, they would not be required on a final design.

A high-speed camera was oriented toward the leading edge along with two fiber-optic light sources for illumination (Fig. 3.12). With a black background, this allowed filming of high-contrast video in order to automatically track the wing markers. Automated tracking was performed with 2D image analysis software (ProAnalyst [2]). Sample video frames (with a white background for image clarity and illustration purposes) with tracked markers are shown in Fig. 3.9, and sample wing trajectories extracted for three different videos are shown in Fig. 3.10.

Tests were performed over a range of control actuator positions (-75μm to +75μm) and power actuator frequencies (20Hz to 40Hz) while holding power actuator amplitude constant. As predicted by the dynamic model, the resonant frequency of this system is higher than that in Chapter 2 due to the larger (thus less stiff and heavier) actuator structure. The effective wing inertia is also increased in the experiments due to the addition of retroreflective markers. The total and difference in stroke amplitudes are presented in Fig. 3.13 and Fig. 3.14 respectively. As predicted by the kinematic and dynamic models, control actuator motion has a large effect on relative wing motion. While drive frequency does have an effect on the individual stroke amplitude of each wing, it has little effect on the *difference* in amplitudes. A

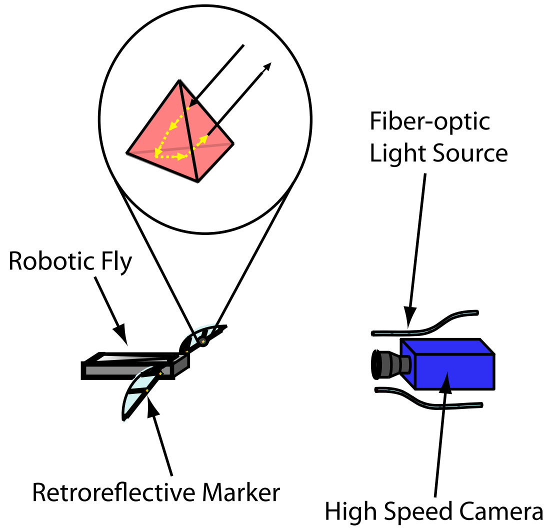

Figure 3.12: Schematic of the test setup. Retroreflective wing markers and fiber optic illuminators were used in order to facilitate automated tracking of the wing trajectory (not to scale).

constant-frequency section of the data from Fig. 3.13 at 30Hz is shown in Fig. 3.15. This plot makes the asymmetry of the data more evident - changes in wing amplitude are not perfectly symmetric about the control actuator's neutral position, as predicted by the kinematic or dynamic models. This can likely be attributed to a manufacturing asymmetry in the transmission or actuator, and highlights the need for mechanization of the micro-assembly process.

3.6 Discussion

This chapter has presented an alternative control method for generating roll torques on a microrobotic insect platform using a hybrid power-control actuator. Experimental results from a test platform show reasonable agreement with kinematic and dynamic predictions, but suffer from the fundamental issue of a lower resonant

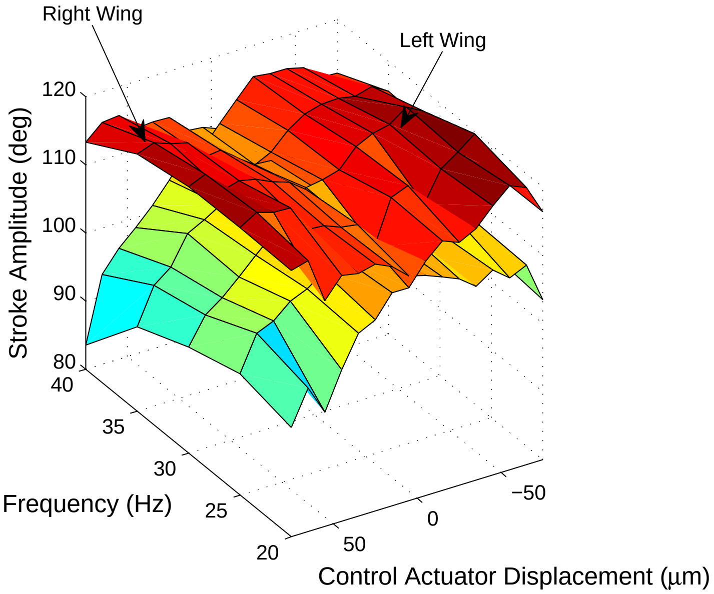

Figure 3.13: Experimental data showing total stroke amplitude for the left and right wings. The data is characterized by a broad resonant peak and a strong dependence on control actuator position. The low resonant frequency is attributed to the addition of wing markers and the larger actuator.

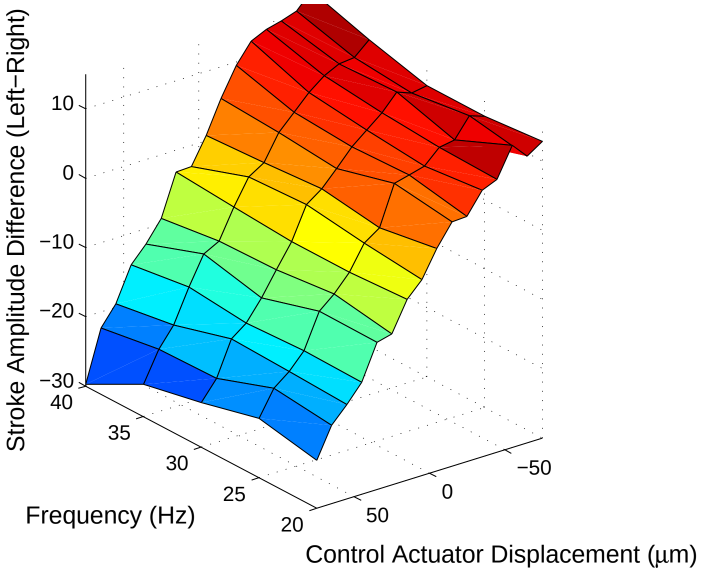

Figure 3.14: Experimental data showing difference in stroke amplitude $\phi_{total,L} - \phi_{total,R}$ as a function of both control actuator displacement and power actuator drive frequency.

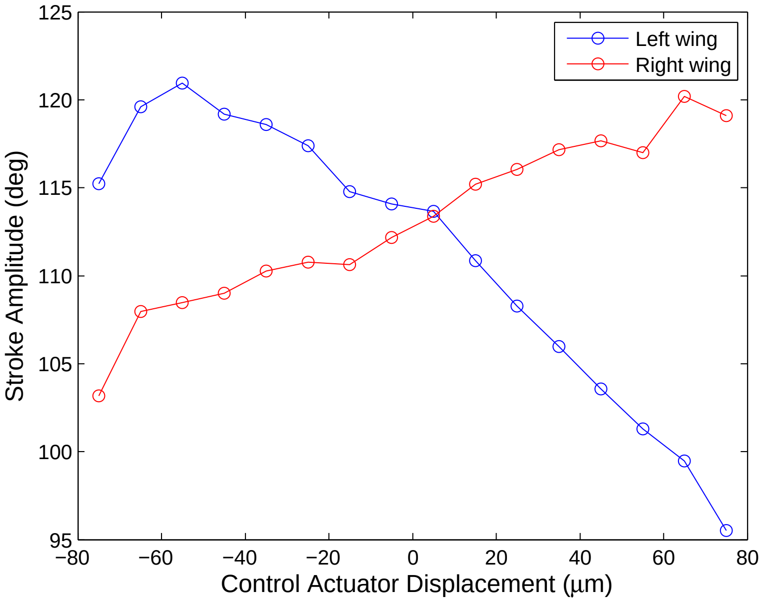

Figure 3.15: Total stroke amplitudes of the left and right wings plotted against the applied control actuator displacement, at a constant power actuator frequency of 30Hz.

frequency due to the actuator design. Initial attempts at developing a flight-weight prototype (Fig. 3.16) were abandoned in favor of the design presented in Chapter 2. However, combining the improved manufacturing process from [90] with potential new actuation technologies, or different actuator configurations, could make this design viable in the future.

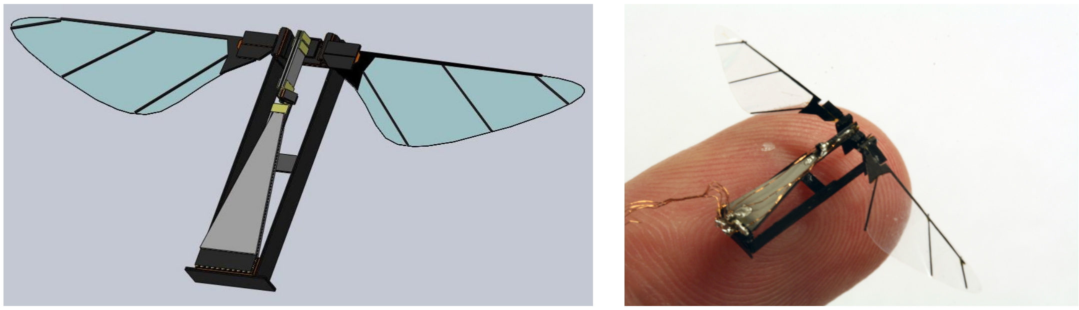

Figure 3.16: A 3D CAD model of a flightweight design utilizing the hybrid actuator structure (top), and preliminary attempt at a flight-weight prototype (bottom).

Chapter 4

Linearized Dynamic Model

4.1 Introduction

Dynamic modeling of FWMAVs typically includes several nonlinear elements, such as mechanism kinematics of linkages that are used to connect motors or other actuators to flapping wings [91], nonlinear aerodynamic forces [89], or nonlinear actuator effects such as saturation and hysteresis [96]. Wings typically flap through large angular ranges while also undergoing large changes in angle of attack, so some standard methods for linearizing dynamic models may not be appropriate. For example, the small angle assumption ($\sin\theta \approx \theta$) is usually only considered valid over a range of $\pm 15^\circ$, whereas wings may flap through a stroke amplitude as great as 120° in some FWMAVs [93] and approach 180° in some insects [38]. Lift and drag coefficients from a quasi-steady aerodynamic model typically used to predict aerodynamic forces on flapping wings [39] are functions of angle of attack and thus can vary greatly throughout a single stroke as the angle of attack changes [31]. As a result, complete dynamic models of FWMAV systems are usually highly nonlinear and time varying.

Numerous studies have investigated nonlinear modeling of FWMAVs, frequently with attention to design and optimization of elastic elements which allow a flapping system to be driven at resonance, thus reducing or eliminating the inertial cost associated with accelerating and decelerating the wing [58, 84, 66, 65, 10]. However, such studies typically focus on the addition of a spring element to an existing MAV system, without consideration for redesigning actuators, linkages or wings. Other studies, such as [57], have taken a more integrated approach to vehicle design, including wing, actuator and transmission elements, accounting for full nonlinear dynamics. Each component can have an important effect on overall system dynamics and thus vehicle performance - for example, changing the wing shape will affect both its inertial properties and aerodynamic damping forces, whereas changing a linkage system or gearbox will affect how torques map from the motor frame of reference to the wing.

Here, we seek to show that a *linear* model can serve as a simple, useful design tool to predict resonant behavior of a system under harmonic actuation, and examine the validity of a linearized model in the presence of various nonlinearities mentioned above. Such a model should accurately account for changes to system parameters such as wing shape, actuator size and transmission geometry in order to examine their effects on resonant behavior. Accurately predicting resonant behavior will allow the design of a system with maximum power transfer from actuators to the load (in this case, the air) or an optimal lift/weight ratio.

An alternative approach to developing a physics-based, ground-up nonlinear model and then linearizing it is to use system identification. Here, a linear model can be derived by experimentally measuring a system's response to chosen inputs and estimated disturbances. This is commonly used, for example, to characterize the dynamics of hovering rotary-wing MAVs moving in three-dimensional space, due to the difficulty of calculating parameters such as body inertia and drag terms for a vehicle with complex shape [48]. We define such a problem as modeling the "external" dynamics of the system. The MAV itself is treated as a black box, and system inputs are mapped to motions in three dimensional space; interior interactions of power supplies, actuators, linkages and airfoils are not modeled separately. Such experiments are useful for designing a flight controllers for a predetermined vehicle design. However, for the purposes of vehicle design itself, we must characterize the "internal" dynamics - for example, the relationship between an electrical control signal and actuator motion, or wing movement and resulting aerodynamic forces.

Using a simple lumped parameter model, [91] predicted an undamped natural frequency of 170Hz, with measured resonance of 110Hz in the experimental prototype. In this chapter, we seek to improve on this analysis and present a linearized model that can accurately predict the frequency domain response of an actuator-transmission-wing system and compare this theoretical model to a linear model derived from experimental data using system identification.

The rest of the chapter is organized as follows. In Section 4.2 the experimental setup and development of the identified model are described briefly. Section 4.3 presents the development of a linearized dynamic model. Section 4.4 compares the frequency-domain responses of the identified and theoretical models using Bode diagrams. Section 4.5 discusses implications of the results on vehicle design and usefulness of the theoretical model as a design tool, particularly how physical parameters of the system affect the resonant response. Further considerations and future work are discussed in Section 4.6.

4.2 Experiments

We use the experimental setup in Fig. 5.8, which is a modified version of the one in [89], a single wing version of robotic flapper presented in [91] designed for aerodynamic testing. This setup allows simultaneous measurement of the displacement of the distal end of the piezoelectric actuator as well as the instantaneous lift force (which is not purely aerodynamic since it will include an inertial component due to wing rotation). As shown in Fig. 5.8, the wing driver mechanism is mounted on the end of a double-cantilever beam, whose deflection is measured with a capacitive displacement sensor (CDS). For small beam deflections, there is a linear relationship between deflection and lift force. Further details on the design, fabrication and calibration of the CDS-based force sensor are given in [89] and [95]. The actuator displacement is measured using a noncontact charge-coupled device (CCD) laser displacement sensor (Keyence LK-031). The sensor laser reflection on the actuator is depicted as a circular spot in Fig. 5.8.

A discrete-time state-space representation of the system is found using a subspace algorithm as in [72]. The input to the system is an electrical signal from a D/A board which is amplified through a high-voltage amplifier and sent to the actuator, and the output is an analog voltage from the CCD sensor used to measure actuator deflection, which is then sampled and recorded with an A/D board. We refer to

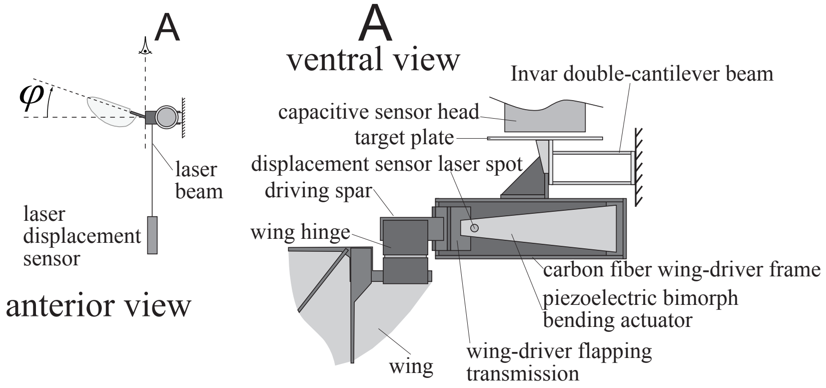

Figure 4.1: Diagram of the experimental setup for measuring lift forces and displacement of the actuator tip. The wing-driver is attached to an Invar double cantilever beam, whose deflection is measured by a capacitive displacement sensor. This deflection is proportional to the lift force. The displacement of the actuator tip is measured using a CCD laser displacement sensor.

the actual continuous-time system as P and the discrete-time identified model as P_I. A block diagram of this system is shown in Fig. 4.2. Fig. 4.3 shows Bode plots of the identified 48th-order linear model and a reduced 4th-order model. The magnitude response has been normalized to have 0 dB gain at DC. Note that P_I has two prominent resonant peaks, around 127Hz and 750Hz respectively. Understanding the 127Hz peak is of particular interest since this falls within the typical range of operation of the robot.

The higher-frequency dynamics may arise due to a variety of causes, such as higher-order dynamic components within the system (e.g. vibration of the wing itself or an unknown aerodynamic effect); or vibration of components that are considered mechanical ground, such as the airframe or lift sensor (note that the lift sensor itself has a resonant frequency of approximately 1kHz). At this point, any discussion of the root causes of these higher order dynamics is purely speculative, and thus not

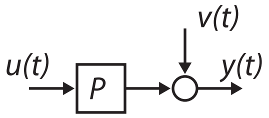

Figure 4.2: A block diagram of the experimental system. The actual open-loop plant P is driven by input voltage signal to the actuator $u(t)$. The measured output $y(t)$ is the actuator displacement, which will include effects from all aggregated output disturbances $v(t)$ acting on the system (such as aerodynamic forces).

investigated further in this paper. Regardless of their source, feedback control of the piezoelectric actuator position can be used to cancel out undesired vibrational modes [72].

4.3 Development of Linear Model

The identified model P_I gives us an empirical reference with which we can evaluate the quality of a linear, lumped-parameter model. There are three primary mechanical components of interest in formulating the dynamic model: the actuator, transmission, and wings. The three components are connected and each has associated nonlinear geometric, inertial, damping or elastic behavior (Fig. 4.4). Since the system only has one mechanical degree of freedom, it can be simplified to the one illustrated in Fig. 4.5. We assume the fourth component, the airframe, acts as a rigid mechanical ground and thus has no relevant dynamic properties. Here, we treat the linearization of each component individually, then synthesize these components to develop the full linear model.

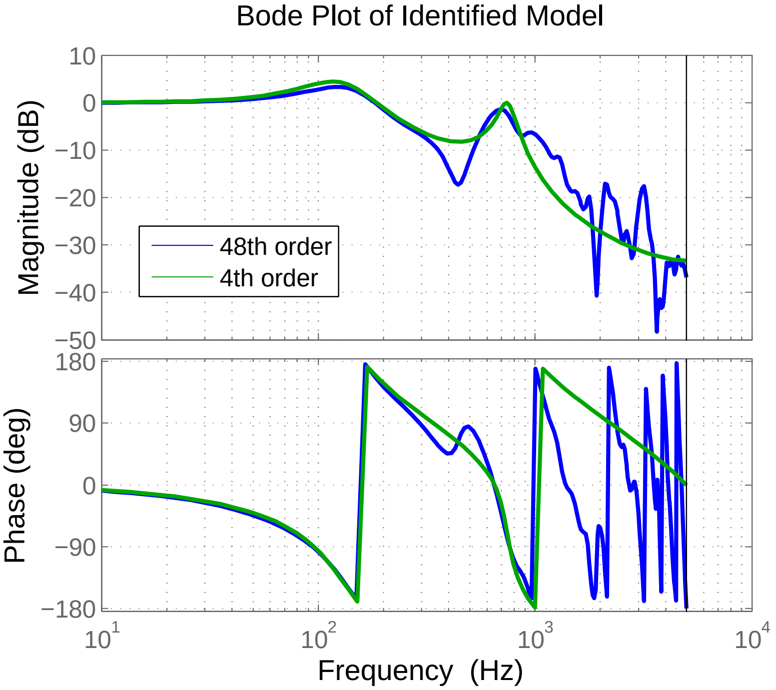

Figure 4.3: Bode plot of the identified discrete-time model P_I of the system depicted in Fig. 4.2. The input to the system is the voltage sent through an amplifier to the actuator, and measured output is the voltage of the CCD sensor which corresponds to actuator displacement.

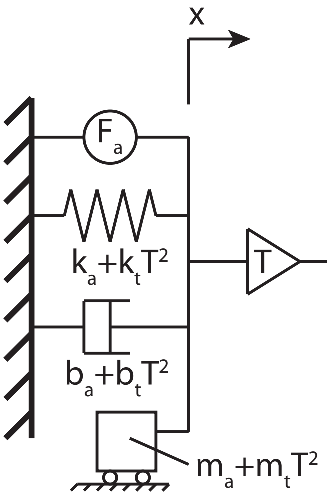

Figure 4.4: A lumped-parameter representation of the dynamic system to be modeled. The subscripts a, t and w stand for actuator, transmission and wing respectively. The system consists of an actuator connected to the wings by a mechanical transmission. Each component has its own geometric, inertial, damping and elastic terms, many of which are nonlinear but can be approximated by linear models. The transmission itself can have dynamic properties, which are mapped back to the actuator frame x via the transmission ratio T. It is important to note that x *and* ϕ *are kinematically related through the transmission* T, so the system pictured only has one degree of freedom, and therefore can be reduced to the equivalent diagram shown in Fig. 4.5.

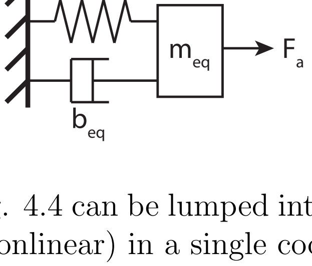

Figure 4.5: The elements in Fig. 4.4 can be lumped into equivalent stiffness, damping and inertial parameters (still nonlinear) in a single coordinate frame, either x or ϕ.

4.3.1 Actuator

Piezoelectric actuators can be subject to numerous nonlinear effects, including creep, saturation, hysteresis, and electric field-dependent stiffness (and thus resonant frequency). For modeling purposes, a piezoelectric actuator can be treated as a two-port element that transduces voltage and current to force and velocity. See [79] for more details on dynamic modeling of the actuator and a discussion of nonlinear effects.

Three key assumptions allow treatment of the actuator as a linear element. First, the actuator is driven by an ideal voltage source, therefore a voltage-driven piezoelectric actuator is equivalent to a force source in the mechanical domain. Second, the resonant frequency of the actuator ($\sim$1000Hz) is much higher than the typical operating frequencies of interest for the FWMAV in question ($\sim$100Hz), thus we can assume quasi-static operation of the actuator. This is expected based on several previous studies of piezoelectric actuators which have recorded the frequency-domain magnitude response of the actuator displacement for clamped-free boundary conditions [22, 97]. We measure the *force* response of an actuator to a voltage input, including phase information, under clamped-clamped and clamped-pin/roller boundary conditions; this is due to the difficulty of measuring force under clamped-free boundary conditions, which requires construction of a dynamometer as in [82]. The resonant frequency of a beam, if measured under one set of boundary conditions, can be adjusted for different boundary conditions via a scaling factor (see [67], p 3-73), thus we can approximate the resonant frequency of a clamped-free actuator using these tests.

A diagram of the experimental setup is shown in Fig. 4.6. Force data is recorded with a six-axis force/torque sensor (ATI Nano 17), and a linear model is derived using the same system identification techniques used to create a model of the robotic wing flapper (Fig. 4.7). The identified model shows that, at low frequencies, the force output has a flat-band response (i.e. constant gain and zero phase difference) for both sets of boundary conditions, suggesting that force is simply proportional to voltage at low frequencies. The dynamics at higher frequencies may arise due to resonance of the clamping mechanism used to hold the actuator in place, sensor noise, or other factors; but for a worst-case scenario, we can assume an actuator resonance of just over 1kHz. Based on the scaling factors in [67], a clamped-pin/roller beam will be four times stiffer than a clamped-free beam, thus we would still expect a *minimum* actuator resonance of 250Hz, outside the range of interest for our MAV. In practice, the resonant frequency of the actuators is expected to be much higher.

Lastly, the frequency and field-dependent, thus in general nonlinear, actuator damping is not a significant source of loss [81], therefore can be neglected relative to the aerodynamic damping. From the static analysis in [97], we expect the force exerted by an actuator to be proportional to the applied voltage. Thus for sinusoidal voltage excitation, the force applied by the actuator to the mechanical system is

$$F_a = F_b \sin(2\pi f t) \tag{4.1}$$

where F_b is the maximum (blocked) force of the actuator, a function of actuator geometry, material properties and applied voltage as calculated in [97], and f is the drive frequency. Neglecting nonlinear softening effects, the elastic deformation of

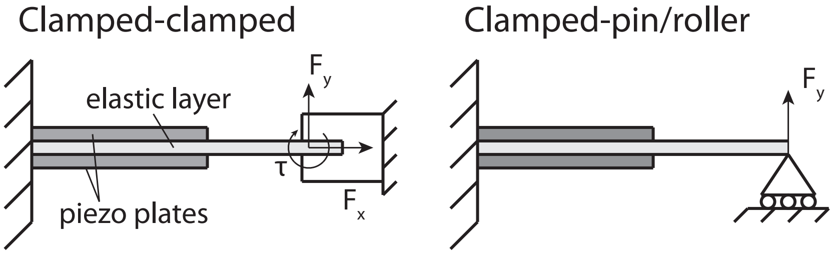

Figure 4.6: A side view of the experimental setup used to measure actuator voltage-force response. Force output of the actuator is measured under clamped-clamped and clamped-pin/roller conditions using a six-axis force/torque sensor (ATI Nano 17). The latter case allows measurement of pure vertical force, while clamped-clamped conditions measure both horizontal and vertical forces and a moment. The clamped-pin/roller condition better approximates the operating conditions when the actuator is attached to a transmission-wing system.

the actuator acts as a linear mechanical spring with spring constant k_a, also available based on the derivation in [97]. As mentioned above, we neglect the actuator damping term b_a in Fig. 4.4.

4.3.2 Transmission

The transmission consists of two symmetric slider-crank fourbar mechanisms (or, for the single-wing device used in these experiments, only a single fourbar). Their input links are rigidly connected so the entire transmission is only 1DOF. Half of the transmission is shown in Fig. 4.8. The transmission physically consists of carbon fiber links connected by flexible polymer joints - a *pseudo-rigid body* assumption models the carbon fiber links as rigid and the flexures as ideal revolute joints with torsional springs [94]. This allows kinematic analysis of the transmission to map actuator input

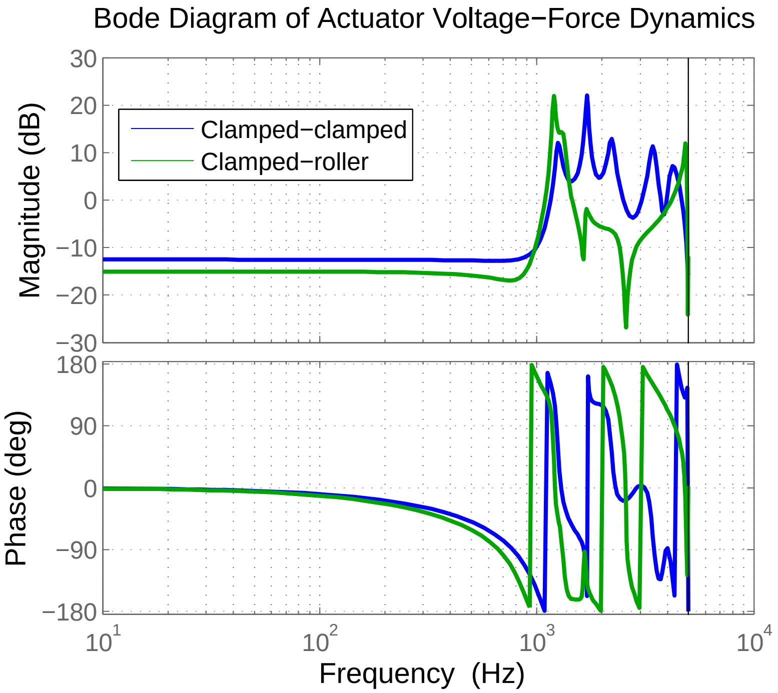

Figure 4.7: The identified model of a cantilever piezoelectric actuator shows that in the frequency range of interest for the FWMAV, the force output of the actuator is flat and in phase with the voltage input. This suggests that it is reasonable to treat the force as simply proportional to the applied voltage. High-frequency dynamics are ignored as they may arise from resonance of the clamp, sensor noise or other sources that are mistaken by the system identification model as dynamic behavior. Furthermore, the frequency range over 1kHz is not of interest for the FWMAV in question.

x to wing flapping angle ϕ using the dimensions defined in Fig. 4.8. $\phi(x)$ is given by

$$\phi = cos^{-1}\left(\frac{(L_y - x)^2 + C_1}{C_2\sqrt{L_3^2 + (L_y - x)^2}}\right)$$
$$+tan^{-1}\left(\frac{L_3}{L_y - x}\right) + tan^{-1}\left(\frac{L_2 - L_4}{L_3}\right) - \frac{\pi}{2} \tag{4.2}$$

where

$$L_y = L_1 + L_2 - L_4 \tag{4.3}$$

$$C_1 = L_3^2 + (L_2 - L_4)^2 - L_1^2 + L_3^2 \tag{4.4}$$

$$C_2 = 2\sqrt{L_3^2 + (L_2 - L_4)^2}. \tag{4.5}$$

For small displacements, (4.2) can be simplified greatly, and the transmission simply acts as a lever, i.e.,

$$\phi = Tx \tag{4.6}$$

where $T = 1/L_3$. For the single-wing flapping device used in these experiments, the transmission dimensions are $L_1 = 300\mu$m, $L_2 = 500\mu$m, $L_3 = 300\mu$m, and $L_4 = 630\mu$m. The nonlinear and linearized kinematics for this geometry are plotted in Fig. 4.9. As expected, the small angle assumption is valid in the range of roughly ±15°, however the actual stroke angle begins to deviate from the linearized angle for larger actuator displacements. It is possible to optimize transmission linearity numerically by defining a cost function such as the square of the difference between the derivative $d\phi/dx$ and the ideal linear transmission ratio T, and minimizing this function using the *fmincon* algorithm in Matlab. The kinematics for an optimal geometry with link

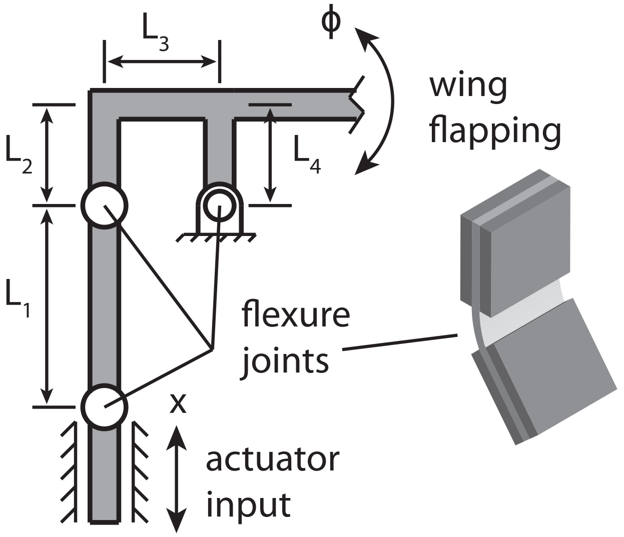

Figure 4.8: One-half of the fourbar transmission is pictured. The transmission kinematically relates actuator displacement x to wing flapping angle ϕ. Flexure joints (inset) act as revolute joints in parallel with torsional springs.

lengths $L_1 = 312\mu\text{m}$, $L_2 = 400\mu\text{m}$, $L_3 = 291\mu\text{m}$, and $L_4 = 498\mu\text{m}$ are shown in Fig. 4.9 as well.

Elastic deformation of the flexures stores potential energy and thus must be included in a dynamic model. While this element will be nonlinear due to the nonlinear kinematics, linearization of the kinematics means the flexures can be treated as torsional springs with spring constant k_t. Damping and inertia of the transmission flexures and linkages are neglected, as these values are quite small relative to the aerodynamic damping and inertia of the wings [83].

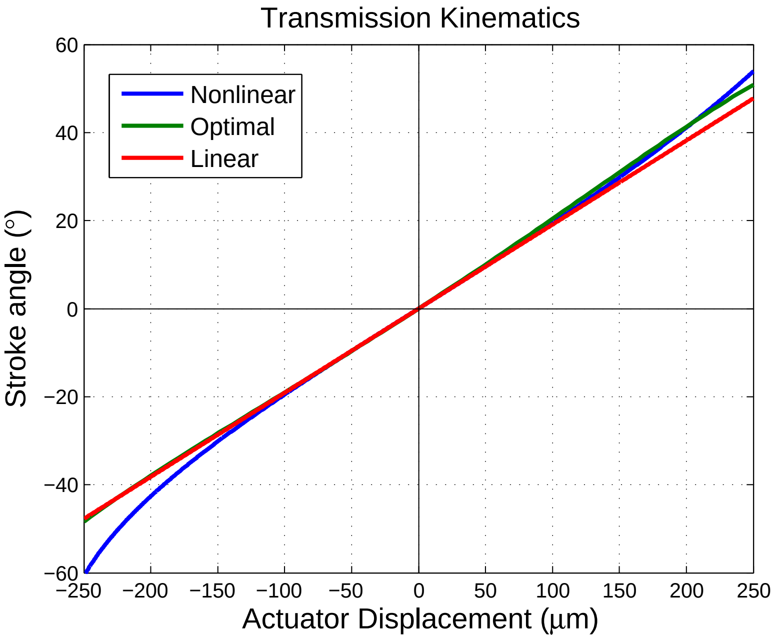

Figure 4.9: The nonlinear and linear transmission kinematics plotted for actuator motion ranging from ±250 μm. The linearization is quite accurate for wing motions up to ±20° and begins to deviate from the nonlinear kinematics as wing angles approach ±60°. Transmission geometry can be optimized to improve the linearity of the response.

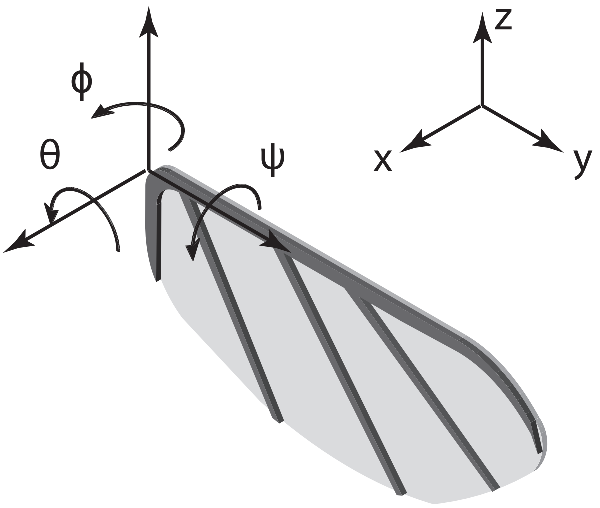

Figure 4.10: The global xyz coordinate system is fixed to the vehicle airframe. The wing flaps about the ϕ axis, which remains parallel with the global z axis. The ψ and θ axes rotate with the leading edge of the wing. In addition to flapping about the ϕ axis, the wing also rotates about the ψ axis. Deviations from a flat stroke plane (θ) are not addressed here.

4.3.3 Wings

Inertia

As discussed earlier, the wing flaps about one axis while rotating about its longitudinal axis (see Fig. 4.10). Coupling between these degrees of freedom leads to nonlinear terms in the equations of motion (for brevity the derivation is not reproduced here, see [89] for details). Analysis can be greatly simplified if the wing is treated as a rod rotating about a single axis ϕ, and the second axis of rotation ψ is ignored. This may be a reasonable assumption for a wing with a high enough aspect ratio (length/chord). To verify, we calculate the maximum kinetic energy of each rotational mode for typical wing kinematics: flapping at 100Hz with a stroke amplitude of 120°, and the angle of attack changing from 45° to 90° in one half of the half-stroke (i.e. one-quarter of a complete flapping cycle). This gives maximum angular velocities of $\dot{\phi} = 418$ rad/sec and $\dot{\psi} = 314$ rad/sec. The moments of inertia about the wing base, as calculated by a Solidworks model, are J_ϕ=45.3×10^{-12} kg×m^2 and J_ψ=1.7×10^{-12} kg×m^2. This gives maximum kinetic energies of

$$K_\phi = \frac{1}{2} J_\phi \dot{\phi}^2_{max} = 3.96\mu J \tag{4.7}$$

$$K_\psi = \frac{1}{2} J_\psi \dot{\psi}^2_{max} = 0.084\mu J. \tag{4.8}$$

Taking the ratio of these two terms gives

$$\frac{K_\phi}{K_\psi} \approx 47 \tag{4.9}$$

so we see that the vast majority of kinetic energy due to wing movement is stored in the flapping mode. Thus we can make the simplifying assumption that the inertial behavior of the wing is modeled by a beam with moment of inertia J_ϕ rotating about the ϕ axis (including inertia from the "added-mass" effect due to acceleration of the air, see [89]), and this behavior is linear.

Aerodynamics

The instantaneous aerodynamic force acting on the wing is typically broken into two components: lift and drag (F_L and F_D). We assume the aerodynamic energy terms are dominated by drag - i.e., the drag directly opposes motion of the actuator and thus dissipates energy; whereas we neglect the energy required to create a downward momentum jet of air during hover, and assume the lift force does no work against gravity if the altitude of the vehicle does not change. The drag force is a function of flapping angular velocity $\dot{\phi}$,

$$F_D = \frac{1}{2}\rho\beta C_D(\alpha)\dot{\phi}^2 \tag{4.10}$$

where ρ is the ambient air density, $C_D(\alpha)$ is an angle-of-attack-dependent drag coefficient (determined experimentally in [31]) and β is a coefficient that depends on wing geometry (see [89] for details). The drag force acts at the wing center of pressure, a distance r_{cp} from the base of the wing. For a linear model, we desire a linear damper of the form $F_D = b\dot{\phi}$ where b is the damping coefficient. The drag force can be linearized about an operating point $[\dot{\phi}_0, \alpha_0]$, such that

$$F_D = \rho\beta C_D(\alpha_0)\dot{\phi}_0\,\Delta\dot{\phi}. \tag{4.11}$$

Therefore b is given by

$$b = \rho\beta C_D(\alpha_0)\dot{\phi}_0. \tag{4.12}$$

Fig. 4.11 compares the nonlinear and linearized drag forces calculated using (4.10) and (4.11) over a full flapping cycle for typical flapping kinematics. We choose the point of maximum drag (which occurs at mid-stroke with $\alpha = 45°$) for linearization, thus the linearized drag force always overestimates the actual drag force, giving a "worst case" estimate for aerodynamic behavior.

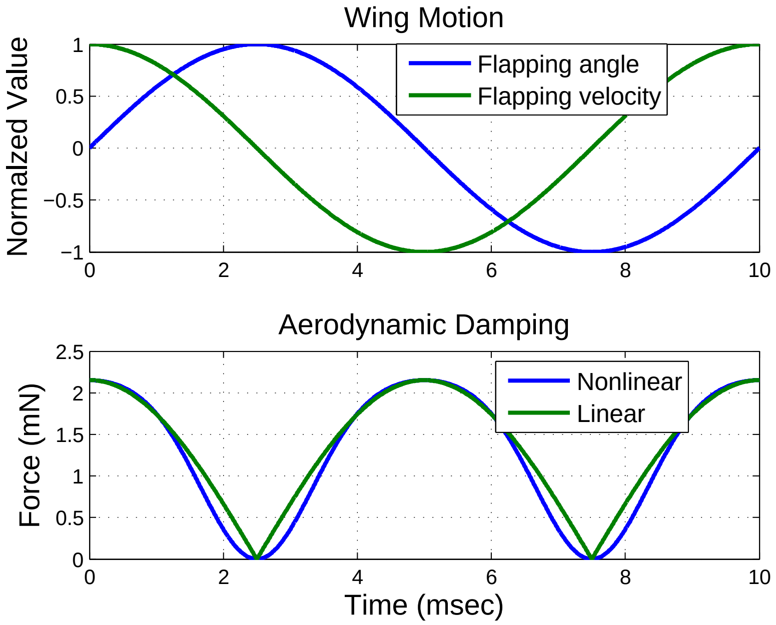

Figure 4.11: Nonlinear and linearized aerodynamic drag forces over one flapping period for typical flapping kinematics, calculated using (4.10) and (4.11). Note that by convention, drag force is always defined to be positive.

4.3.4 Complete model

Combining the linearized elements presented above yields the model pictured in Fig. 4.12, which is equivalent to that in Fig. 4.5. The equation of motion for this system is simply the classical result for a second-order spring-mass-damper,

$$m_{eq}\ddot{x} + b_{eq}\dot{x} + k_{eq}x = F \tag{4.13}$$

where, mapping all relevant terms to the x coordinate,

$$m_{eq} = m_a + T^2 J_\phi \tag{4.14}$$

$$b_{eq} = T^2 r_{cp} b \tag{4.15}$$

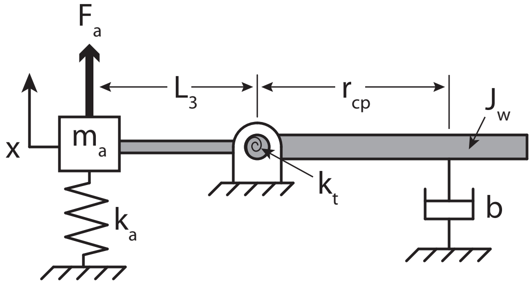

Figure 4.12: A diagram of the linear dynamic model.

Table 4.1: Physical parameters

Parameter	Symbol	Value	Units
Actuator mass	m_a	20	mg
Wing inertia	J_ϕ	45.3	mg·mm^2
Transmission ratio	T	2,857	rad/m
Radius to center of pressure	r_{cp}	10.1	mm
Aerodynamic damping	b	2.91	μN·s/m
Actuator stiffness	k_a	300	N/m
Transmission stiffness	k_t	5.4872	μN·m/rad
Equivalent mass	m_{eq}	390	mg
Equivalent damping	b_{eq}	0.2613	N·s/m
Equivalent spring constant	k_{eq}	344.8	N/m

$$k_{eq} = k_a + T^2 k_t. \tag{4.16}$$

Values for these parameters are given in Table 4.1. The transfer function relating actuator displacement to force is then

$$\frac{X}{F} = \frac{1}{m_{eq}s^2 + b_{eq}s + k_{eq}} \tag{4.17}$$

and we compare the Bode plot for this transfer function to the identified model P_I in the following section. For convenience, we refer to the theoretical model as P_T.

4.4 Comparison of Models

The theoretical linear model P_T from (4.17) is compared to the identified model P_I in Fig. 4.13. We see reasonable agreement between the magnitude responses of P_T and P_I, with resonant frequencies of 133Hz and 127Hz respectively. This gives an error of approximately 5%, a significant improvement over the roughly 50% error in [91] (170Hz predicted vs. 110Hz actual). It is well known that while there is a one-to-one mapping of poles from a continuous time system to a discrete time system, the zeros obtained from discretely sampling a continuous-time system can be complicated functions of the sampling frequency [6], and this can affect the phase response. Thus, it is not cause for concern that the phase responses of the two systems do not match well. However, we note that the magnitude response of P_T depends heavily on the state $[\dot{\phi}_0, \alpha]$ used for linearization of the aerodynamic damping. The terms m_{eq} and k_{eq} are dependent on intrinsic geometric and material system properties, and are not explicitly dependent on linearization about a state (unless the transmission ratio, T, is taken about a non-equilibrium position for the transmission, but we neglect this possibility). Choice of a different $[\dot{\phi}_0, \alpha_0]$ for (4.11) can result in either over or under-damping of the theoretical model (Fig. 4.14).

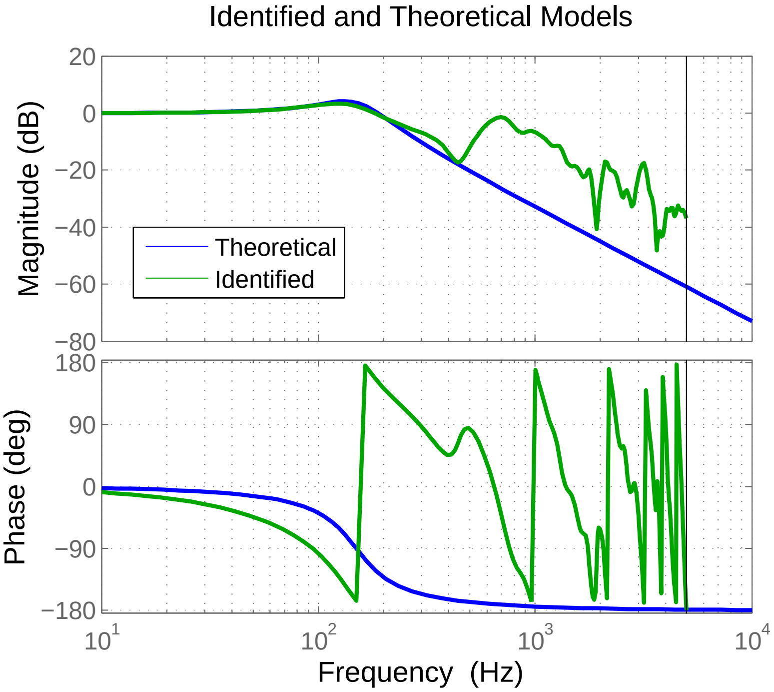

Figure 4.13: Bode plots for the theoretical and identified models P_T and P_I are in reasonable agreement for magnitude, with resonant frequencies of 133Hz and 127Hz respectively.

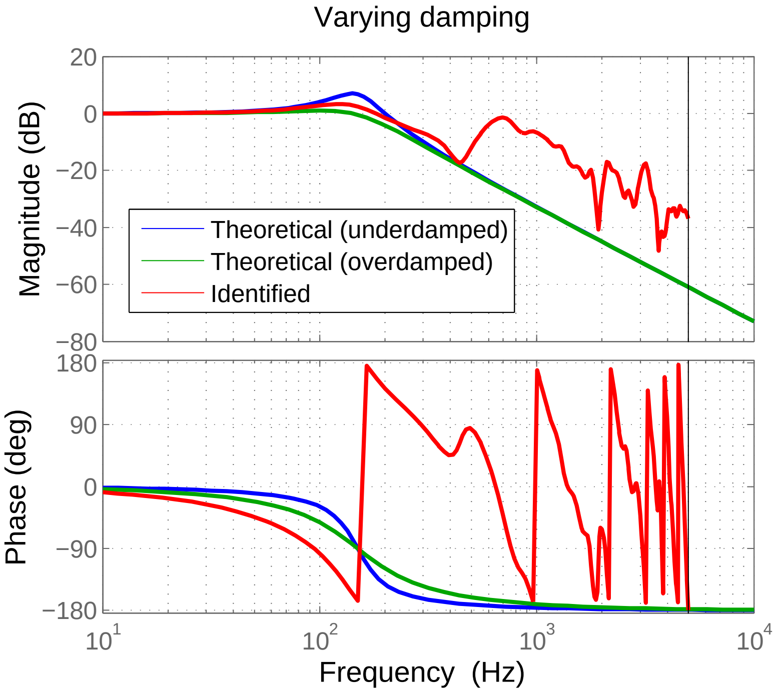

Figure 4.14: Taking kinematic data from [89] allows selection of different states for linearization of the aerodynamic damping. Selecting an angle of attack $\alpha = 30°$ results in an underdamped model, while $\alpha = 60°$ gives an overdamped model. The good fit in Fig 4.13 resulted from $\alpha = 45°$, and all three models use a flapping velocity of $\dot{\phi} = 392\text{rad/sec}$.

4.5 Implications for Vehicle Design

The original design of the Harvard Microrobotic Fly [91] presented the undamped natural frequency of the system as

$$\omega_n = \sqrt{\frac{k_{eq}}{m_{eq}}} \tag{4.18}$$

and there it is correctly stated that wing flapping inertia should be minimized in order to maximize resonant frequency. However, transmission optimization was purely kinematic, i.e. T was maximized (based on limitations of the fabrication process which placed a lower bound on L_3) in order to maximize stroke amplitude for a given actuator displacement. Since a voltage-driven piezoelectric actuator acts as a force source, not a displacement source, this approach is not entirely realistic, as it does not take into account the effects of the transmission ratio on dynamic behavior. Here, we present the damped resonant frequency

$$\omega_d = \omega_n \sqrt{1-\zeta^2} \tag{4.19}$$

in expanded form so the dependence on T can be seen:

$$\omega_d = \sqrt{\frac{m_a + T^2 J_\phi}{k_a + T^2 k_t}} \sqrt{1 - \frac{b_{eq}^2}{4\left(m_a + T^2 J_\phi\right)\left(k_a + T^2 k_t\right)}}. \tag{4.20}$$

This equation is plotted in Fig. 4.15 as a function of L_3 (remember that $T = 1/L_3$), and it is clear that, for the frequency range of interest, *resonant frequency increases with increasing* L_3 (for very large L_3, the system resonant frequency will asymptoti-

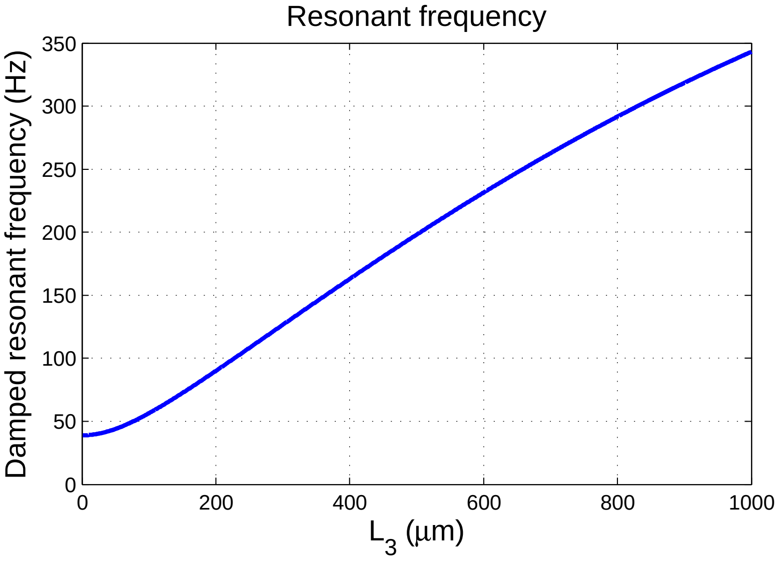

Figure 4.15: Plot of (4.20), showing that resonant frequency increases with increasing L_3 for the linearized model P_T.

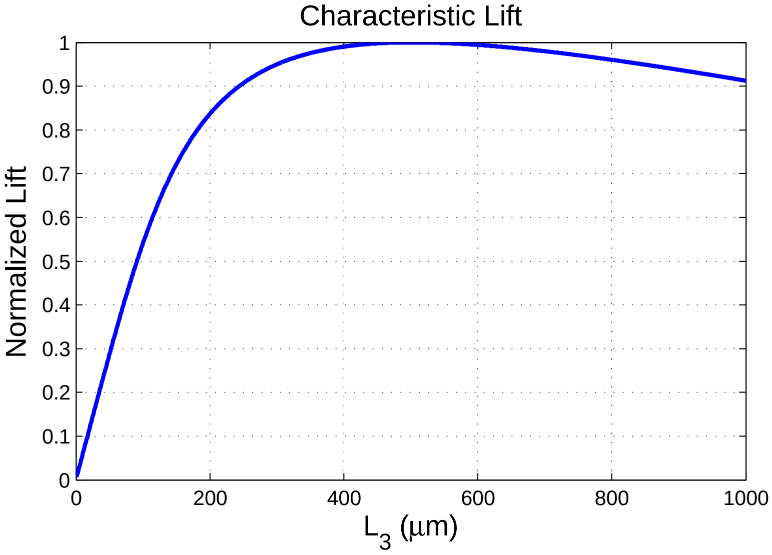

Figure 4.16: Characteristic lift force as a function of L_3 for the linearized model P_T.

cally approach the resonant frequency of the unloaded actuator). Thus, the claim in [91] that transmission ratio should be maximized conflicts with the desire to increase resonant frequency. This result does not simply imply that transmission ratio should instead be minimized to maximize resonant frequency, as this would result in very small stroke amplitudes - e.g., a vehicle flapping at 1kHz with only 5° of wing motion will likely generate negligible lift. Ultimately we seek to maximize the lift-to-weight ratio for a given vehicle, or maximize the lift force for a vehicle of fixed mass. For a linear model, as with the drag force, the lift force will be proportional to wing velocity. Thus we define a *characteristic wing velocity* as the product of resonant frequency and the stroke amplitude:

$$\dot{\phi}_{char} = |\phi|\omega_d \tag{4.21}$$

We use the DC stroke amplitude for this calculation, since, as discussed above, the magnitude at resonance is heavily dependent on the accuracy of the linearized damping term. The result, shown in Fig. 4.16, indicates that there is an optimal value for L_3 that gives maximum lift. Decreasing L_3 indefinitely will result in a decrease in both resonant frequency and resulting lift force - an important result not considered in the original vehicle design.

Note that this analysis hinges on the assumption that the passive dynamics of wing rotation, which play a vital role in lift generation (see [89] for details), will remain sufficient to generate lift. In reality, these dynamics are also frequency-dependent, i.e. at very low frequencies, not enough aerodynamic force will be generated to cause the wing to rotate, so the angle of attack will remain near $\alpha = 90°$ and little lift will be generated. Alternatively, at very high frequencies, high aerodynamic and inertial forces will cause the wing to "over-rotate" (i.e. α approaches 0°), and again, very little lift will be generated. Thus these results must be used with caution when extrapolated outside the neighborhood of flapping at 100Hz.

4.6 Discussion

We have presented a linearized second order model that provides a reasonable fit to an identified model of a flapping-wing MAV. The model provides a significant improvement over previous lumped-parameter modeling efforts, and proves sufficient despite the inherently nonlinear nature of the system. The model provides insight into the design of the MAV system for flapping at resonance, especially when considering the transmission mechanism that maps actuator displacement to wing motion. The model will serve as a useful design tool for vehicle scaling, e.g., designing components for a vehicle with a larger mass, which will likely have larger wings and actuators and thus a lower resonant frequency. Designing FWMAVs to flap at resonance is an essential part of maximizing power efficiency for systems with limited payload and lift/weight ratio.

Chapter 5

Instrumentation

Author's note: special thanks to Kevin Galloway for his help in the literature review of other existing torque sensor technologies, and design and fabrication of the supporting hardware for the torque sensor.

5.1 Introduction

It is standard practice in robotics to use multi-axis force and torque sensors to characterize the behavior of a robot and its interactions with its environment - for example, the ground-reaction forces on the feet of a terrestrial robot, or the body-frame torques on a helicopter. At typical larger scales, these sensors are commercially available and can be purchased as a pre-packaged set including mechanical interfacing hardware and electronic readout or associated software. However, the unique scale and operating conditions of the RoboBee mean commercially available experimental tools may not always be sufficient and thus custom designs are required. For example, the robotic fly presented in [93] required the development of a two-axis force sensor to empirically determine lift and drag forces generated by the flapping wings [95]. These sensors can be used to characterize input-output relationships between electrical drive signals to actuators and output body-frame forces and torques, and in turn this information can be used to guide development of control laws for free flight. This chapter presents detailed analysis of the design and fabrication of a single-axis torque sensor and a dual-axis force/torque sensor in this context.

The time-averaged torques predicted for the RoboBee in Chapters 2 and 3 are on the order of 1μNm. To the authors' knowledge, even the most sensitive commercially available torque transducers fall short of the range, resolution and bandwidth demanded for microrobotic experiments. For instance, the Nano17 by ATI Industrial Automation (Apex, NC) offers a torque measurement capacity of 120mNm and a resolution near 16μNm, which is an order of magnitude too large for our application.

There have been several published works on the development and manufacture of custom torque sensors for a variety of applications. One micro-torque sensor developed for the watch industry [47] uses differential force measurement to achieve a resolution of 50nNm over a working range of $\pm 200\mu$Nm. The device consists of a spring blade positioned perpendicular to the torque axis (i.e. not mechanically connected) with a piezoresistive force sensor chip at both ends of the spring blade. A perpendicular bar mounted on the torque axis acts on the spring blade via two adjustment screws. These screws allow the spring blade to be pre-stressed so that an applied torque will increase pressure on one force sensor and decrease pressure on the other. While this micro-torque sensor has adequate range, its resolution falls short of our 10nNm target (discussed below).

The most relevant previous work was presented in [45] and improved upon in [4], where a contactless torque sensor was developed for rotating micromotors. The torque sensor in [4] uses a cross-shaped spring element where one end is fixed and the torque is calculated by measuring the torsional deformation at the free end with a laser triangulation sensor. The published sensing range was $\pm 200\mu$Nm with accuracy down to 4μNm. There are design features of this device, namely the cross-shape sensor beam, that are found in our proposed design, however, there are several key differences. The tests in [4] were purely static and thus dynamic behavior of the sensor itself was not a concern. The sensor rotation axis and motor shaft were directly aligned, therefore off-axis loading was not an issue. In our case, high-frequency actuation of microrobots can lead to both excitation of resonant modes of the sensor and high off-axis loads. Consequently, this raises issues related to the sensor's bandwidth, resolution, and off-axis stiffness among others which are rigorously addressed in Section II.

At the MEMS level there are some proposed designs that fall within our desired sensing range [88, 17, 18]. Still, this approach has it owns challenges including 1) a fragile building material (i.e. silicon) which makes sensor calibration and usage difficult, 2) extremely small mounting features, and 3) poor resistance to out of plane loads, especially for the type of cantilevered torque experiments we desire to run.

Other micro-torque sensors have been developed for characterizing micromotors [74, 100, 68], however, these devices were designed for continuously rotating motor shafts and are not easily adapted to measure body torques generated by flapping-wing microrobots.

5.2 Sensor Design

5.2.1 Criteria

The concept of the proposed single-axis torque sensor is that a solid structure should deform measurably when a torque is applied about the desired axis, but deformations should be negligible under other loading. The sensor geometry must meet this demand while simultaneously being realistic to manufacture. The deformation of the structure must then be converted into a useful electrical signal - frequently an analog voltage which is correlated to a torque value. The methods for measuring deformation typically fall under two categories: contact and contactless. Strain gauges and differential force measurement are examples of the former while capacitive sensors and laser inferometers fall within the latter category. Each method has its limitations with regards to range, bandwidth, and sensitivity, and must be selected appropriately in tandem with the design of the torque sensor.

The sensor must be designed such that its static and dynamic parameters are appropriate for the intended application, in this case torque measurements of a robotic bee. The sensor geometry must be designed such that deflection under expected torque loading applied by the fly is appropriate for the output mode selected. For example, capacitive sensors used to measure displacement will have both an upper bound due to limited range and a lower bound due to limited resolution, or the torque sensor itself could fracture or plastically deform under loading. A larger displacement will lead to better sensitivity for a given output mode, as long as the output is not saturated. The sensor's bandwidth must be sufficiently high such that its operation is ideally quasi-static in the expected frequency range of wing flapping. Unfortunately, these static and dynamic criteria conflict. A mechanically stiffer sensor will be less sensitive but will have a higher bandwidth; whereas a more compliant sensor will be more sensitive, but will have a lower bandwidth. Thus, there is an inherent tradeoff between sensitivity and bandwidth that must be considered in the design and is discussed in more detail below.

There are other, more qualitative criteria involving the three-dimensional arrangement of the sensor itself, robotic bee, and supporting structures. Design criteria are summarized here, quantitatively when possible:

1. **Sensor topology**: Compliant in the desired axis with high off-axis rejection ratio (at least 100:1)

2. **Manufacturability**: The sensor geometry must be practical to manufacture at the scale of an insect-sized vehicle

3. **Range**: At least $\pm 100\mu$Nm, ten times the maximum expected torque output from a robotic fly

4. **Resolution**: Resolution of 10nNm, i.e. 0.01% of maximum torque range

5. **Bandwidth**: Sensor resonant frequency should be at least 1kHz (10 times the typical flapping frequency of 100Hz)

6. **Sensitivity**: $\pm 100\mu$Nm should correspond to approximately ±10V analog output, i.e. a sensitivity of 100mV$/\mu$Nm.

7. **Spatial considerations**: Sensor and supporting structure must avoid collisions

with flapping wings and allow clear camera views for high-speed video of wing motions

These criteria are evaluated in detail below in order to arrive at a final sensor design. It is important to emphasize that many of the criteria are coupled. This therefore requires an iterative design process to converge on a solution that falls within the allowable limits of the design criteria.

5.2.2 Sensor Topology

As a starting point, we select a sensor topology. A cantilever beam with an appropriate cross section can serve to be compliant to a torque about the longitidunal beam axis, yet insensitive to torques about orthogonal axes and transverse or axial forces, (i.e. a high off-axis stiffness). A cross-shape cross section is analyzed in [86] as a suitable design for a flexible revolute joint due to its high off-axis stiffness. A "slotted tube", shown in Fig. 5.1, is also a viable option with high off-axis stiffness. We choose the cross-shaped design for purposes of manufacturability. Steel shim stock can be laser-machined in two dimensions and then assembled to form a three dimensional beam, similar to the process in [95], eliminating the need to machine a slit into a small metal tube. The cross-shape also has the advantage of being more symmetric to off-axis loading as compared to the slotted tube which is more sensitive to lateral forces in the x-direction than in the y-direction (axes defined in Fig. 5.1).

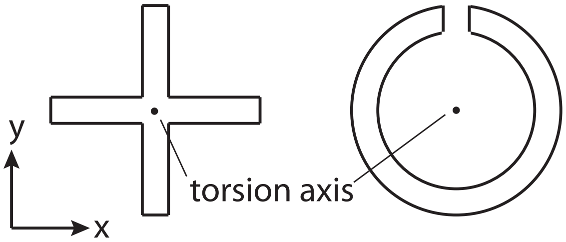

Figure 5.1: Cantilever beams with cross (left) and slotted-tube (right) cross-sections are compliant to torques about the beam axis but insensitive to other loading.

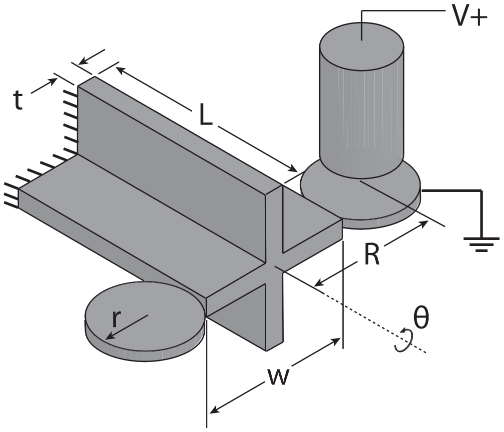

Figure 5.2: Dimensions that define the sensor geometry. Electrical connections to the capacitive probe head and target plate are also shown.

5.2.3 Output Mode

Capacitive sensors have proven useful in similar applications [95] due to their high sensitivity and bandwidth. A capacitive sensor consists of a probe head that forms a capacitor with an electrically grounded target plate. Motion of the target plate causes a measurable change in capacitance which is calibrated to displacement, force, or in this case, torque. Mounting a target plate to the edge of a cantilever beam allows measurement of the displacement of the plate when a torque is applied to the beam (Fig. 5.2). Despite their good bandwidth and sensitivity, capacitive sensors do have some drawbacks. One disadvantage is their typically small operating range (on the order of tens of microns), which requires very precise, parallel alignment of the probe head with the target plate. This small operating range also makes them susceptible to drift due to thermal expansion of components such as the sensor itself or surrounding support structures. The addition of a target plate also adds mass to the sensor, which will lower the mechanical resonant frequency of the beam and thus decrease the sensor bandwidth. Selection of capacitive sensors with appropriate specifications is discussed in Section 5.3.

5.2.4 Analytical Model

The sensor geometry can be fully parameterized by the dimensions shown in Fig. 5.2: width w, thickness t, length L, target plate radius r and radius to the center of mass of the target plate R. We define R as a function of the width, target plate radius, and an additional offset d (i.e. the edge of the target plate does not necessarily need to abut the edge of the sensor beam, it can be cantilevered out on a support strut; this dimension is not shown in Fig. 5.2),

$$R = \frac{w}{2} + r + d \tag{5.1}$$

Given this geometry, [86] reports the torsional stiffness of such a beam as

$$k_\theta = \left(\frac{w}{t} - 0.373\right)\frac{4Gt^4}{3L} \tag{5.2}$$

where G is the shear modulus of the material. The total moment of inertia of the sensor about the θ axis is the sum of several components:

$$J_{tot} = J_{eq} + J_{ec} + J_{tp} + J_{fly} \tag{5.3}$$

where J_{eq} is the equivalent moment of inertia of the beam (since it is fixed at one end and twists along its length, this will be less than the moment of inertia of the beam as a rigid body), J_{ec} is the moment of inertia of the square end cap at the end of the beam (not pictured in Fig. 5.2), which serves as a flat surface to mount the device under test, J_{tp} is the moment of inertia of the target plates and support struts, and J_{fly} is the moment of inertia of the robotic fly and associated mounting hardware that will ultimately be attached to the end of the sensor. Note that by the parallel axis theorem, and accounting for both plates, J_{tp} is defined as

$$J_{tp} = 2\left(\frac{1}{4}mr^2 + mR^2\right) \tag{5.4}$$

The undamped resonant frequency of a spring-mass system is $\omega_n = \sqrt{k/m}$, so we have

$$f_n = \frac{1}{2\pi}\sqrt{\frac{k_\theta}{J_{total}}} \tag{5.5}$$

and we can use this as an approximation for sensor bandwidth (realistically the usable bandwidth will be lower than the resonant frequency). Next, for the static rotation θ of the sensor due to a torque τ applied by the fly, we have

$$\theta = \frac{\tau}{k_\theta} \tag{5.6}$$

and this rotation results in displacement δ_θ of the center of the target plate,

$$\delta_\theta = R\sin\theta \tag{5.7}$$

We also have the potential displacement of the target plate due to force F applied by the fly in the y direction,

$$\delta_y = \frac{F_y L^3}{3EI} \tag{5.8}$$

where I is the cross-sectional moment of area of the sensor beam. In order for the beam to effectively decouple torque and force measurements, we desire a high off-axis rejection ratio γ,

$$\gamma = \frac{\delta_\theta}{\delta_y} \tag{5.9}$$

for typical force and torque values F and τ expected from the fly.

Note that while δ_θ is the displacement of the *center* of the target plate, the target plate is actually undergoing translation and rotation. This could be a cause of concern for two reasons: (1) Capacitive sensors are typically designed and calibrated to measure displacements of parallel surfaces with a linear response, so the torque-to-voltage calibration could be nonlinear, and (2) the outer edge of the target plate will translate more than the center and could possibly collide with the probe head if the beam rotates too much. The latter concern can be alleviated simply through proper selection of geometric parameters; and while a linear calibration curve would be convenient, it is not necessarily required, thus this issue is not cause for excessive concern.

The concept of *sensor quality* is defined in [95] as the product of sensitivity and

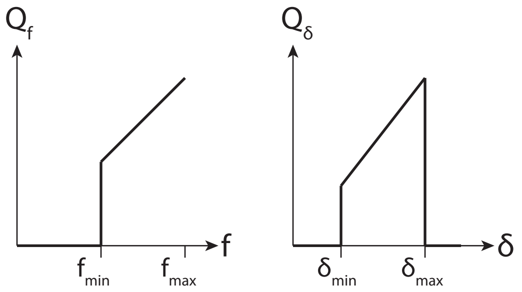

Figure 5.3: Components of the quality factor Q, Q_f and Q_δ, are defined to be zero outside the acceptable ranges of frequency and target plate displacement.

bandwidth, so in this case we have

$$Q = f_n \times \delta_\theta \tag{5.10}$$

since a higher f_n means a higher bandwidth and higher δ_θ means higher sensitivity. The quality factor is subject to two sets of constraints: (1) a minimum acceptable resonant frequency, determined by the expected frequency of the flapping tests, and (2) an acceptable range of target plate displacements, determined by the range and resolution of the capacitive sensor. Designs outside of this range are not considered, which is equivalent to setting the quality factor to zero (Fig. 5.3).

5.2.5 Finite element model

In order to validate the analytical model, a finite-element model in Comsol (Fig. 5.4) is used to calculate the static rotation of the beam due to an applied torque as well as the first few resonant modes. Figure 5.5 shows that the static rotation of the beam and resonant frequency calculated by the numerical simulations match the analytical model very well for varying beam geometries (different lengths and widths

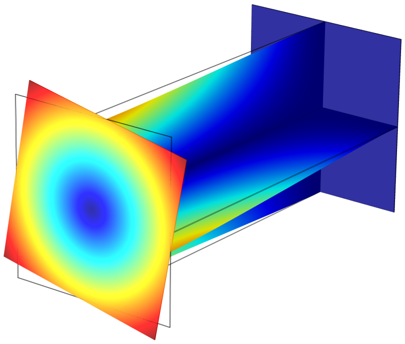

Figure 5.4: A finite element model is used to predict static deflection under applied load, and vibrational modes of the beam.

for a fixed thickness, ignoring target plate and fly inertia for now). Therefore, we accept the validity of the analytical model and proceed to use it to select an optimal design, as this solution approach is much faster than running multiple finite element simulations over a wide range of geometries.

5.2.6 Optimization

The techniques used to fabricate the sensor (discussed below) allow sheets of metal shim stock to be machined to any dimensions L and w, however shim stock is only available in discrete thicknesses t (without the use of a lapping machine to thin down stock material). Thus for an available sheet thickness of $t = 152.4\mu\text{m}$ we use the analytical model to calculate the target plate displacement δ_θ and resonant frequency f_n over a range of beam lengths and widths. Relevant physical parameters are given in Table 5.1. Using a cutoff resonant frequency of $f_{min} = 1000Hz$ and allowable target plate displacements of $\delta_{min} = 0.5\mu m$ and $\delta_{max} = 10\mu m$ gives the allowable range of geometries (Fig. 5.6).

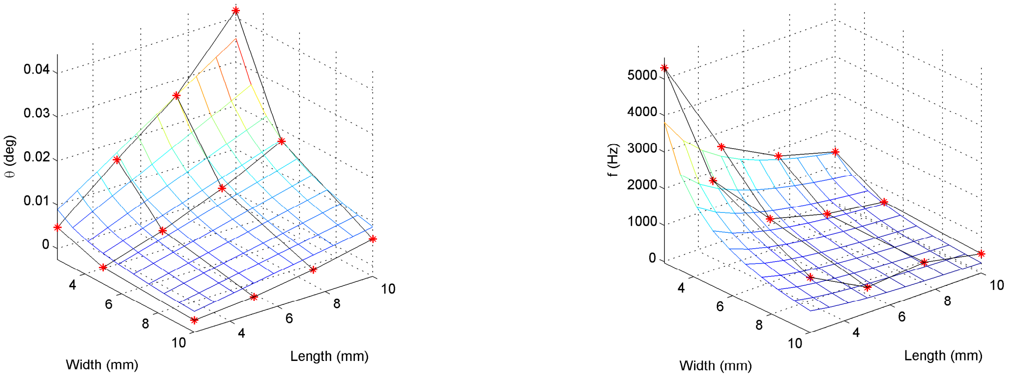

Figure 5.5: Finite element model simulations (red markers) predict both static beam rotation (top) and first resonant frequencies (bottom) in agreement with the analytical model (mesh grid).

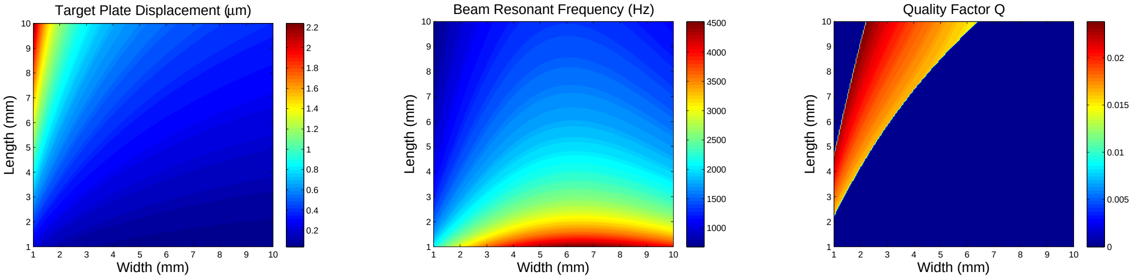

Figure 5.6: Sensor target plate displacement (left), resonant frequency (center) and quality factor (right) as functions of beam length and width. The quality factor is set to zero outside of the acceptable displacement and frequency ranges, giving the acceptable set of geometries for the final design.

Table 5.1: Material properties and other parameters

Parameter	Variable	Value
Invar elastic modulus	E	141Gpa
Invar density	ρ	8,100kg/m^3
Invar Poisson's ratio	ν	0.29
Target plate radius	r	1mm
Target plate offset	d	4mm
Fly moment of inertia	J_{fly}	1.1μgm^2
Maximum torque from fly	τ	10μNm
Maximum lift from fly	F_y	120mg

We select dimensions $w = 5mm$ and $L = 10mm$, which fall within the acceptable bounds. For these dimensions the beam resonant frequency is 1341Hz, the static torsion angle is 4.5×10^{-3} degrees, and the target plate displacement is $0.588\mu m$ (erring on the side of higher resonant frequency in case any inertias were underestimated). The predicted off-axis rejection ratio is $\gamma = 335$.

5.3 Sensor Fabrication

The sensor components are laser-machined from 6mil Invar shim stock using a 355nm diode-pumped solid state (DPSS) laser. Invar is selected due to its low coefficient of thermal expansion, in order to help mitigate calibration drift due to thermal expansion or contraction of the sensor beam. The 2D parts are then assembled (Fig. 5.7) and seams are laser-welded (Laserstar Technologies 1900 series). The high resolution of the laser machining system (roughly 5μm beam diameter) assures accurate assembly of the separate parts through mating features such as slots and tabs. The entire beam is laser-welded to a stainless steel block at the base, which is anchored to a base plate. Each capacitive sensor is mounted to a 5 DOF structure which allows precision alignment of the capacitive probe head with the target plate. The user has control over the capacitive sensor's X-Y-Z position, and a flexure mount holding the sensor offers up to 6° of pitch and yaw adjustability. While the system was designed with two target plates to allow differential readings from two separate capacitive sensors, the off-axis rejection ratio of the final design is high enough that only one sensor is necessary (a beam with a much lower off-axis rejection ratio and two capacitive sensors could serve as a dual lift/torque sensor). The capacitive sensor (Microsense model 8810 gauging system and model 2813 probe) was selected because the small probe diameter (2mm) allowed use of a smaller target plate, incurring less of a penalty on resonant frequency. The combined 8810/2813 system has a bandwidth of 10kHz, a range of $\pm 10 \mu m$, and resolution of roughly 0.6nm. This range gives the torque sensor a factor of safety of roughly 17 to avoid overloading or output saturation, a resolution of over 1000 divisions of full-scale expected output (predicted maximum target plate displacement divided by capacitive sensor resolution), and enough bandwidth to collect up to 100 data points per flapping cycle for flapping at 100Hz. A CAD model and photograph of the completed assembly are shown in Fig. 5.8.

5.4 Experiments

5.4.1 Static tests

For calibration, notches were laser-machined into the end cap of the beam at 1mm intervals that allowed calibration weights to be hung at varying radial positions. A small tray was also used to hang different weight combinations at the same radial

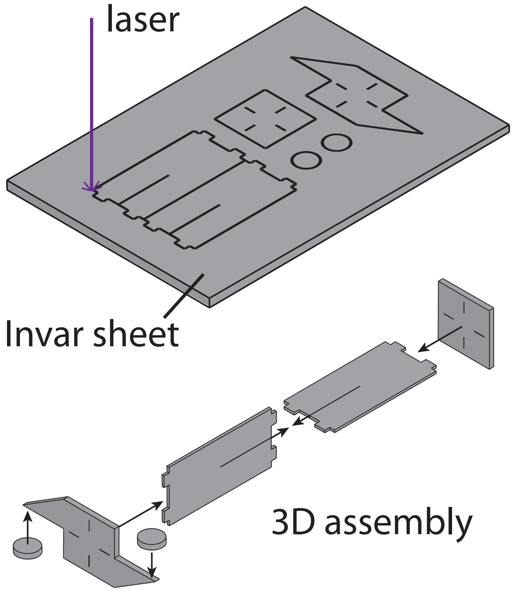

Figure 5.7: Sensor beam components are machined in 2D with a laser (top) then assembled in three dimensions (bottom). Seams are laser-welded to join the pieces together. Refer to Fig. 5.2 for relevant dimensions of the final assembly.

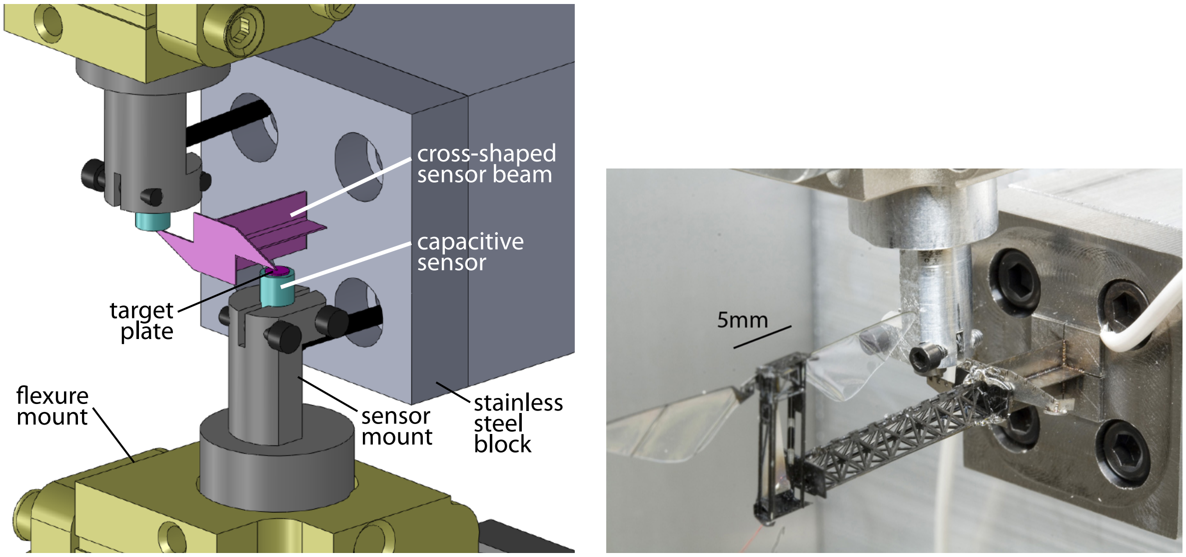

Figure 5.8: A CAD model (top) of the completed assembly including sensor beam, capacitive sensors and supporting fixtures, and photograph (bottom) of the completed experimental setup with a robotic bee attached to the faceplate of the sensor via a lightweight carbon fiber truss structure (required to avoid collision of the wings and the capacitive sensor).

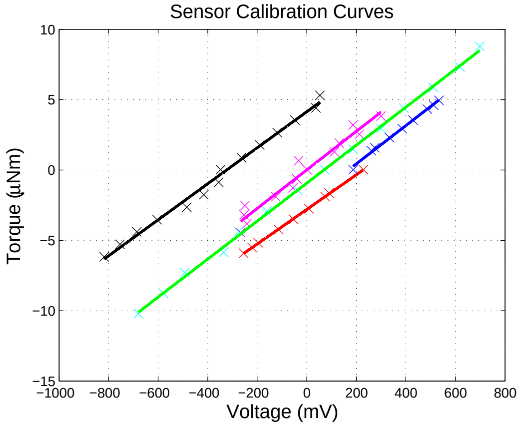

Figure 5.9: Sensor calibration curves. Each color corresponds to a single calibration process (the entire process takes several minutes), with multiple calibrations taken over a period of hours or several days. The "x" markers correspond to individual readings, and each line is a linear least-squares fit. Multiple sensor calibrations show that while the zero reading is subject to drift over time, likely due to thermal effects, the sensitivity remains relatively constant.

position. All of these calibration curves are presented in Fig. 5.9 and show an average sensitivity of 75.8 mV/μNm. The zero level is subject to thermal drift with a time constant of several minutes (Fig. 5.10), but since flapping-wing experiments will occur in fractions of a second, as long as a new zero reading is taken immediately before each experiment, distortions of the data due to thermal effects can be eliminated.

5.4.2 Dynamic Tests

The resonant frequencies of the beam with and without a RoboBee attached to the end are approximately 1.0kHz and 1.5kHz respectively, in close agreement with the analytical model and sufficient for flapping tests in the neighborhood of 100Hz. A 60mg prototype was mounted to the end of the sensor in the configuration shown in Fig. 5.11. This orientation allowed measurement of pitch torques generated by the wings during flapping. The lift and drag forces both contribute to the net pitch

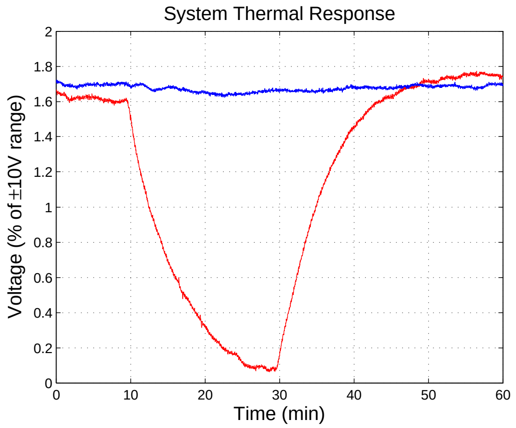

Figure 5.10: The system is subject to drift due to thermal expansion, and over long time scales this can be significant due to ambient temperature changes or air currents in the room (blue). A fiber-optic light source aimed directly at the sensor was used to determine the system's step response to a thermal input (red). The system's thermal time constant τ is approximately 6.5 minutes, so it requires about half an hour to reach equilibrium. Significant changes in the thermal environment, such as bright lighting, can cause voltage drift on the order of several percent of the full operating range. This should be taken into account when collecting data.

torque. For symmetric upstroke/downstroke flapping, the contribution to pitch from the drag force over one stroke cycle should average out to zero. That is, flapping in one direction, the drag force is opposite the direction of wing motion and the contribution to pitch torque will be positive. When the wing reverses direction, the drag force also reverses direction and thus the contribution to pitch is negative. In general, the lift force always acts upward and does not reverse direction on the upstroke or downstroke (although lift values may briefly go negative near stroke reversal due to inertial reactions, see [89]). Thus, changing the location of the average lift force vector over one stroke can change the average pitch torque acting on the vehicle (Fig. 5.12), and this fact will be useful for vehicle control and stabilization. For many small insects, the dynamics of wing flapping are typically an order of magnitude faster than body dynamics, therefore forces and torques averaged over several wingbeats can be

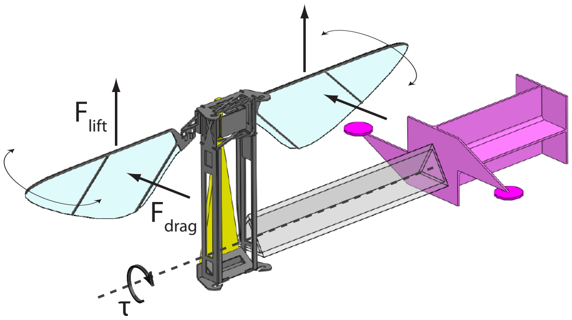

Figure 5.11: The RoboBee is mounted to the torque sensor in an orientation that allows measurement of pitch torques. Lift and drag forces act on the bee's wings as they flap back and forth, and both will contribute to the torque τ.

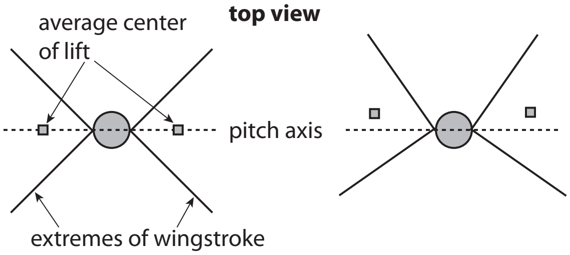

Figure 5.12: Nominally, assuming a symmetric vehicle and symmetric upstroke and downstroke flapping, the center of lift (i.e., location of the average lift force over one wingstroke) will act in-line with the vehicle's center of mass, and there will be no pitch torque (left). However, biasing the stroke forward or backward while keeping the amplitude constant will move the point of action of the average lift force away from the pitch axis, generating a torque (right).

sufficient for control purposes [28].

The RoboBee's wings are driven by a voltage-controlled piezoelectric actuator. To verify the proposed method for controlling average pitch torques, the wings were flapped at 100Hz with a drive signal amplitude of 200V, which corresponds to a stroke amplitude of approximately 100°, or a gain of 0.5°/V. The DC value of the control signal was varied over a range of ±25V, or about ±12.5° of stroke angle bias (note that these values are approximate - in future tests, stereoscopic imaging can

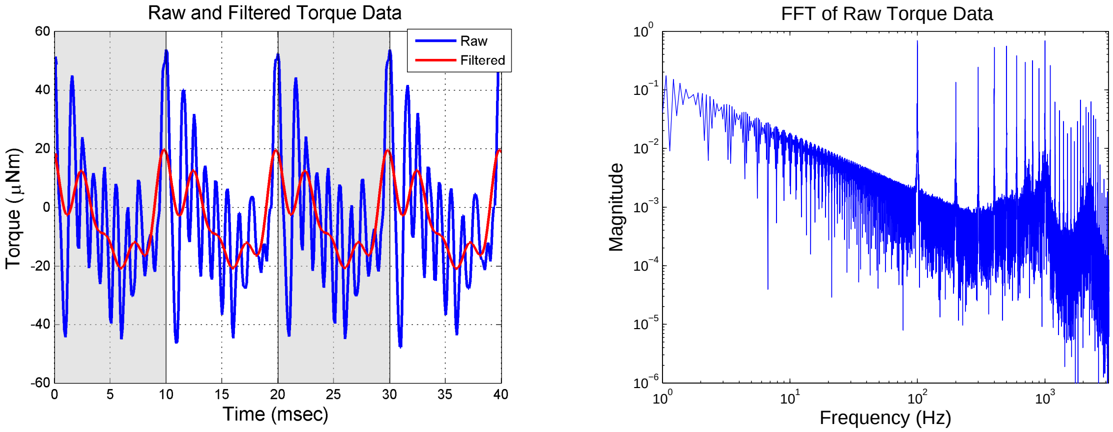

Figure 5.13: (left) Instantaneous torque values have contributions from drag, lift and inertial forces and are also affected by sensor resonance. A tenth-order Butterworth filter with a cutoff frequency of 800Hz is used with the *filtfilt* command in Matlab to eliminate the high frequency components of the signal without adding a phase delay, which allows decomposition of torque readings on a sub-period basis. Data from four wingbeat periods is shown (one period = 10msec) for the baseline flapping case with zero offset voltage. (right) An FFT of the signal shows that there are strong components at both the flapping frequency (100Hz) and the sensor resonant frequency around 1kHz.

be used to reconstruct exact wing position in 3D space, as in [89]). Instantaneous torque depends on contributions from both aerodynamic lift, drag and inertial forces (Fig. 5.11), however a running average (taken over ten wingbeats) shows a clear correlation between the offset voltage and the average torque value (Fig. 5.14). The sensor's high bandwidth allows characterization of contributions to torque with sub-period temporal resolution. If the resonant frequency of the sensor is sufficiently high relative to the flapping frequency, a low-pass filter can be used to eliminate signal components that arise due to sensor resonance (Fig. 5.13). When synchronized with wing kinematics, torque measurements would allow validation of aerodynamic models and decomposition of different contributions to net torque. This analysis is not presented here since 3D wing kinematics were not recorded, and for purposes of vehicle control, the important result is the time-averaged torque value.

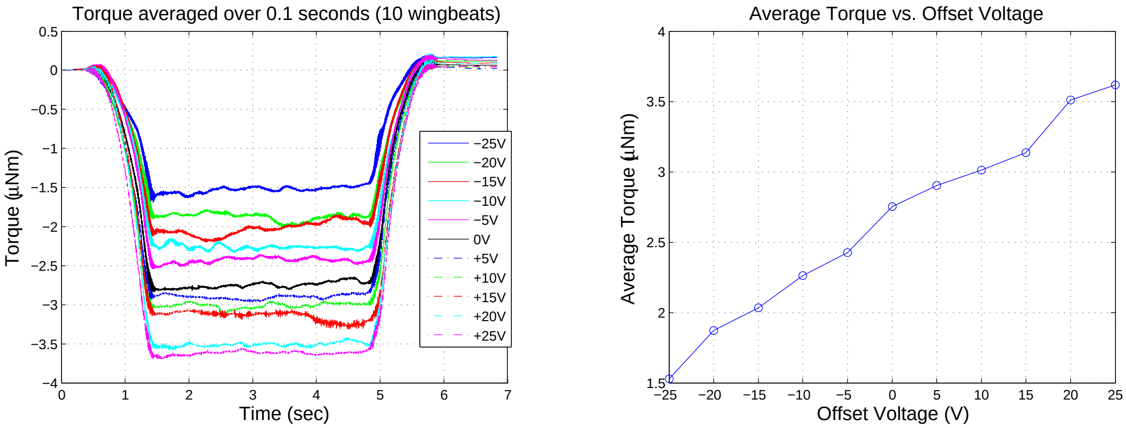

Figure 5.14: (left) A running average taken over 0.1sec (10 wingbeats) shows that controlling the stroke angle offset via an offset voltage can directly control the DC value of the torque measurement. The transients at the beginning and end of the data are due to slow ramp-up and ramp-down of flapping to avoid damage to the device under test. (right) Correlating this average torque value to the offset voltage command shows a roughly linear relationship, which will be useful for developing control laws.

Table 5.2: Actual Sensor Performance

Parameter	Value
Off-axis rejection ratio	335
Range	$\pm 130\mu$Nm
Resolution	4.5nNm
Bandwidth	1kHz
Sensitivity	75.8mV/μNm

Flapping tests at 110Hz resulted in saturation of the ±10V analog output of the capacitive sensor, corresponding to a range of $\pm 130\mu$Nm. The final performance of the sensor is summarized in Table 5.2.

5.5 Dual-axis force/torque sensor

While useful for preliminary control experiments, single-axis sensors are limited in that they only allow characterization of single-input, single-output (SISO) control systems. Achieving stable hover will require a multi-input, multi-output (MIMO) controller, and thus multi-axis sensors are useful. As discussed above, six-axis force/torque sensors are commercially available but not feasible at this size scale. Thus, as a next step, we present a two-axis force/torque sensor. The design methodology, analysis and fabrication are very similar to that presented for the single-axis torque sensor above, so we present a shortened version here.

5.5.1 Sensor Geometry

The sensor geometry and relevant dimensions are depicted in Fig. 5.15. It consists of four identical rectangular cross-section beams, mechanically grounded at the proximal end and connected to a rigid end cap at the distal end. Two target plates, whose displacement will be measured by a capacitive probe, are attached to the end cap. It is evident that if $d \equiv h$ and $t \equiv w$, the structure will be equally sensitive to forces in both the x and y directions. However, through proper adjustment of the cross-sectional aspect ratio of these rectangles (individual beams and center-to-center beam spacing), the sensor can be made sensitive to one force but insensitive to the other, while still remaining sensitive to torque about the z axis. This is discussed further in the modeling section below.

5.5.2 Analytical Model

The sensor must meet the same bandwidth and torque resolution criteria presented for the single axis-sensor, with the additional criteria of proper force range and resolution. We assume a peak force output of three times the bee's weight, or

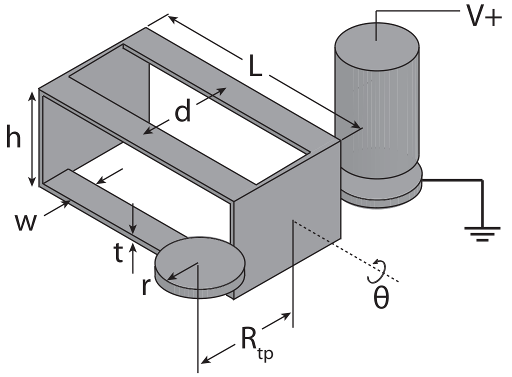

Figure 5.15: The relevant sensor dimensions: individual beam width and thickness t and w, beam center-to-center horizontal and vertical spacing d and h, beam length L, target plate radius r, and radius from the axis of rotation to the center of the target plate, R_{tp}.

about 1mN. Calculating the stiffness of the beam in the y direction is straightforward and is simply the sum of the stiffness of the four clamped-guided beams acting in parallel:

$$k_y = \frac{48EI}{L^3} \tag{5.11}$$

The torsional stiffness of the beam is slightly more complicated and is calculated using linear superposition and assuming small angles of rotation. The torsional stiffness of a rectangular beam about its centroidal axis is given in [67], and using this information we can construct the torsional stiffness of four of these beams arranged in the configuration presented above:

$$k_\theta = k_y \frac{d^2}{4} + 4\frac{w^3 t^3 G}{\alpha\left(w^2 + t^2\right) L} \tag{5.12}$$

where α is a parameter that depends on the aspect ratio t/w, given in [67].

In order to calculate resonant frequency (and thus sensor bandwidth), we must also calculate the equivalent mass and moment of inertia. The total equivalent mass is the sum of the components

$$m_{tot} = m_{eq} + m_{ec} + m_{fly} + 2m_{tp} \tag{5.13}$$

where m_{eq} is the equivalent mass of the four cantilever beams, m_{ec} is the mass of the end cap, m_{fly} is the mass of the robotic fly, and m_{tp} is the mass of a single target plate. The equivalent beam mass for all four beams, as presented in [95], is

$$m_{eq} = \frac{52}{35} m_b \tag{5.14}$$

where m_b is the mass of an individual beam.

The resonant frequency of the y mode is therefore

$$\omega_y = \sqrt{\frac{k_y}{m_{tot}}} \tag{5.15}$$

Similarly, we calculate the total moment of inertia,

$$J_{tot} = J_{eq} + J_{ec} + J_{fly} + J_{tp} \tag{5.16}$$

where the subscripts denote the same items as in Eq. 5.13. Note that we use the parallel axis theorem to compute all moments of inertia about the central axis of rotation of the sensor. Thus, we also have the resonant frequency of the rotational mode

$$\omega_\theta = \sqrt{\frac{k_\theta}{J_{tot}}} \tag{5.17}$$

Given maximum expected force output F and torque output τ from the bee, we can calculate the maximum predicted target plate displacement based on these loads and the stiffnesses:

$$\delta_y = \frac{F}{k_y} \tag{5.18}$$

$$\delta_\theta = R_{tp} \sin\theta \tag{5.19}$$

We can also define a “quality factor” as the product of sensitivity and bandwidth, for both the translational and rotational modes of the sensor:

$$Q_y = \frac{1}{k_y}\omega_y \tag{5.20}$$

$$Q_\theta = \frac{1}{k_\theta}\omega_\theta \tag{5.21}$$

This introduces a multivariable optimization problem since we have two possibly conflicting quantities that we want to optimize. So, we combine them into a single objective function and introduce a weighting factor β that scales the relative importance of the force and torque modes:

$$Q = Q_y + \beta Q_t \tag{5.22}$$

and we optimize this quantity subject to the following constraints, some of which prevent overlapping geometries, while others are performance criteria:

- $w, t, d, h, L, R_{tp} > 0$
- $d > w$
- $h > t$
- $R_{tp} > d/2 + w/2 + r$
- $f_y, f_t > 1000$Hz
- .5μm< δ_y,δ_t,< 5μm

The results of this optimization give the following optimal geometry (rounded to reasonable dimensions to make design and fabrication easier)

- $w = 1.5$mm
- $d = 6$mm
- $h = 3$mm
- $L = 6$mm
- $R_{tp} = 5$mm

5.5.3 Calibration

The dual-axis sensor is calibrated in the same manner as the single-axis sensor, by hanging weights at varying radial positions. This allows correlation of the measured force and torque to the two analog output voltages, as shown in Fig. 5.16. Fortunately this relationship is linear, and all the calibration points can be fit to a plane. Thus

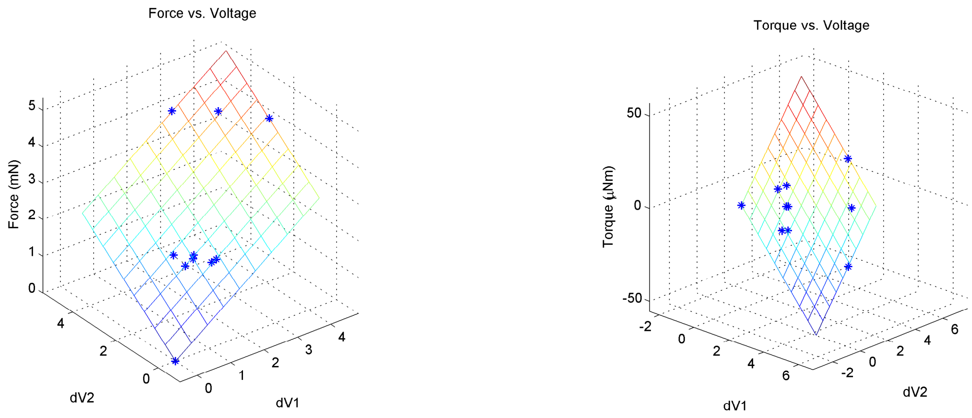

Figure 5.16: 3D calibration plots for the dual-axis sensor showing the relationship between force, torque, and the two voltage signals.

the calibration can be expressed as a 2x2 matrix that converts two voltages to force and torque. Using a least-squares regression to fit a plane through the calibration data points, this matrix is determined to be

$$\begin{bmatrix} F \\ T \end{bmatrix} = \begin{bmatrix} 4.5135 & 4.5747 \\ -70.2317 & 61.3911 \end{bmatrix} \begin{bmatrix} V_1 \\ V_2 \end{bmatrix} \tag{5.23}$$

where V_1 and V_2 are in units of volts, F is in mN and T is in μNm. The completed sensor is shown in Fig. 5.17, and with an attached RoboBee in 5.18.

For hovering flight control experiments, we will need to control the real torque about the center of mass of the fly, T_{com}. However, the torque about the center of mass of the fly will not necessarily coincide with the torque about the sensor's axis of rotation. Due to limits in the accuracy of the interface between the two parts, the center of mass of the fly may not coincide directly with the axis of rotation of the sensor. In that case, for example, there will be a contribution to the measured torque from the lift force due to a radial offset from the axis of rotation (Fig. 5.19). To

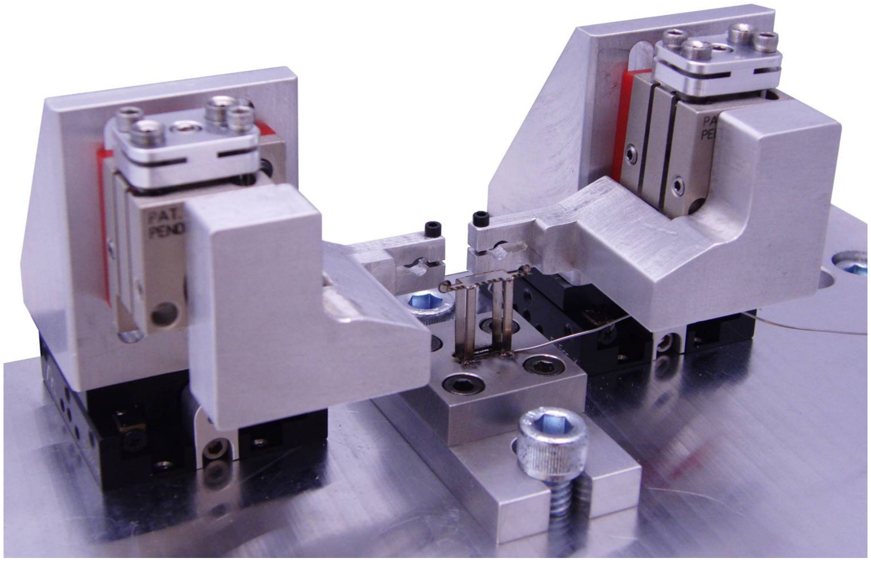

Figure 5.17: The completed dual force-torque sensor.

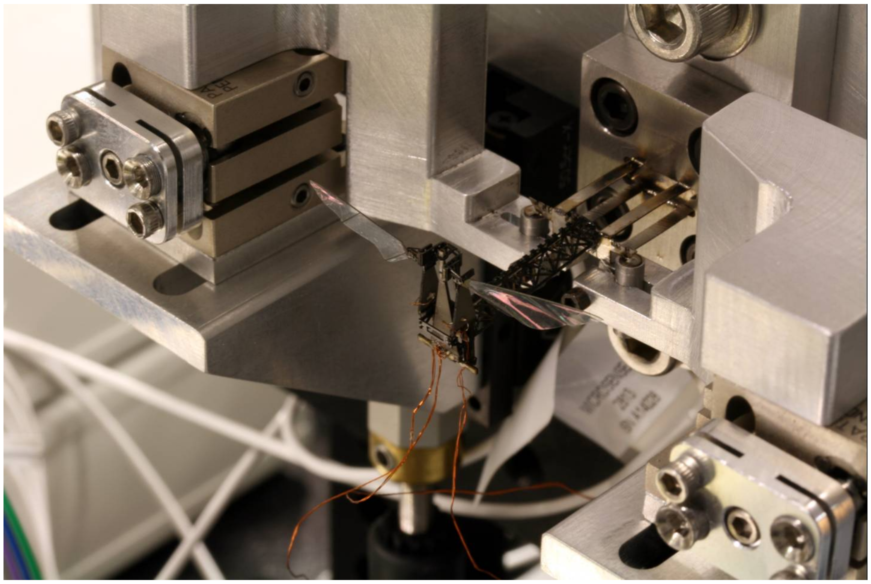

Figure 5.18: The completed dual force-torque sensor with a RoboBee attached via a carbon fiber truss.

formulate this problem more generally, due to other possibly unmodeled effects, we break the measured torque T_{meas} into three subcomponents:

$$T_{meas} = T_{com} + k_0 + k_1 F_{meas} \tag{5.24}$$

where k_0 is a term accounting for any inherent torque bias in the fly due to manufacturing asymmetries, and k_1 determines the contribution to the measured torque from the lift force F_{meas}. When the torque we wish to control, T_{com}, is zero, (i.e. we are not actively generating roll, pitch or yaw torques), Eq. 5.24 can be used to solve for the parameters k_0 and k_1 using a least-squares fit for a scatter plot of points (F_{meas}, T_{meas}). Then, for real-time control experiments, the equation can be rearranged to solve for T_{com} based on the measured force and torque F_{meas} and T_{meas} and the pre-determined constants k_0 and k_1. Finally, this information can be used to design a multi-input multi-output (MIMO) controller capable of decoupled, simultaneous control of force and torque. Lift force and roll torque data collected using the sensor during MIMO experiments performed collaboratively with Néstor Pérez-Arancibia are shown in Fig. 5.20, showing lift and roll being controlled with separate phases and frequencies.

5.6 Discussion

This chapter presented a single-axis torque sensor and dual-axis force/torque sensor used for characterizing the microrobotic bee's ability to generate body torques. The sensors also enable closed-loop system identification and feedback control experiments, as in [75]. The biggest challenge facing developments in this area is the

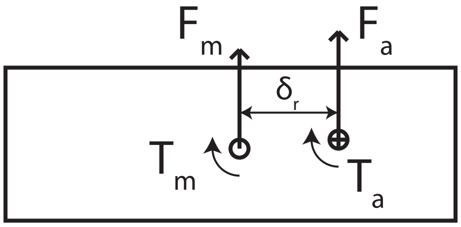

Figure 5.19: A schematic showing an end-on view of the sensor beam. The hollow circle represents the beam's center of rotation, and the circle with a cross through it represents the attachment point of the fly. The sensor measures force and torque F_m and T_m about its axis of rotation, however the applied torque T_a may be different than the measured torque due to error in positioning the robot relative to the sensor's axis of rotation, δ_r.

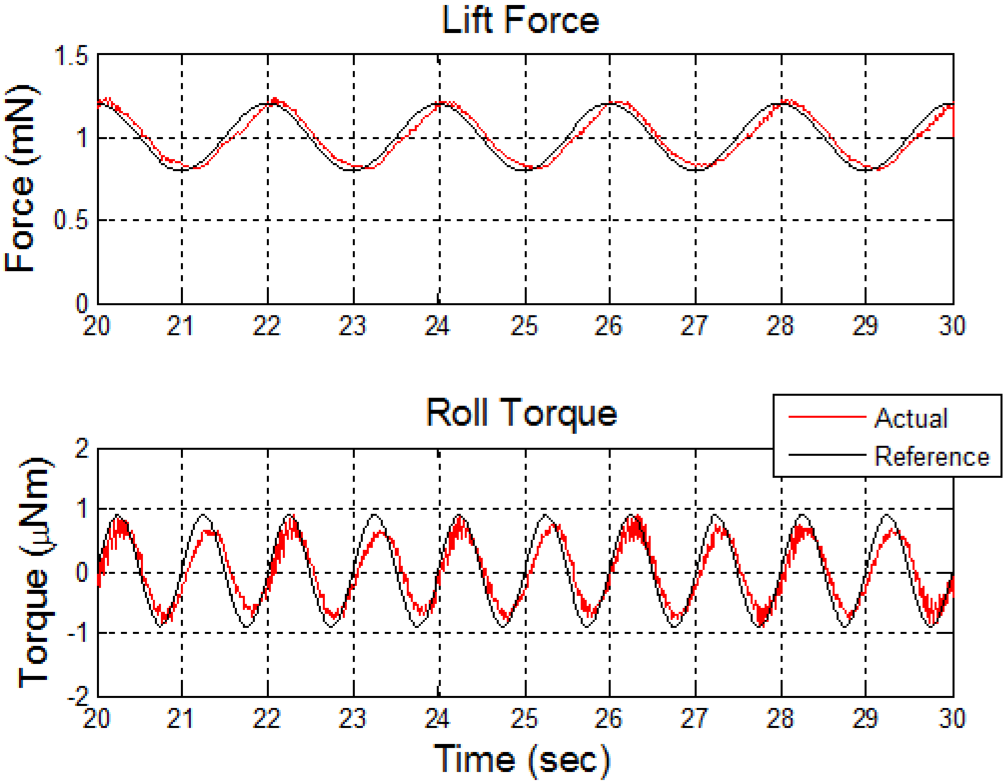

Figure 5.20: Decoupled lift force and roll torque measured using the dual-axis sensor during MIMO control experiments. Figure courtesy of Néstor Pérez-Arancibia.

construction of a six-axis force torque sensor, that would allow for full input-output characterization of all six body-frame forces and torques. Being limited to one or two axes of measurement at a time makes measuring coupling effects very difficult, and compensating for coupling between degrees of freedom may be essential for developing a controller for stable hovering flight.

Chapter 6

Open-Loop Torque Measurements and Steering Maneuvers

6.1 Introduction

This chapter presents the first roll, pitch and yaw torque measurements for an insect-sized FWMAV generated entirely via asymmetric wing motions. The rest of this chapter presents the strategies used to generate each torque, resulting torque measurements, and preliminary open-loop flight maneuvers.

6.2 Torque Generation

The principles for controlling roll and pitch torques were originally introduced in Chapter 2. Here we briefly review those principles and also introduce a method for controlling yaw torques with this design. An important principle for torque control is that the *wingbeat* dynamics are roughly an order of magnitude faster than the *body* dynamics - thus, body attitude can be controlled by controlling time-averaged, not instantaneous, forces and torques. This has been observed both in biological systems [46] and FWMAV experiments [71, 75]. This section addresses the general wing motions, and actuator signals specific to this design, required to generate all three torques. A schematic top-down view of the vehicle in hover with roll, pitch and yaw axes defined is shown in Fig. 6.1a for reference.

6.2.1 Wing Kinematics

Pitch torque can be controlled simply by shifting the mean stroke angle forward or backward. This can be accomplished with a single power actuator and does not require control actuators, and is depicted schematically in Fig. 6.1b. Measurements of pitch torque generated with this method were originally presented in [44], and used for single-DOF pitch attitude control in [75].

Roll torques are controlled via differential stroke amplitude - the control actuators are excited out-of-phase to increase the amplitude of one wing while decreasing the amplitude of the opposite wing. This has the advantage of generating a torque while keeping the total lift, and net load seen by the power actuator, approximately the same. This is depicted in Fig. 6.1c.

While roll and pitch torques can be controlled with parameters that can be varied slowly over several wingbeat periods, yaw torques require use of the control actuators on a sub-period basis to achieve *split-cycle* flapping ([73, 33] present a method for control with split-cycle flapping using independent wing actuation). When control actuators are used to change wing amplitude at a fixed power actuator frequency, this also changes wing velocity - i.e., in Fig. 6.1c, the left wing will have a higher velocity than the right wing since it is sweeping through a larger amplitude at the same frequency. If this amplitude differential is *switched* on the upstroke and the downstroke, then one wing will have a higher velocity on the upstroke, and the opposite wing will have a higher velocity on the downstroke. This creates an asymmetry in drag force on each wing over the wingbeat cycle, resulting in a net yaw torque. This is illustrated in Fig. 6.1d.

6.2.2 Actuator Signals

Each piezoelectric actuator is voltage-driven with a unipolar signal, typically ranging up to 300V (drawing about 100mW for the power actuator and several mW for the control actuators). Each actuator has three electrical terminals: a positive “bias” voltage, a signal voltage, and ground (Fig. 1.7). Note that for a bimorph actuator with a unipolar drive, zero displacement will occur when the signal voltage is equal to one-half the bias voltage. Thus, for drive signal V_i and bias voltage V_b, we can parameterize the drive signal of the ith actuator as

$$V_i = A_i \sin(\omega t + \phi_i) + \beta_i \tag{6.1}$$

where A_i is referred to as the amplitude and β_i as the offset. The parameters necessary for a constant time-averaged torque are defined for the power (V_1) and control (V_2 & V_3) actuators in Table 6.1 and depicted graphically in Fig. 6.2. Note that only the phases ϕ_i and offsets β_i are relevant for determining which torque is generated - the

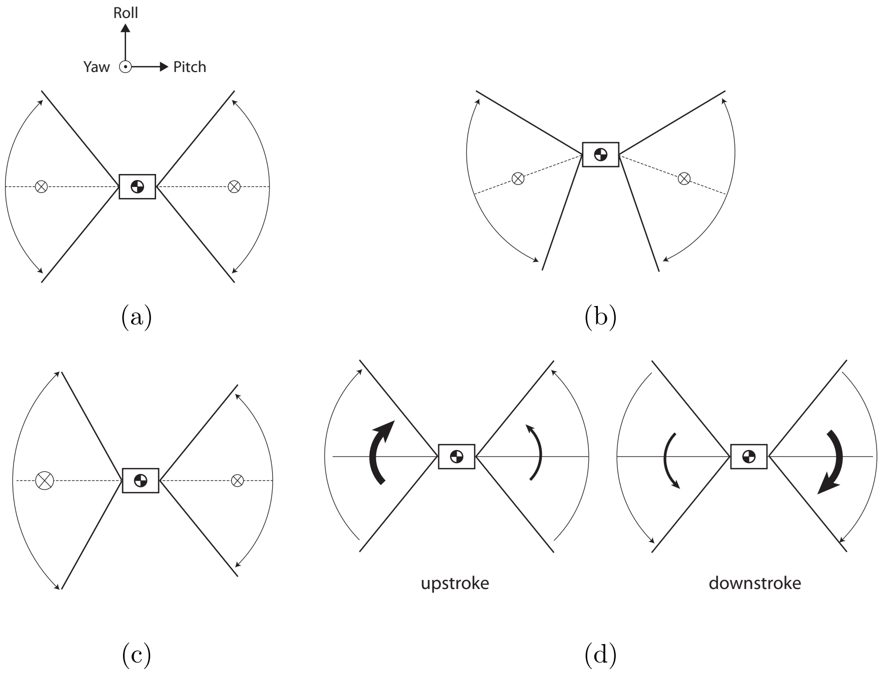

(a) (b)

(c) (d)

Figure 6.1: (a) Schematic of top-down view during hover with roll, pitch and yaw axes defined. For nominally symmetric flapping, the average total lift force from both wings passes through the body center of mass, resulting in no net torque. The $\otimes$ symbol represents the center of lift for each wing averaged over one wingstroke. (b) Pitch torque is controlled by shifting the mean stroke angle for both wings forward or backward, so the center of lift no longer passes through the center of mass. (c) Roll torque is controlled by keeping the power actuator signal constant while using the control actuators to asymmetrically increase/decrease wing amplitude, resulting in a larger lift force on one wing. (d) Yaw torque is controlled via split-cycle flapping - the wings have asymmetric velocities on the upstroke and downstroke, indicated by thicker and thinner arrows. This results in an asymmetric drag force on each wing over the stroke, and thus a net yaw torque.

Table 6.1: Actuator drive signal parameters

Parameter	None	Pitch	Roll	Yaw
A_1	> 0	> 0	> 0	> 0
ϕ_1	0	0	0	0
β_1	$V_b/2$	$> V_b/2$	$V_b/2$	$V_b/2$
A_2	0	0	0	> 0
ϕ_2	0	0	0	$\pi/2$
β_2	$V_b/2$	$V_b/2$	$> V_b/2$	$V_b/2$
A_3	0	0	0	> 0
ϕ_3	0	0	0	$3\pi/2$
β_3	$V_b/2$	$V_b/2$	$< V_b/2$	$V_b/2$

amplitudes A_i will simply scale the magnitude of the torque, and the frequency ω is the same for all three actuators.

For convenience, we define the following “control” voltages for each torque. For pitch,

$$V_p = \beta_1 - \frac{V_b}{2} \tag{6.2}$$

for roll

$$V_r = \beta_2 - \frac{V_b}{2} \tag{6.3}$$

and for yaw

$$V_y = A_2. \tag{6.4}$$

Note that for roll and yaw, the control actuator signals are always mirrored about $V_b/2$, so it is mathematically redundant to define another voltage based on V_3.

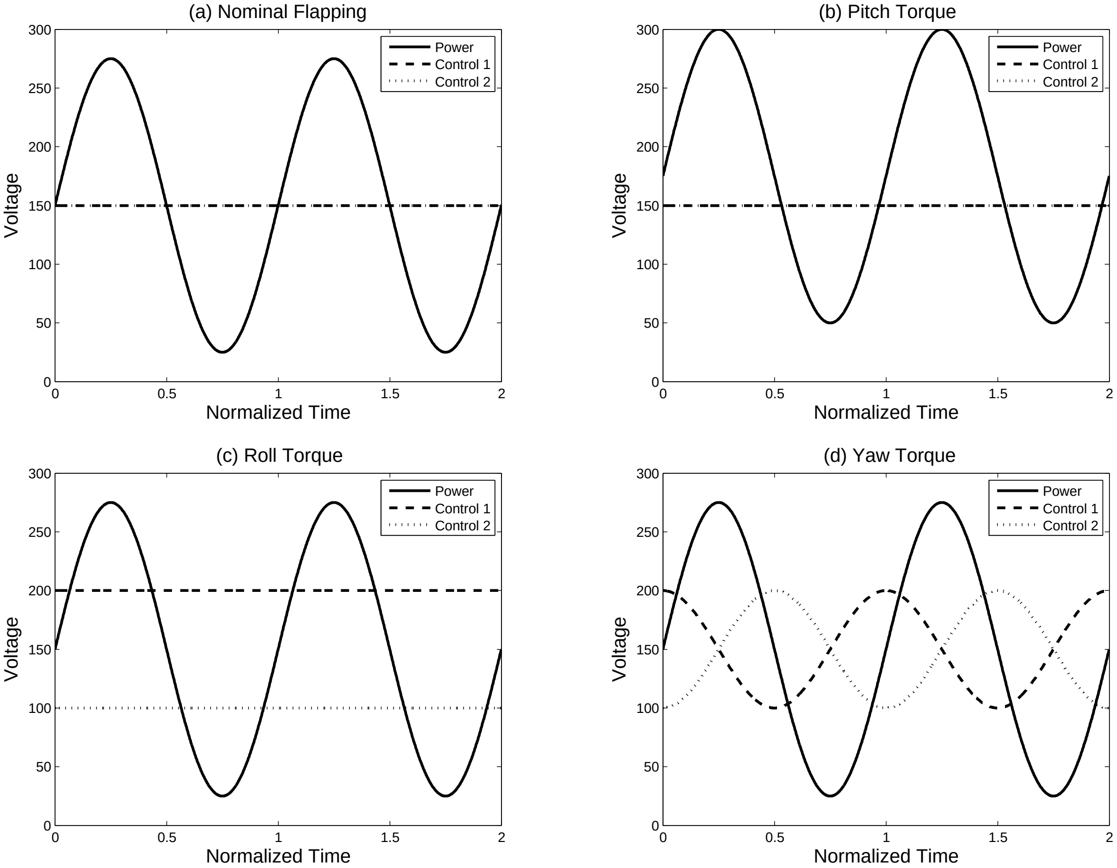

Figure 6.2: This figure depicts drive signals required for each body torque, assuming a 300V bias signal to the actuators, normalized over two flapping periods. (a) For nominal flapping and no torque, the control actuator signals are centered at 150V and the power actuator signal is symmetric about 150V. (b) For pitch torque, the control actuators remain centered at 150V, but the power actuator signal is shifted up (or down) - in this case centered at 175V. (c) For roll torque, the power actuator signal is again symmetric about 150V, but now the control actuator signals are constant and asymmetric about the midpoint, in this case 100V and 200V. (d) For yaw torque, all three signals are centered at 150V, but now the control actuators oscillate with 90° and 270° phase lags with respect to the power actuator.

6.3 Torque Measurements

The single-axis torque sensor from Chapter 5 was used to measure roll, pitch and yaw torques individually for the 110mg RoboBee prototype. The pitch torque data from Chapter 5 is reproduced here for completeness, and for the first time we present roll and yaw torque data for an insect-sized FWMAV. Torques in the range of $\pm 1\mu$Nm can be achieved about each axis, and these are compared to torques measured in several commonly studied insect species in Fig 6.4. Note that since testing conditions varied for the data collected on different insects in [19, 76, 70, 24, 59, 49], this is only an order-of-magnitude comparison for torques generated by insects of different sizes. It is not intended to indicate any definitive trend or scaling law, or claim that the RoboBee will be controllable based on its relative location on this plot. The torque generated by the RoboBee seems to be in the appropriate range relative to its mass when compared to biological data, although it is underperforming relative to honeybees of similar mass.

The experimental data is shown in Fig. 6.3 for time-averaged torques over a period of several wingbeats. All three torques show a very linear relationship with their respective control voltages V_p, V_r and V_y - surprising due to the nonlinear nature of the aerodynamic forces, but potentially beneficial for controller design. An additional test, varying the control actuator phase ϕ_2 with constant signal V_y (and the relationship $\phi_3 = \phi_2 + \pi$), shows that the values $\phi_2 = \pi/2$ and $\phi_3 = 3\pi/2$ maximize yaw torque (Fig. 6.3d).

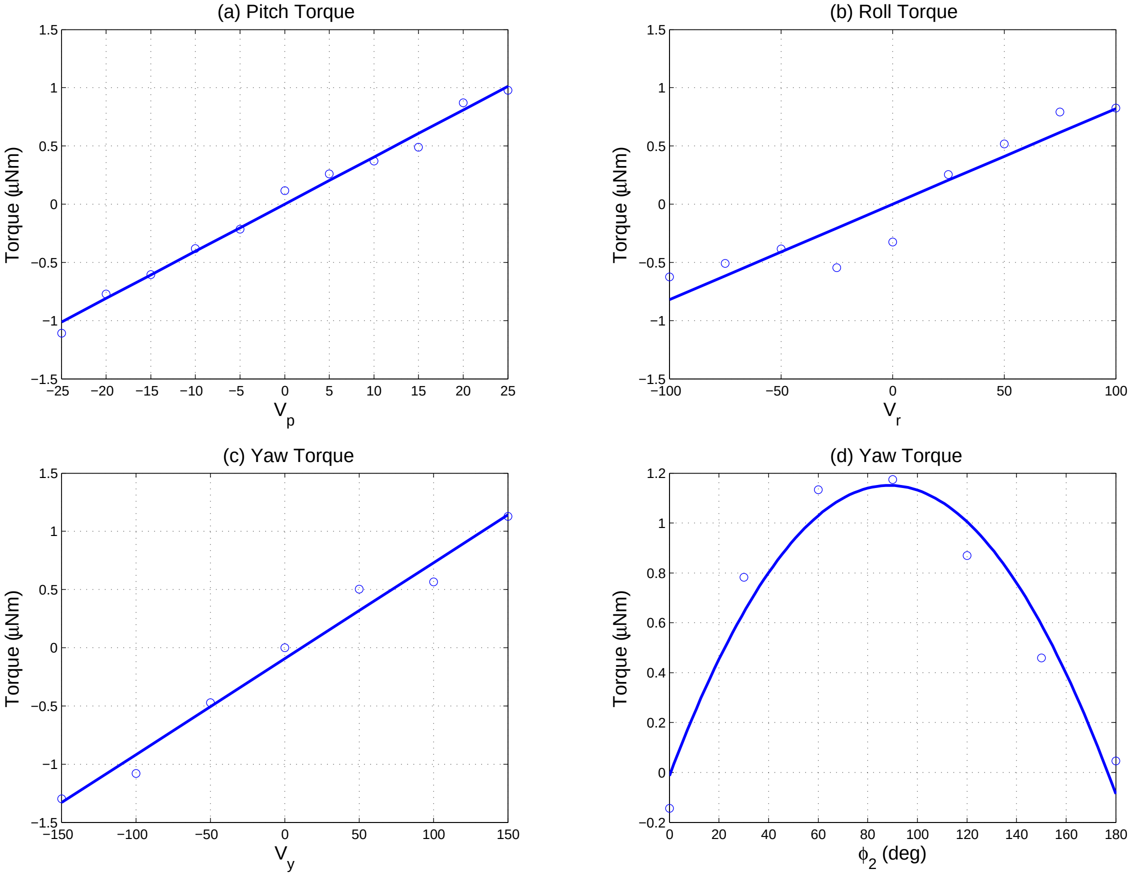

Figure 6.3: Torque data for (a) pitch, (b) roll and (c) yaw torques showing a linear relationship between control voltage and measured torque (data points are for torque averaged over several wingbeats with constant actuator drive parameters). (d) For a fixed amplitude V_y, yaw torque is maximized at $\phi_2 = 90°$.

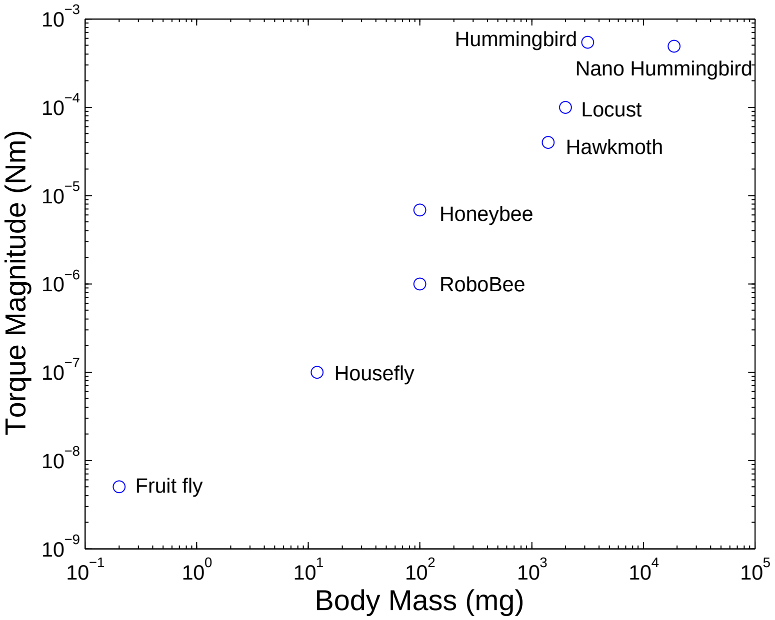

Figure 6.4: A log-log plot of typical torques measured during steering maneuvers for various insects: fruit flies (*Drosophila melanogaster*) [19], houseflies (*Musca domestica*) [70], honeybees (*Apis mellifera*) [59], hawkmoths (*Manduca sexta*) [24], locusts (*Locusta migratoria*) [76], and a ruby-throated hummingbird (*Archilochus colubris*) [49]. The Aerovironment Nano Hummingbird is also included [56]. Note that this data is *not* sufficient to claim that a vehicle will be controllable.

6.4 Open-loop flight maneuvers

As an intermediate step between torque measurements and controlled free flight, open-loop flight maneuvers were tested. Open-loop tests confirmed the ability to perform liftoff, pitch and roll maneuvers. Figure 6.5 shows combined frames from high-speed videos of open-loop "vertical liftoff", "roll left" and "roll right" trajectories. These initial results show that roll and pitch motions are not entirely decoupled; and attempts at open-loop yawing maneuvers were unsuccessful. Thus, a feedback controller that can compensate for coupling between the three axes of rotation will likely be required for stable flight.

6.5 Discussion

This chapter has presented the first results of an insect-sized FWMAV capable of liftoff with external power and direct control of roll, pitch and yaw torques. We do *not* claim that these torques are entirely decoupled. Due to the lack of a commercially available six-axis force/torque sensor with appropriate resolution for a vehicle of this scale, custom sensors such as those presented in Chapter 5 are required to measure forces and torques. Thus, measuring coupling between torques would require a multi-axis torque sensor, which has not yet been developed. However, preliminary results indicate that there is a high gain from each of the three control signals to the respective body torques, and open-loop maneuvers can be controlled without severe coupling issues. This is a promising indication for the success of free flight.

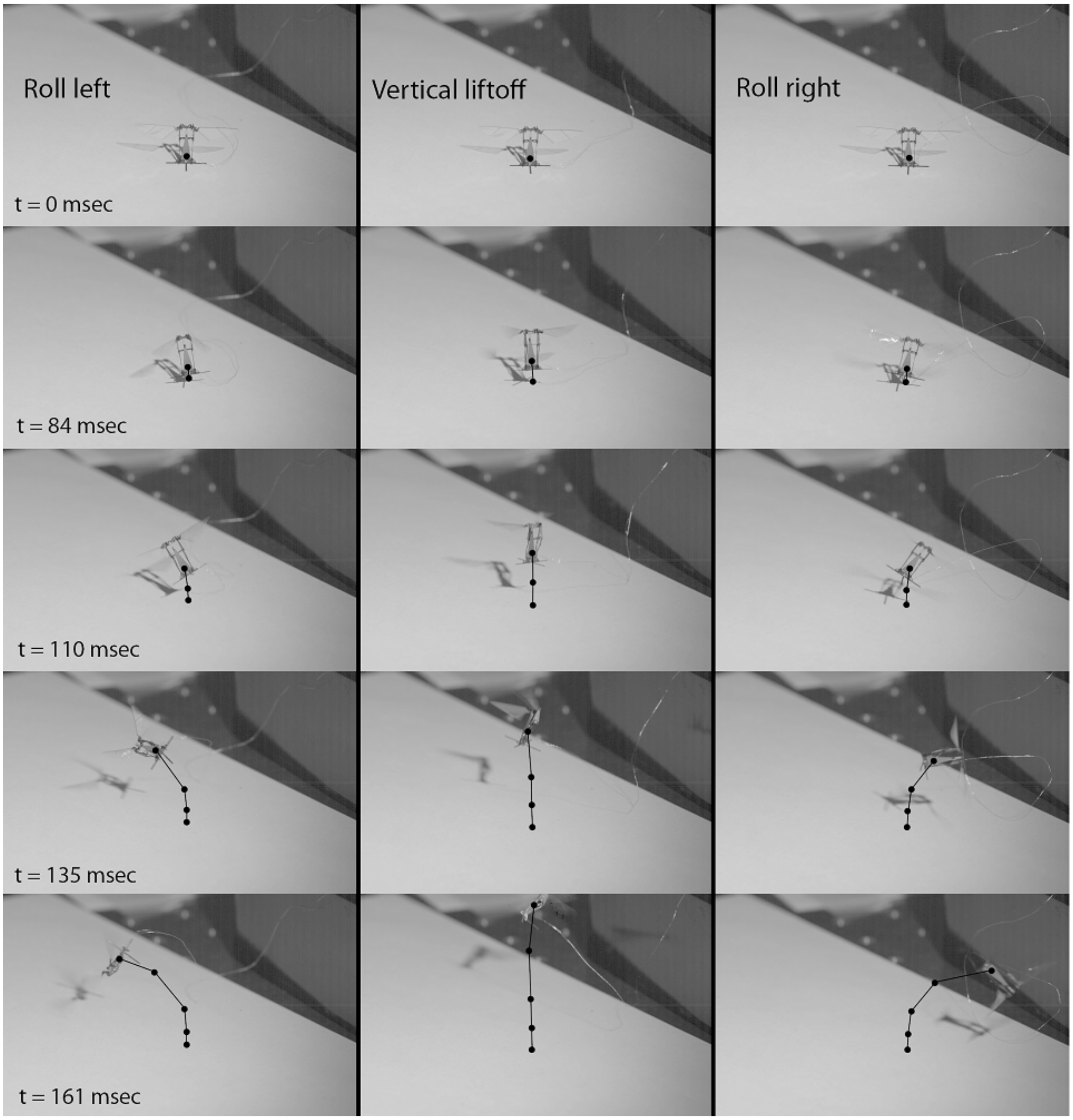

Figure 6.5: High-speed video frames showing open-loop flight maneuvers (filmed at 1000 frames per second with a Phantom V7.10 high-speed camera from Vision Research). Vertical liftoff (center column), roll left (left column), and roll right (right column) trajectories are shown. The trajectory history is overlayed on each frame, with a dot representing the approximate center of mass. Videos are available as supplemental material to the electronic version of the thesis.

Chapter 7

Controlled Flight

Author's note: I collaborated with Néstor Pérez-Arancibia on all the experiments presented in this chapter.

Following the torque measurements and open-loop flight maneuvers from the previous chapter, we performed controlled flight experiments. The initial goal was to obtain stable vertical ascent, i.e. controlling pitch and roll angles to keep the fly upright, while leaving altitude control open-loop. We did not attempt to control yaw orientation during these tests.

The RoboBee's position, velocity, and angular orientation were recorded real-time with a Vicon motion capture system. This information was fed into a controller in the Matlab xPC environment, which generated analog voltages to drive the RoboBee's actuators (first passing through high-voltage amplifiers). A schematic of the control system is shown in Fig. 7.1. The controller consists of two decoupled PID loops for pitch and roll (Fig. 7.2). We manually tuned the PID gains over dozens of flight trials until we achieved successful vertical liftoff, however flight distance was limited

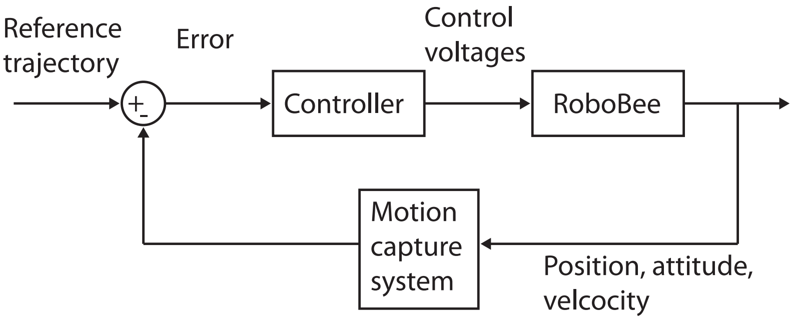

Figure 7.1: A block diagram of the closed-loop system used for flight control experiments. The position, attitude, translationan and rotational velocities of the RoboBee are recorded real-time using a motion capture system (Vicon). These values are compared to a reference trajectory, and the error is fed into the control block. The controller outputs signals to drive the piezoelectric actuators, which are amplified through a high-voltage amplifier (not shown in the diagram).

by the length of the power tether.

A composite image from video of the final, most successful flight trial is shown in Fig. 7.3. Three-dimensional trajectories from several representative trajectories are shown in Fig. 7.4. 2D projections of these trajectories are shown in Fig. 7.5.

The RoboBee used in these tests broke after approximately 100 trials. Fabrication remains a significant challenge, as additional copies of the device failed to reach the same level of performance, typically due to a severe inherent torque bias resulting in saturation of the controller. This highlights the need for reliable, repeatable manufacturing of symmetric devices. The next step in controlled flight is to design a MIMO controller to simultaneously control both attitude and position in three-dimensional space. This work is ongoing at the time of publication of this thesis.

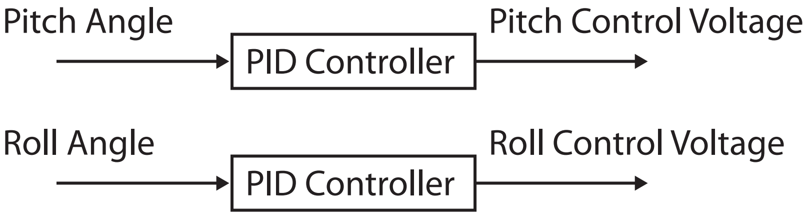

Figure 7.2: The controller used in the flight control experiments consisted of two decoupled PID SISO control loops, one for pitch and one for roll.

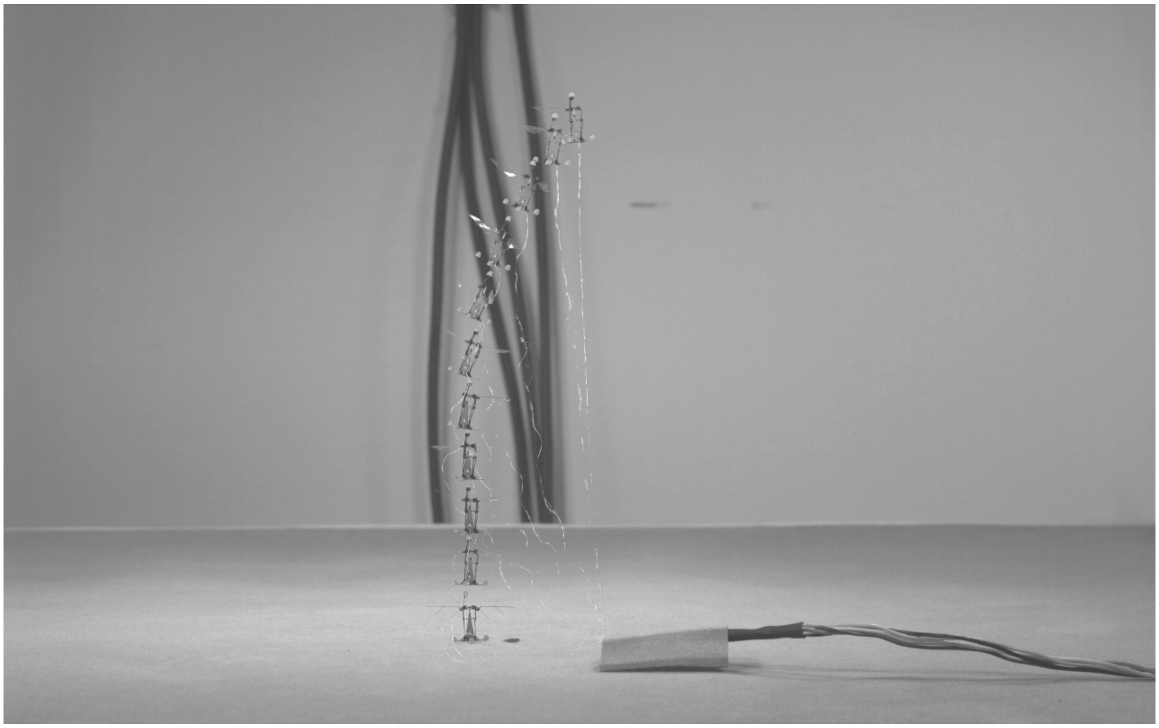

Figure 7.3: Composite image of video frames from the most successful controlled vertical flight attempt. This video is available as supplemental material in the electronic version of the thesis.

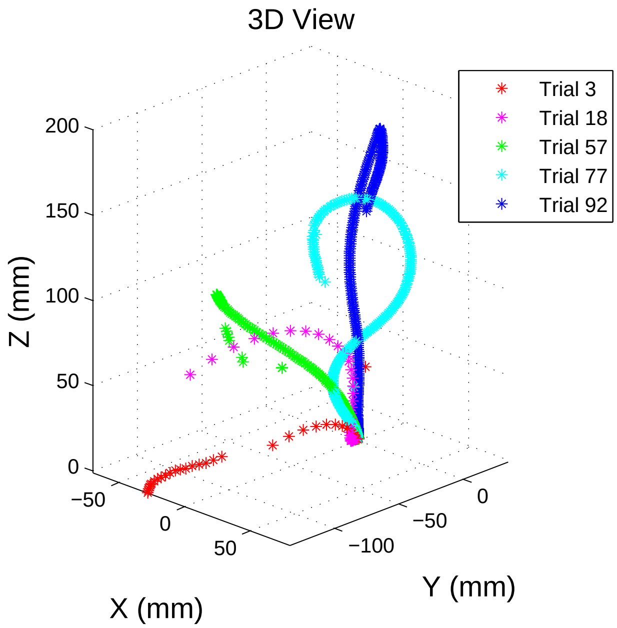

Figure 7.4: Three-dimensional trajectories as recorded by the Vicon motion capture system for various controlled flight trials. The tests range from early failures (Trial 3 in red) to the most successful test (Trial 92 in blue).

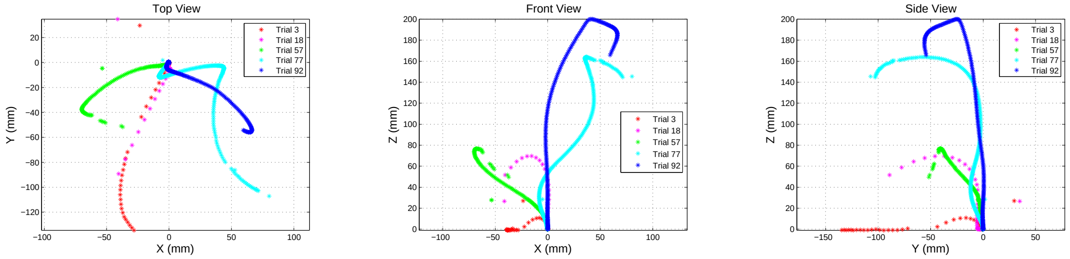

Figure 7.5: 2D projections of the same flight trajectories from Fig. 7.4 into the XY, XZ and YZ planes. The most successful trial (92) is limited by the length of the power tether, resulting in the sharp kink at the top of the plot when the end of the tether is reached.

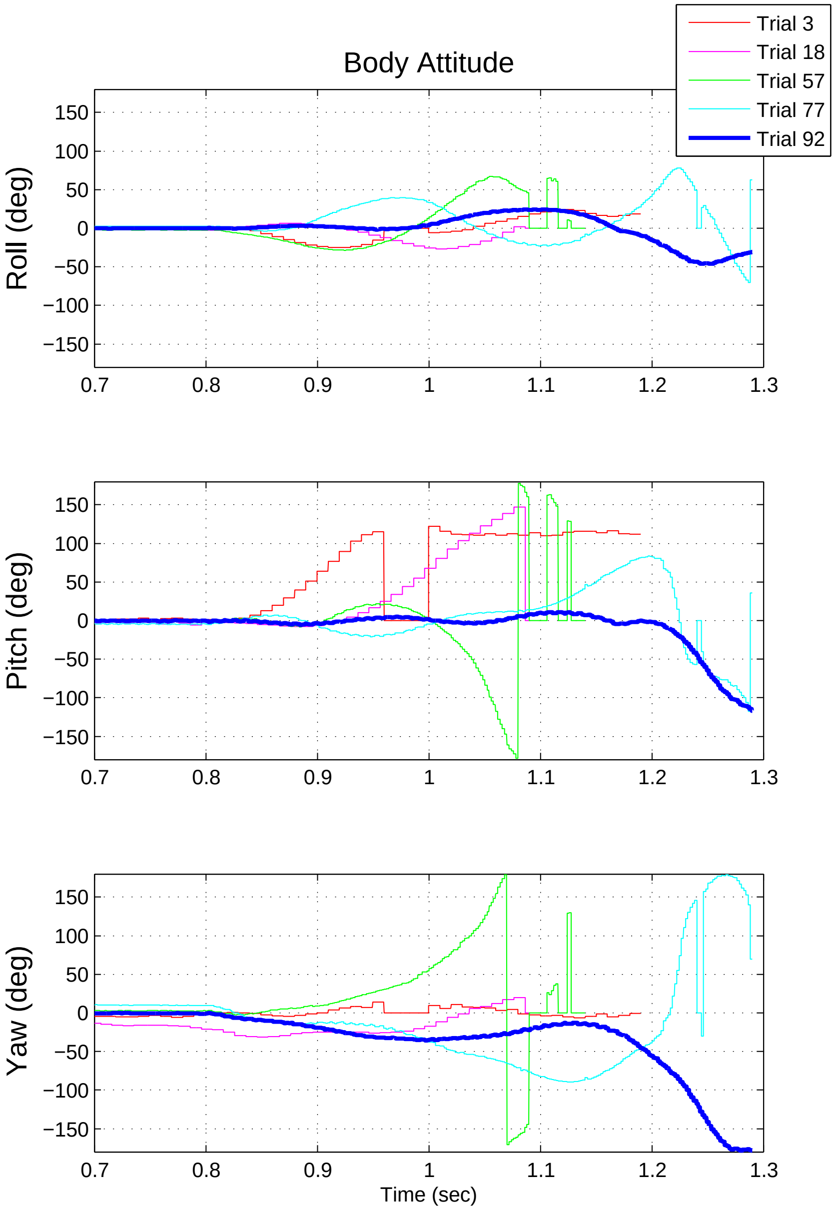

Figure 7.6: Roll, pitch and yaw angles for the same flight trajectories displayed in Fig. 7.4. Earlier trials clearly exhibit large oscillations or instabilities, resulting in crashes. The final trial (92, dark blue) maintains small pitch and roll angles until it reaches the end of the power tether.

Chapter 8

Conclusions and Future Work

At the beginning of the work presented in this thesis, the state-of-the-art for insect-sized flapping-wing micro air vehicles was limited to a robot that could lift off while attached to two external guidewires for stability. The mechanism for generating body torques for stabilization and maneuvering did not yet exist, nor did the devices to measure and characterize those torques. Control laws to stabilize a vehicle that did have these capabilities existed only in theory and not in practice.

This thesis has contributed a robot design capable of both open and closed-loop liftoff with external power and sensing. The robot is capable of directly controlling roll, pitch and yaw torques; and the instrumentation with sufficient resolution and bandwidth to measure these torques has been developed. We have also demonstrated controlled flight without the addition of stabilizing mechanisms such as sails. These are the first such results for an FWMAV that is truly insect-scale.

Despite these accomplishments, numerous issues must be addressed before the RoboBee can be functionally useful outside of the lab. The four primary issues are outlined below.

8.1 Other methods for torque control

The improved fabrication processes from [90] and [80] allow a much more rapid design cycle for testing different concept vehicles. Previously our ability to test multiple different designs was severely limited by the skill-intensive fabrication process. This thesis focuses exclusively on the use of a distributed power-and-control actuation scheme to generate body torques, but numerous other approaches are possible. The use of sails for passive stabilization and decoupled direct drives for each wing [64] are already being investigated. Other possibilities include, but are not limited to, the use of traditional thrust vectoring with control surfaces, actuated stroke plane deviation, the use of active materials to modulate flexure stiffness, and a moveable center of mass. All of these strategies could be investigated by researchers in the future.

8.2 Vehicle Optimization

The RoboBee prototypes presented in the previous chapters are by no means optimized for weight, performance or energy efficiency. There is a huge design space to potentially improve various performance metrics, such as the stiffness-to-weight ratio of the airframe, the aerodynamic efficiency of the wings, and a mass/torque tradeoff for the control actuators (large control actuators will generally lead to larger body torques - increasing control authority but decreasing payload or useful flight time). This is a system-level design optimization that must take into account related areas such as sensors, electronics, and control algorithms.

For example, it may be that using a split-actuator drive [64] (two separate power actuators that independently drive the wings directly, with no control actuators) is mechanically more efficient and lighter than the power-and-control actuator design presented here. However, the power electronics circuitry required to drive two high-frequency power actuators, instead of one high-frequency power actuator and two lower-frequency control actuators, may be more complex and heavier - actually increasing the overall weight penalty on the vehicle. A consistent and systematic way to evaluate vehicle performance, including a well-defined "cost of steering" (analogous to "cost of transport") must be used to compare different designs and make a decision for the ultimate implementation of the RoboBee.

8.3 On-board Electronics

All of the experiments presented in this thesis used vehicles that were tethered for power and control and utilized off-board sensors such as the Vicon motion capture system. Clearly a tethered vehicle will not be useful in the field, so on-board electronics including sensors [37] and power circuitry [54] must be incorporated into the design. This will require collaboration between the power electronics and mechanical design teams to develop optimal drive configuration depending on the number, size, and usage profile of multiple piezoelectric actuators; and between the sensor design and control teams to determine which sensors will be necessary for stability, navigation, and higher-level tasks such as object recognition.

8.4 Fabrication

Despite the improved fabrication process developed in [90], reliable, repeatable production of identical RoboBee prototypes is still a significant challenge. While the methods from [90] allow mass-production of identical two-dimensional parts, these parts are still hand-assembled into three-dimensional robots, introducing significant potential for error. It was obvious over many trials of different robots during control experiments that fabrication asymmetries could lead to large biases in roll, pitch and yaw torques that could make an individual vehicle difficult or impossible to control. As a solution to this problem, in the long run all hand assembly must be eliminated and the mass-production process from [80] must be adopted. This will allow reliable mass production of identical, symmetric robots for control experiments.

8.5 Funding Sources

The work in this thesis was supported by the following funding sources:

- the Office of Naval Research (under award number N00014-08-1-0919)
- the Army Research Laboratory (under award number W911NF-08-2-0004)
- the National Science Foundation (under award number CMMI-07466 38)
- the Wyss Institute for Biologically Inspired Engineering at Harvard University
- a National Defense Science and Engineering Graduate Fellowship

Any opinions, findings and conclusions or recommendations expressed in this material are those of the authors and do not necessarily reflect those of the National Science Foundation.

Bibliography

[1] Reflexite. www.reflexite.com.

[2] Xcitex products and solutions. http://xcitex.com/html/products.php.

[3] Piezo systems, 2010. www.piezo.com.

[4] G. Abraham, R. Duffait, P. Wurmsdobler, A. Matzner, and W. Brenner. Principles of torque measurement for rotating microactuators. In *Sensors, 2002. Proceedings of IEEE*, volume 2, pages 1757 – 1761, 2002.

[5] U.S. Defense Advanced Research Project Agency. Nano air vehicle program, solicitation number: Baa06-06. www.fbo.gov.

[6] K. J. Åström, P. Hagander, and J. Sternby. Zeros of sampled systems. *Automatica*, 20(1):31–38, 1984.

[7] S. Avadhanula. *Design, Fabrication and Control of the Micromechanical Flying Insect*. PhD thesis, University of California, Berkeley, 2006.

[8] S. Avadhanula and R. S. Fearing. Flexure design rules for carbon fiber microrobotic mechanisms. In *In Proc. IEEE Int. Conf. on Robotics and Automation*, pages 1579–1584, 2005.

[9] S. Avadhanula, R. J. Wood, D. Campolo, and R. S. Fearing. Dynamically tuned design of the MFI thorax. In *In Proc. IEEE Int. Conf. on Robotics and Automation*, volume 1, pages 52–59, 2002.

[10] S. S. Baek, K. Y. Ma, and R. S. Fearing. Efficient resonant drive of flapping-wing robots. In *In Proc. IEEE/RSJ Int. Conf. on Intelligent Robots and Systems*, pages 2854–2860. IEEE, 2009.

[11] C.N. Balint and M.H. Dickinson. The correlation between wing kinematics and steering muscle activity in the blowfly Calliphora vicina. *Journal of Experimental Biology*, 204(24):4213, 2001.

[12] C.N. Balint and M.H. Dickinson. Neuromuscular control of aerodynamic forces and moments in the blowfly, Calliphora vicina. *Journal of Experimental Biology*, 207(22):3813, 2004.

[13] S.K. Banala and S.K. Agrawal. Design and optimization of a mechanism for out-of-plane insect winglike motion with twist. *Journal of Mechanical Design*, 127:841, 2005.

[14] A. J. Bergou, S. Xu, and Z. J. Wang. Passive wing pitch reversal in insect flight. *J. Fluid Mech.*, 591:321–337, 2007.

[15] G.J. Berman and Z.J. Wang. Energy-minimizing kinematics in hovering insect flight. *Journal of Fluid Mechanics*, 582:153–168, 2007.

[16] A.P.F. Bernhard and I. Chopra. Hover test of mach-scale active twist rotor using piezo-bending-torsion actuators. *Journal of aircraft*, 39(4):678–688, 2002.

[17] F. Beyeler, S. Muntwyler, Z. Nagy, M. Moser, and B. J. Nelson. A multi-axis mems force-torque sensor for measuring the load on a microrobot actuated by magnetic fields. In *Intelligent Robots and Systems. IROS IEEE/RSJ Int. Conf. on*, pages 3803 –3808, 2007.

[18] F. Beyeler, S. Muntwyler, and B. J. Nelson. A six-axis mems force-torque sensor with micro-newton and nano-newtonmeter resolution. *Microelectromechanical Systems, Journal of*, 18(2):433–441, April 2009.

[19] J. Blondeau and M. Heisenberg. The three-dimensional optomotor torque system ofdrosophila melanogaster. *Journal of Comparative Physiology A: Neuroethology, Sensory, Neural, and Behavioral Physiology*, 145(3):321–329, 1982.

[20] J.Y. Bouget. Camera Calibration Toolbox for Matlab, 2008. www.vision.caltech.edu/bouguetj/calib_doc/.

[21] R.A. Brooks and A.M. Flynn. Fast, cheap and out of control. Technical report, DTIC Document, 1989.

[22] D. Campolo, R. Sahai, and R. S. Fearing. Development of piezoelectric bending actuators with embedded piezoelectric sensors for micromechanical flapping mechanisms. In *In Proc. IEEE Int. Conf. on Robotics and Automation*, volume 3, pages 3339–3346, 2003.

[23] P.C. Chen and I. Chopra. Hover testing of smart rotor with induced-strain actuation of blade twist. *AIAA journal*, 35(1):6–16, 1997.

[24] B. Cheng, X. Deng, and T.L. Hedrick. The mechanics and control of pitching manoeuvres in a freely flying hawkmoth (manduca sexta). *The Journal of Experimental Biology*, 214(24):4092–4106, 2011.

[25] Combes, S. A. and Hedrick, T. and Daniel, T. Flight control beyond the wings: abdominal flexion and pitch control in maneuvering hawkmoths. *Journal of Experimental Biology*, 2010. in prep.

[26] G. De Croon, KME De Clercq, R. Ruijsink, B. Remes, and C. De Wagter. Design, aerodynamics, and vision-based control of the delfly. *International Journal of Micro Air Vehicles*, 1(2):71–97, 2009.

[27] X. Deng, L. Schenato, and S. Sastry. Hovering flight control of a micromechanical flying insect. In *Decision and Control*, volume 1, pages 235–240, 2001.

[28] X. Deng, L. Schenato, and S. Sastry. Flapping flight for biomimetic robotic insects: Part II-flight control design. *IEEE Trans. on Robotics*, 22(4):789–803, 2006.

[29] X. Deng, L. Schenato, W.C. Wu, and S. Sastry. Flapping flight for biomimetic robotic insects: Part I-system modeling. *IEEE Trans. on Robotics*, 22(4):776–788, 2006.

[30] M. Dickinson and M. Tu. The function of dipteran flight muscle. *Comp. Biochem. Physiol.*, 116A(3):223–238, 1997.

[31] M. H. Dickinson, F. Lehmann, and S. P. Sane. Wing rotation and the aerodynamic basis of insect flight. *Science*, 284(5422):1954–1960, 1999.

[32] A. Dogan, Q. Xu, K. Onitsuka, S. Yoshikawa, K. Uchino, and R.E. Newnham. High displacement ceramic metal composite actuators (moonies). *Ferroelectrics*, 156(1):1–6, 1994.

[33] D. Doman, M. Oppenheimer, and D. Sigthorsson. Dynamics and control of a biomimetic vehicle using biased wingbeat forcing functions: Part ii-controller. In *Proceedings of the 48th AIAA Aerospace Sciences Meeting*, 2010.

[34] H. Dong, Z. Liang, and M. Harff. Optimal Settings of Aerodynamic Performance Parameters in Hovering Flight. *International Journal of Micro Air Vehicles*, 1(3):173–181, 2009.

[35] R. Dudley. *The biomechanics of insect flight: form, function, evolution*. Princeton University Press, 2000.

[36] R. Dudley. Mechanisms and Implications of Animal Flight Maneuverability 1. *Integrative and Comparative Biology*, 42(1):135–140, 2002.

[37] P.-E. Duhamel, J. Porter, B. Finio, G. Barrows, D. Brooks, G.-Y. Wei, and R. Wood. Hardware in the loop for optical flow sensing in a robotic bee. In *In Proc. IEEE/RSJ Int. Conf. on Intelligent Robots and Systems*, pages 1099–1106, 2011.

[38] C. P. Ellington. The aerodynamics of hovering insect flight. III. kinematics. *Philos. Trans. R. Soc. London Ser. B*, 305(1122):41–78, 1984.

[39] C. P. Ellington. The aerodynamics of hovering insect flight. IV. aeorodynamic mechanisms. *Philos. Trans. R. Soc. London Ser. B*, 305(1122):79–113, 1984.

[40] R. Fearing, K.H. Chiang, M. H. Dickinson, D.L. Pick, M. Sitti, and J. Yan. Wing transmission for a micromechanical flying insect. In *In Proc. IEEE Int. Conf. on Robotics and Automation*, volume 2, pages 1509–1516, 2000.

[41] Festo. SmartBird - bird flight deciphered. http://www.festo.com/cms/en_corp/11369.htm.

[42] B. Finio, C. Oland, and R. J. Eum, B. Wood. Asymmetric flapping for a robotic fly using a hybrid power-control actuator. In *In Proc. IEEE/RSJ Int. Conf. on Intelligent Robots and Systems*, 2009.

[43] B. Finio, J. Shang, and R. J. Wood. Body Torque Modulation for a Microrobotic Fly. In *In Proc. IEEE Int. Conf. on Robotics and Automation*, pages 3449–3456, 2009.

[44] B.M. Finio, K.C. Galloway, and R.J. Wood. An ultra-high precision, high bandwidth torque sensor for microrobotics applications. In *Intelligent Robots and Systems (IROS), 2011 IEEE/RSJ International Conference on*, pages 31–38. IEEE, 2011.

[45] F. Franek and A. Maciszewski. Torsionselement und ver- wendung eines solchen bei einer einrichtung zur messung von reibungskraften. Osterreichisches Patent AT 393 167 B, 1991.

[46] S. N. Fry and M. H. Dickinson. The aerodynamics of free-flight maneuvers in *Drosophila*. *Science*, 300(5618):495–498, 2003.

[47] V. Gass, B. H. Van der Schoot, S. Jeanneret, and N. F. de Rooij. Micro-torque sensor based on differential force measurement. In *Proc. IEEE Int. Conf. on Micro Electro Mechanical Systems*, pages 241 –244, 1994.

[48] G. Gremillion and J. Humbert. System identification of a quadrotor micro air vehicle. In *AIAA Conf. on Atmospheric Flight Mechanics*, 2010.

[49] T.L. Hedrick, B. Cheng, and X. Deng. Wingbeat time and the scaling of passive rotational damping in flapping flight. *Science*, 324(5924):252, 2009.

[50] A.M. Hoover and R.S. Fearing. Analysis of off-axis performance of compliant mechanisms with applications to mobile millirobot design. In *IEEE/RSJ International Conference on Intelligent Robots and Systems*, pages 2770–2776, 2009.

[51] iRobot Corporation. irobot 510 packbot, 2012. http://www.irobot.com/en/us/robots/defense/packbot.aspx.

[52] R.M. Jones. *Mechanics of composite materials.* CRC, 1999.

[53] M. Karpelson, G. Y. Wei, and R. J. Wood. A review of actuation and power electronics options for flapping-wing robotic insects. In *In Proc. IEEE Int. Conf. on Robotics and Automation*, pages 779–786, 2008.

[54] M. Karpelson, G. Y. Wei, and R. J. Wood. Milligram-Scale High-Voltage Power Electronics for Piezoelectric Microrobots. In *In Proc. IEEE Int. Conf. on Robotics and Automation*, 2009.

[55] Karpelson, M. and Whitney, J. P. and Wei, G. Y. and Wood, R. J. Energetics of Flapping-Wing Robotic Insects: Towards Autonomous Hovering Flight. In *In Proc. IEEE/RSJ Int. Conf. on Intelligent Robots and Systems*, 2010.

[56] Mathew Keennon, Karl Klingebiel, Henry Won, and Alexander Andriukov. Development of the Nano Hummingbird: A Tailless Flapping Wing Micro Air Vehicle. In *AIAA Aerospace Sciences Meeting*, 2012.

[57] Z. A. Khan and S. K. Agrawal. Design and optimization of a biologically inspired flapping mechanism for flapping wing micro air vehicles. In *In Proc. IEEE Int. Conf. on Robotics and Automation*, pages 373–378. IEEE, 2007.

[58] J. P. Khatait, S. Mukherjee, and B. Seth. Compliant design for flapping mechanism: A minimum torque approach. *Mechanism and Machine Theory*, 41(1):3–16, 2006.

[59] P. Kunze. Untersuchung des bewegungssehens fixiert fliegender bienen. *Journal of Comparative Physiology A: Neuroethology, Sensory, Neural, and Behavioral Physiology*, 44(6):656–684, 1961.

[60] U.S. Air Force Research Laboratory. M.A.V.: Micro Air Vehicles. http://www.youtube.com/watch?v=_5YkQ9w3PJ4.

[61] C. Lee, T. Itoh, and T. Suga. Self-excited piezoelectric PZT microcantilevers for dynamic SFM–with inherent sensing and actuating capabilities. *Sensors and Actuators A: Physical*, 72(2):179–188, 1999.

[62] S. Li and S. Chen. Analytical analysis of a circular PZT actuator for valveless micropumps. *Sensors and Actuators A*, 104(2):151–161, 2003.

[63] P. Luginbuhl, G. Racine, P. Lerch, B. Romanowicz, KG Brooks, NF De Rooij, P. Renaud, and N. Setter. Piezoelectric cantilever beams actuated by PZT sol-gel thin film. *Sensors and Actuators A: Physical*, 54(1-3):530–535, 1996.

[64] K. Ma, S. Felton, and R.J. Wood. Design fabrication and modeling of the split actuator microrobotic bee. In *IEEE/RSJ International Conference on Intelligent Robots and Systems*, 2012.

[65] R. Madangopal, Z. A. Khan, and S. K. Agrawal. Energetics-based design of small flapping-wing micro air vehicles. *IEEE/ASME Trans. on Mechatronics*, 11(4):433–438, 2006.

[66] R. Madangopal, G. Student, Z. A. Khan, and S. K. Agrawal. Biologically Inspired Design Of Small Flapping Wing Air Vehicles Using Four-Bar Mechanisms And Quasi-steady Aerodynamics. *Journal of Mechanical Design*, 127:809, 2005.

[67] L. Marks. *Marks' Standard Handbook for Mechanical Engineers.* McGraw Hill, 11 edition, 2007.

[68] D. Mathieson, B. J. Robertson, U. Beerschwinger, S. J. Yang, R. L. Reuben, A. J. Addlesee, J. Spencer, and R. A. Lawes. Micro torque measurements for a prototype turbine. *Journal of Micromechanics and Microengineering*, 4(3):129, 1994.

[69] T. Maxworthy. The fluid dynamics of insect flight. *Annual Review of Fluid Mechanics*, 13(1):329–350, 1981.

[70] G.D. McCann and GF MacGinitie. Optomotor response studies of insect vision. *Proceedings of the Royal Society of London. Series B. Biological Sciences*, 163(992):369–401, 1965.

[71] N. O. Pérez-Arancibia and Ma, K. and Galloway, K. and Greenberg, J. and R. J. Wood. First controlled vertical flight of a biologically inspired microrobot. *Bioinspiration and Biomimemts*, 6, 2011.

[72] N. O. Pérez-Arancibia, J. P. Whitney and R. J. Wood. Lift force control of a flapping-wing microrobot. In *American Controls Conf.*, pages 4761–4768, 2011.

[73] M. Oppenheimer, D. Doman, and D. Sigthorsson. Dynamics and control of a biomimetic vehicle using biased wingbeat forcing functions: Part i-aerodynamic model. In *Proceedings of the 48th AIAA Aerospace Sciences Meeting*, 2010.

[74] H. Ota, T. Ohara, Y. Karata, S. Nakasima, and M. Takeda. Novel micro torque measurement method for microdevices. *Journal of Micromechanics and Microengineering*, 11(5):595, 2001.

[75] N. Pérez-Arancibia, P. Chirarattananon, B. Finio, and R. Wood. Pitch-angle feedback control of a biologically inspired flapping-wing microrobot. In *IEEE Int. Conf. on Robotics and Biomimetics*. IEEE, 2011.

[76] D. Robert. Visual steering under closed-loop conditions by flying locusts: flexibility of optomotor response and mechanisms of correctional steering. *Journal of Comparative Physiology A: Neuroethology, Sensory, Neural, and Behavioral Physiology*, 164(1):15–24, 1988.

[77] L. Schenato, X. Deng, and S. Sastry. Flight control system for a micromechanical flying insect: Architecture and implementation. In *In Proc. IEEE Int. Conf. on Robotics and Automation*, volume 2, pages 1641–1646, 2001.

[78] M. Sitti. PZT actuated four-bar mechanism with two flexible links for micromechanical flying insect thorax. In *In Proc. IEEE Int. Conf. on Robotics and Automation*, volume 4, pages 3893–3900, 2001.

[79] M. Sitti, D. Campolo, J. Yan, and R. S. Fearing. Development of PZT and PZN-PT based unimorph actuators for micromechanical flapping mechanisms. In *In Proc. IEEE Int. Conf. on Robotics and Automation*, volume 4, pages 3839–3846. IEEE, 2005.

[80] Sreetharan, P. and Whitney, J.P. and Strauss, M. and Wood, R.J. Monolithic fabrication of millimeter-scale machines. *J. Micromech. Microeng.*, 2012.

[81] E. Steltz and R. S. Fearing. Dynamometer power output measurements of piezoelectric actuators. In *In Proc. IEEE/RSJ Int. Conf. on Intelligent Robots and Systems*, pages 3980–3986. IEEE, 2007.

[82] E. Steltz and R. S. Fearing. Dynamometer power output measurements of miniature piezoelectric actuators. *IEEE/ASME Trans. on Mechatronics*, 14(1):1–10, 2009.

[83] E. Steltz, M. Seeman, S. Avadhanula, and RS Fearing. Power electronics design choice for piezoelectric microrobots. In *In Proc. IEEE/RSJ Int. Conf. on Intelligent Robots and Systems*, pages 1322–1328, 2006.

[84] T. Tantanawat and S. Kota. Design of compliant mechanisms for minimizing input power in dynamic applications. *Journal of Mechanical Design*, 129:1064–1075, 2007.

[85] G. K. Taylor. Mechanics and aerodynamics of insect flight control. *Biol. Rev. Camb. Philos. Soc.*, 76(04):449–471, 2001.

[86] B. P. Trease, Y. M. Moon, and S. Kota. Design of large-displacement compliant joints. *Journal of Mechanical Design*, 127:788, 2005.

[87] HTG Van Lintel, FCM Van de Pol, and S. Bouwstra. A piezoelectric micropump based on micromachining of silicon. *Sensors and Actuators*, 15(2):153–167, 1988.

[88] A. Vujanic, N. Adamovic, M. Jakovljevic, W. Brenner, G. Popovic, and H. Detter. Silicon microstructure for precise measurements of mechanical moments. *Microelectronics Journal*, 31(11-12):975 980, 2000.

[89] J. P. Whitney and R. J. Wood. Aeromechanics of passive rotation in flapping flight. *Journal of Fluid Mechanics*, 1(1):1–24, 2010.

[90] JP Whitney, PS Sreetharan, KY Ma, and RJ Wood. Pop-up book MEMS. *Journal of Micromechanics and Microengineering*, 21(11):115021–115027, 2011.

[91] R. J. Wood. Design, fabrication, and analysis, of a 3DOF, 3cm flapping-wing MAV. In *In Proc. IEEE/RSJ Int. Conf. on Intelligent Robots and Systems*, pages 1576–1581, 2007.

[92] R. J. Wood. Liftoff of a 60mg flapping-wing MAV. In *In Proc. IEEE/RSJ Int. Conf. on Intelligent Robots and Systems*, pages 1889–1894, 2007.

[93] R. J. Wood. The first takeoff of a biologically inspired at-scale robotic insect. In *IEEE Trans. on Robotics*, volume 24, pages 341–347, 2008.

[94] R. J. Wood, S. Avadhanula, R. Sahai, E. Steltz, and R. S. Fearing. Microrobot Design Using Fiber Reinforced Composites. *J. Mech. Design*, 130:52304–52315, 2008.

[95] R. J. Wood, K. J. Cho, and K. Hoffman. A novel multi-axis force sensor for microrobotics applications. *Smart Materials and Structures*, 18:125002, 2009.

[96] R. J. Wood, E. Steltz, and R. S. Fearing. Nonlinear performance limits for high energy density piezoelectric bending actuators. In *In Proc. IEEE Int. Conf. on Robotics and Automation*, pages 3633–3640. IEEE, 2005.

[97] R. J. Wood, E. Steltz, and R. S. Fearing. Optimal energy density piezoelectric bending actuators. *Sensors and Actuators A: Physical*, A 119:476–488, 2005.

[98] W.C. Wu, R. J. Wood, and R. S. Fearing. Halteres for the micromechanical flying insect. In *In Proc. IEEE Int. Conf. on Robotics and Automation*, volume 1, pages 60–65, 2002.

[99] M.-L. Zhu, S.-W.R. Lee, H.-L. Li, T.-Y. Zhang, and P. Tong. Modeling of torsional vibration induced by extension-twisting coupling of anisotropic composite laminates with piezoelectric actuators. *Smart Materials and Structures*, 11:55–62, 2002.

[100] C. Zwyssig, S. D. Round, and J. W. Kolar. Analytical and experimental investigation of a low torque, ultra-high speed drive system. In *Industry Applications Conf., 2006. 41st IAS Annual Meeting. Conf. Record of the 2006 IEEE*, volume 3, pages 1507 –1513, oct. 2006.

Appendix A

RoboBee Fabrication

This appendix is intended primarily as an internal reference for future researchers in the Harvard Microrobotics Lab or another lab with similar fabrication capabilities. It details the fabrication process used to create the RoboBees used for controlled flight testing in Chapter 7. More details about the underlying fabrication process are presented in [90] and [80].

A.1 Assembly Steps

This section presents a step-by-step procedure for building a complete RoboBee. See the following sections for more detailed descriptions of each part and figures detailing assembly of individual parts. Refer to Fig. A.1 for materials necessary for each part and laser cut settings.

1. Cut out each of the six layers for the transmission (Fig. A.1). Be sure to include alignment crosses in the top carbon fiber layer.

2. Cure the transmission in the pin-aligned weight press using the EZ1 program and six weights.
3. Re-align the transmission in the laser and do the release cut.
4. Cut out each of the three layers for the airframe. Include alignment crosses on the carbon fiber layer.
5. Cure the airframe in the pin-aligned weight press using the EZ1 program and six weights.
6. Re-align the airframe in the laser and do the release cut.
7. Cut out the FR4, aluminum oxide, and gelpak for the actuators. Be sure to include alignment crosses on the top FR4 layer.
8. Score and cleave the PZT pieces. Be sure to keep track of polarity (have someone teach you this process if you are not familiar with it, directions are not included in this appendix).
9. Use the ultrasonic cleaner to clean the PZT pieces, again, keeping track of polarity of the separate top and bottom pieces.
10. Remove the M55J from the freezer and wait for it to come to room temperature before removing from the ziploc bag and cutting.
11. Cut the M55J layer for the actuators.
12. Layer the actuator materials, dropping the PZT and aluminum oxide pieces into the respective top and bottom FR4 layers.

13. Cure the actuators in the right-hand weight press using the EZ2 program and three weights.
14. Re-align the actuators in the laser and do the release cut. Refocusing due to the thickness of the part is recommended (30 passes each focused to the top FR4, exposed carbon fiber, and gelpak substrate respectively).
15. Make wings (not covered in this appendix).
16. Attach the actuators to the airframe.
17. Assemble the airframe.
18. Fold the transmission.
19. Attach the transmission to the actuators.
20. Wire the three positive (bias) plates of the actuators together, and connect the three ground plates, using conductive epoxy.
21. Connect five external wires (ground, bias, signal 1, signal 2, signal 3).
22. Attach the wings to the wing hinges separately.
23. Mount the wing hinges to the transmission.
24. Fly!

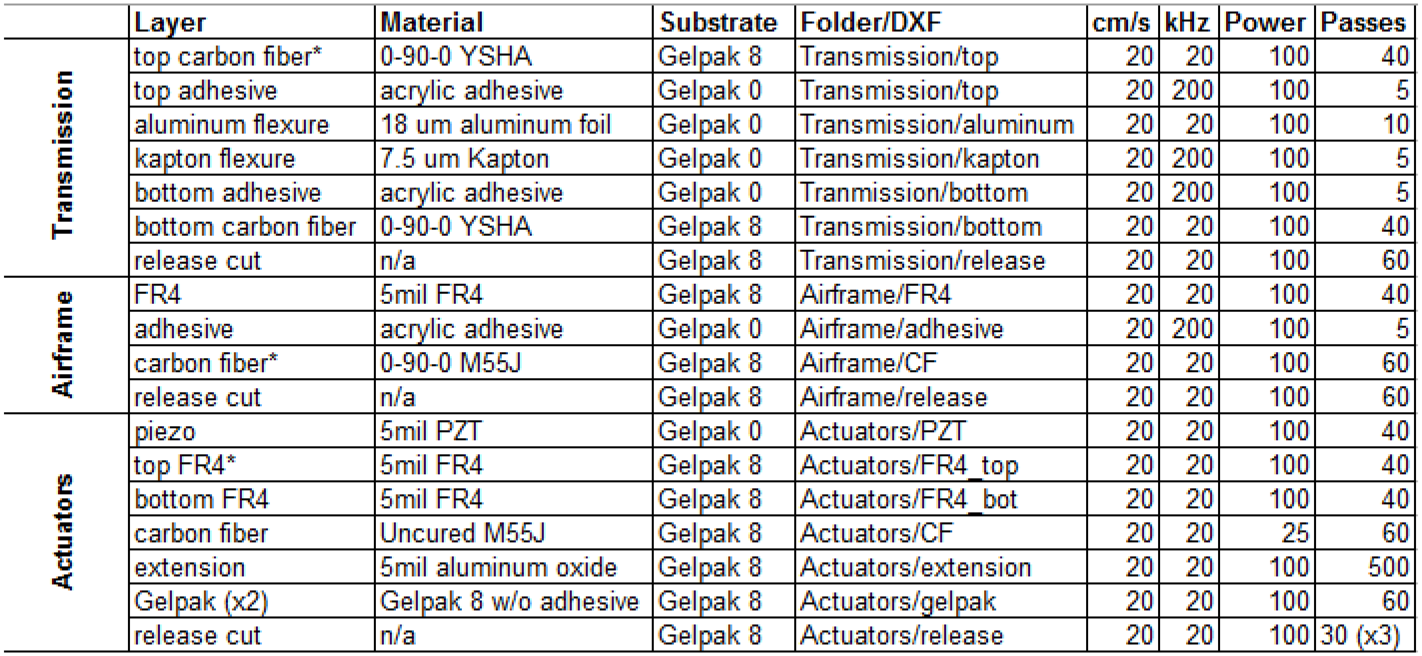

	Layer	Material	Substrate	Folder/DXF	cm/s	kHz	Power	Passes
Transmission	top carbon fiber*	0-90-0 YSHA	Gelpak 8	Transmission/top	20	20	100	40
	top adhesive	acrylic adhesive	Gelpak 0	Transmission/top	20	200	100	5
	aluminum flexure	18 um aluminum foil	Gelpak 0	Transmission/aluminum	20	20	100	10
	kapton flexure	7.5 um Kapton	Gelpak 0	Transmission/kapton	20	200	100	5
	bottom adhesive	acrylic adhesive	Gelpak 0	Tranmission/bottom	20	200	100	5
	bottom carbon fiber	0-90-0 YSHA	Gelpak 8	Transmission/bottom	20	20	100	40
	release cut	n/a	Gelpak 8	Transmission/release	20	20	100	60
Airframe	FR4	5mil FR4	Gelpak 8	Airframe/FR4	20	20	100	40
	adhesive	acrylic adhesive	Gelpak 0	Airframe/adhesive	20	200	100	5
	carbon fiber*	0-90-0 M55J	Gelpak 8	Airframe/CF	20	20	100	60
	release cut	n/a	Gelpak 8	Airframe/release	20	20	100	60
Actuators	piezo	5mil PZT	Gelpak 0	Actuators/PZT	20	20	100	40
	top FR4*	5mil FR4	Gelpak 8	Actuators/FR4_top	20	20	100	40
	bottom FR4	5mil FR4	Gelpak 8	Actuators/FR4_bot	20	20	100	40
	carbon fiber	Uncured M55J	Gelpak 8	Actuators/CF	20	20	25	60
	extension	5mil aluminum oxide	Gelpak 8	Actuators/extension	20	20	100	500
	Gelpak (x2)	Gelpak 8 w/o adhesive	Gelpak 8	Actuators/gelpak	20	20	100	60
	release cut	n/a	Gelpak 8	Actuators/release	20	20	100	30 (x3)

Figure A.1: A list of required materials and cut settings for making the transmission, airframe and actuators. **Important**: Layers marked with a * require alignment crosses.

A.2 Transmission

The transmission consists of two carbon fiber layers (each layer is 0-90-0, approximately 100μm thick) that sandwich a hybrid Kapton-aluminum flexure layer. 7.5μm Kapton is used for dynamically active flexures and 18μm aluminum foil (Reynolds Wrap) is used for static 90° folds. Two sheets of acrylic adhesive are used, one on each side of the flexure layer, to bond to the carbon fiber. Each layer is individually laser machined and then stacked using pin alignment and cured in a heated weight press. An expanded view of the layup is shown in Fig. A.2. Note that, while the Kapton and aluminum foil sheets are separate parts of the layup, gaps in the Kapton layer allow cantilevered areas of the aluminum layer to be pressed into a single flexure layer. The transmissions are released in a single laser-cutting step after the cure. They are then manually folded into the 3D structure and CA glue is used to freeze each 90 degree fold (Fig. A.3). The wing hinges are released as separate parts and manually attached to the transmission.

A.3 Airframe

The airframe consists of a single layer of 0-90-0 carbon fiber (M55J, approximately 150μm thick) with FR4 alignment tabs that allow for “jigsaw puzzle” alignment of the base of each actuator to the airframe. The FR4 is bonded to the carbon fiber with a single acrylic adhesive layer. The layup for the airframe is shown in Fig. A.4. After curing, the airframe is laser-cut and released into four separate pieces (Fig. A.4). The actuators are attached to these pieces individually and then the entire airframe

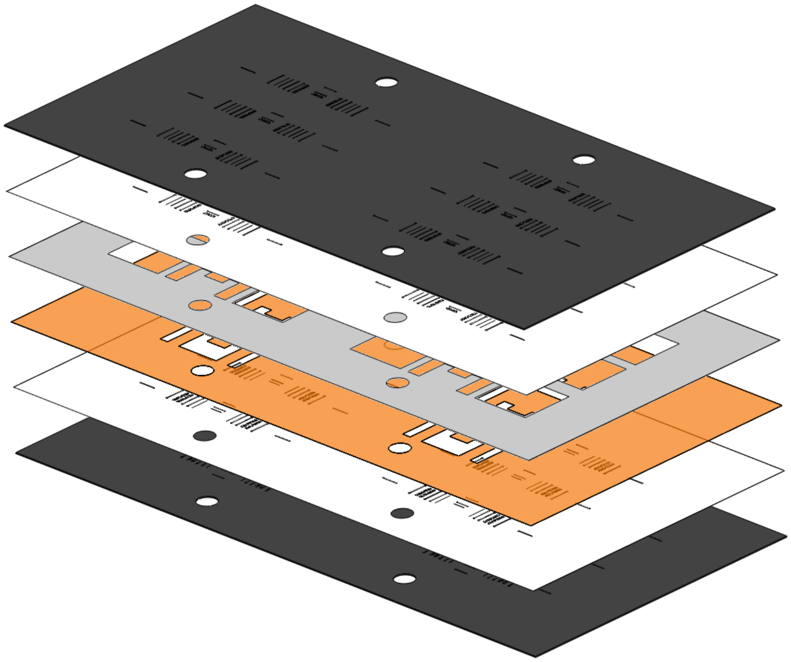

Figure A.2: Expanded view of the transmission layup, showing, from top to bottom: carbon fiber, adhesive, aluminum, kapton, adhesive, and carbon fiber layers. Standard pressure distribution and release layers are used on both sides of the layup in the press (not pictured): silicone rubber, stainless steel shim, and teflon.

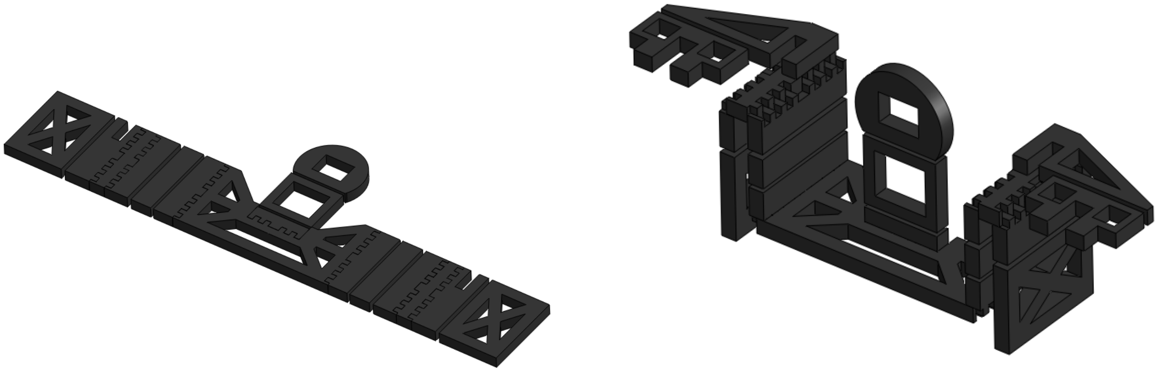

Figure A.3: A single transmission after curing and release (left) and a folded transmission (right).

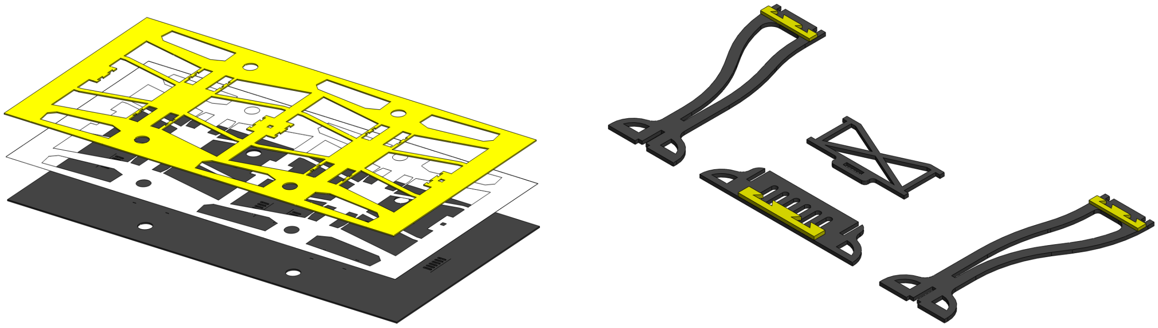

Figure A.4: Airframe layup showing single carbon fiber layer, adhesive layer, and FR4 layer. Silicone rubber, steel and teflon layers are not shown (left). The four separate pieces are shown post-release (right). Note that the images are not to the same scale - the layup (left) contains four complete airframes, the right image only shows parts for one airframe.

is assembled. This is detailed in the “Assembly” section below.

A.4 Actuators

Actuators are also made using the pin alignment process. Top and bottom FR4 and central carbon fiber (M55J) layers are pin-aligned, and individual piezoelectric (PZT) plates and aluminum oxide (Al_2O_3) extensions are manually dropped into the FR4 layers using kinematic alignment. Fig. A.5 shows PZT plates and Al_2O_3 extensions being dropped into the bottom FR4 layer. The uncured carbon fiber layer is placed on top of the bottom FR4/PZT/Al_2O_3 layer, then the top FR4 layer is added, and the final PZT and Al_2O_3 pieces are dropped in. The complete layup is shown in Fig. A.5. The layup is cured using the RS3-C resin cure cycle and the actuators are released in a single cut after curing (Fig. A.6). Note that a small carbon fiber “bridge” piece is manually attached across the gap between the tip of the PZT and the extension using CA glue, after the actuators have been released.

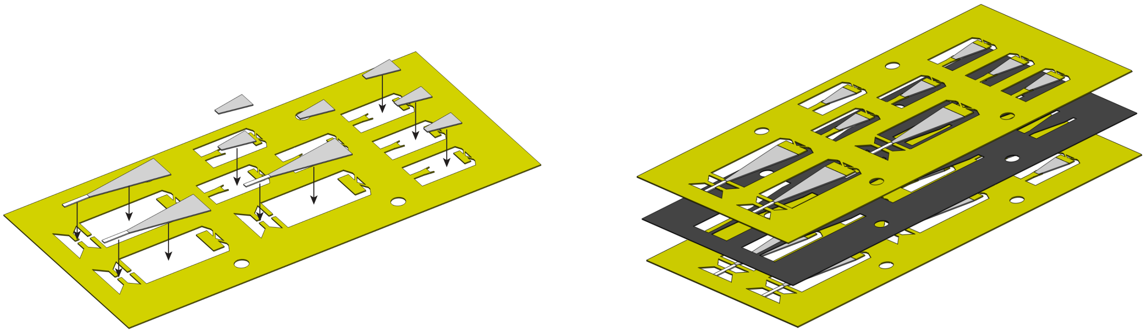

Figure A.5: (left) Diagram showing how PZT and Al_2O_3 components are dropped into the bottom FR4 layer using alignment features. In addition to the standard layup materials (silicone rubber, steel, teflon), a final layer of Gelpak 8 with no adhesive backing (not shown) is used to hold the components in-plane relative to the FR4. (right) The complete actuator layup: bottom layer with FR4 and manually-placed PZT and Al_2O_3 components, central carbon fiber layer, and top FR4/PZT/Al_2O_3 layer.

This piece is not included as part of the layup in order to avoid stress concentrations. The versions used in my control tests were wired manually and did not include any flex circuit or copper-clad FR4 connections. After release and addition of the carbon fiber bridge, the actuators are individually attached to the separate airframe pieces (Fig. A.6).

A.5 Assembly

After actuators have been mounted to the airframe pieces, the airframe is assembled by sliding the side walls into the slots of the base piece, then dropping the crossbrace into the notches at the top of the side walls (Fig. A.7). The transmission is then attached to the actuators - the tip of the power actuator slides through a slot in the last link of the slider crank, and the ground points on either side of the transmission attach to the tips of the control actuators (Fig. A.7). As a last step,

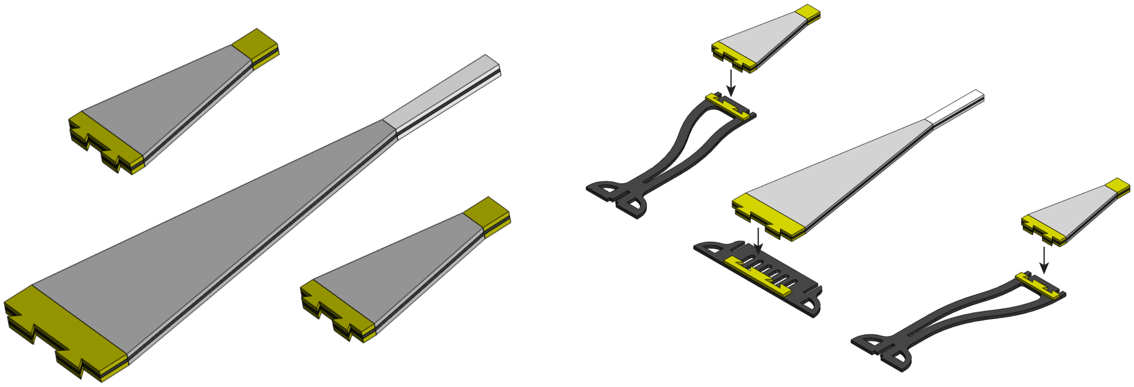

Figure A.6: (left) A set of released actuators: one large power actuator and two smaller control actuators. (right) The actuators are individually attached to the airframe pieces with CA glue, using the FR4 tabs for alignment.

the wings are attached to the transmission (the wing hinges can either be attached to the wings first or the transmission first, depending on user preference).

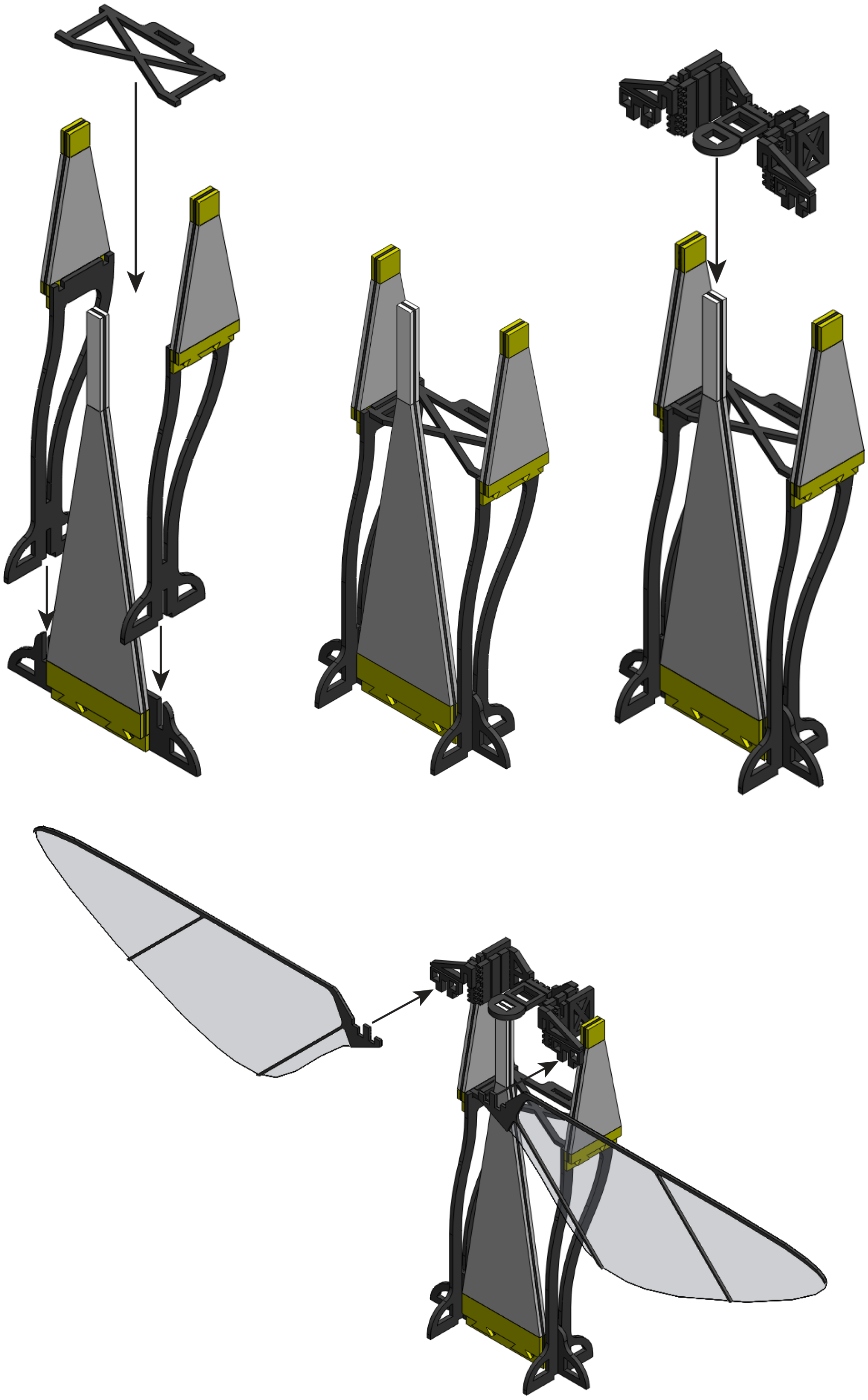

Figure A.7: Assembly process. The side walls of the airframe are inserted into slots in the base piece, then the crossbrace is attached (top left). This results in the completed actuator-airframe structure (top center). The transmission is then mounted to the actuators (top right). Finally, the wings are attached to the transmission (bottom).

Appendix B

Stroke plane deviation for a microrobotic fly

Wing motion in most flapping-wing micro air vehicles (MAVs) is restricted to a flat stroke plane in order to simplify analysis and mechanism design. An MAV actuation and transmission design capable of controlling flapping motions and deviations from the mean stroke plane using relatively simple modifications to a proven design is presented. This allows preliminary investigation into more power-efficient wing trajectories, an important concern for small MAVs. A theoretical quasi-steady model of flapping wing flight is used to predict wing motions, and these predicted trajectories are compared to empirically observed trajectories from a test device. The ratio of average lift to average aerodynamic power is used as an efficiency metric to compare stroke trajectories.

B.1 Introduction

One frequent simplifying assumption made when analyzing flapping-wing flight is that the stroke plane is flat, i.e. the torsional axis of the wing flaps back and forth in a plane, and does not deviate vertically (Fig. B.1 illustrates the wing motion and defines wing angles). There are two reasons for this assumption: (1) many biological wing trajectories do show relatively flat stroke planes, and (2) a flat stroke plane greatly simplifies mechanical construction, as a planar crank-rocker four-bar mechanism with a DC motor (or slider-crank with a linear piezoelectric actuator in the case of the HMF [97]) can be used to generate oscillatory wing motion; whereas stroke-plane deviation requires a more complicated three-dimensional mechanism or a spherical joint (such as the five-bar mechanism with auxiliary four-bar in [13]).

While the flat-stroke plane assumption seems to be a reasonable approximation and has proven successful for several MAV prototypes, inspection of biological data does reveal oval, U-shaped and figure-of-eight wing trajectories [46, 69, 38] (Fig. B.2). Recent theoretical fluid dynamics studies of flapping-wing flight have shown that wing trajectories with nonzero stroke plane deviation may be more efficient and effective in terms of the power that must be expended to keep the vehicle aloft or maneuver [34, 15]. Many current MAV designs have limited flight times due to the limited capacity and energy density of available small-scale power supplies [55], and the future of MAV flight depends heavily on improvement of energy sources such as Lithium-polymer batteries. Thus, any potential increase in efficiency is of vital importance. Since all previous HMF designs were restricted to flapping in a flat stroke plane, the investigation of potentially more efficient stroke trajectories

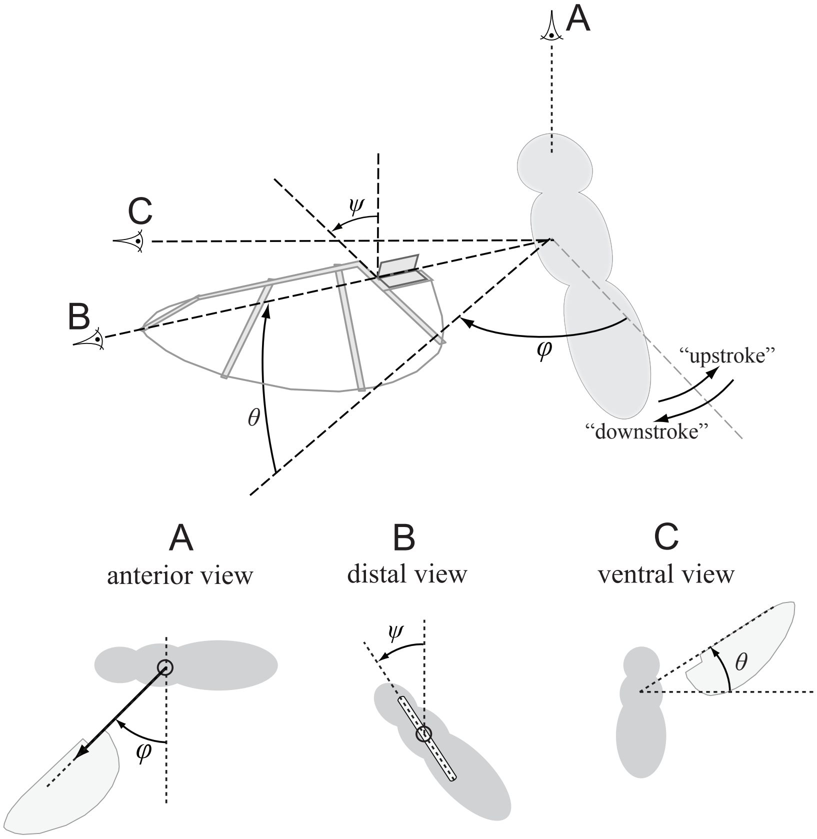

Figure B.1: Definitions of flapping-wing stroke parameters. The angle of rotation of the torsional axis of the wing measured about an axis perpendicular to the mean stroke plane is the *stroke angle* ϕ; the out-of-plane angle measured to the torsional axis of the wing is the *deviation angle* θ; and the rotation of the wing about its torsional axis is the *rotation angle* ψ. The wing flapping forward with respect to the body is referred to as the "downstroke", flapping backward with respect to the body is the "upstroke". Figure not to scale.

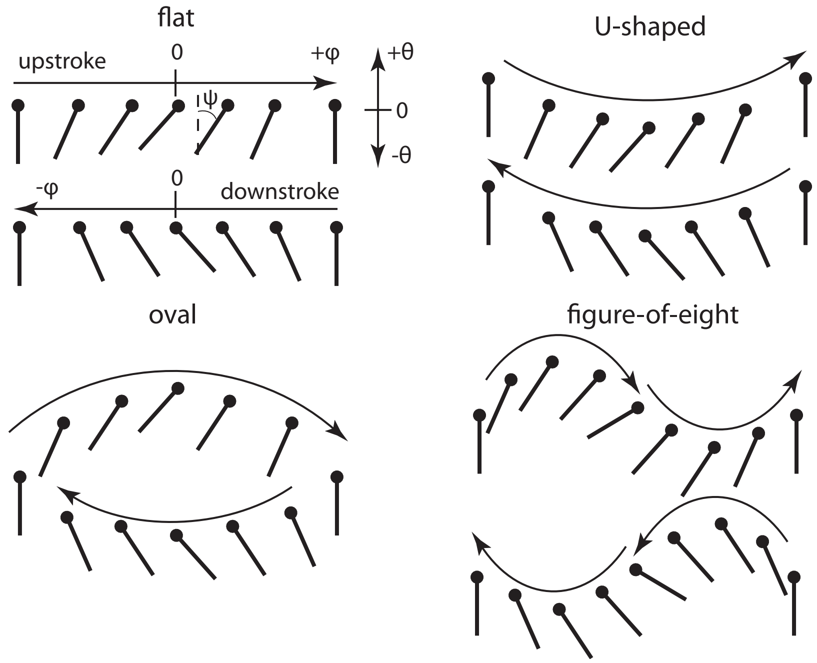

Figure B.2: An "unwrapped" distal view of nominal stroke types. Most MAVs have flat stroke planes, but many more varied trajectories are observed in nature. The filled-in circle represents the leading edge of the wing (assumed to be coincident with the torsional axis for this figure, although this need not be the case). Wing motion is parameterized by the angles ϕ, θ and ψ. For illustration purposes only, not to scale.

involving stroke plane deviation was not possible. The new design presented here enables a preliminary comparison of different trajectory types based on the merits of lift generation and aerodynamic power expenditure as calculated by a theoretical blade-element aerodynamic model. The added complexity and mass associated with such mechanisms is also considered.

B.2 Background and Previous Work

Unlike conventional aircraft which utilize control surfaces for decoupled roll, pitch and yaw control (i.e. elevators, ailerons and rudders), insects primarily use asymmetric changes in wing kinematics for attitude control [85] (it has also been shown that insects can use abdominal and leg movements to aid in maneuvering [25], but that is beyond the scope of this work). Insects possess distinct groups of power and control muscles used to generate primary flapping motion and control these asymmetric motions respectively [30, 11, 12, 35]. Previous versions of the HMF have experimented with this idea, using a single large piezoelectric actuator to flap the wings, and smaller actuators to change the kinematics of the four-bar transmission, allowing asymmetric modulation of stroke amplitude [43, 42]. Since stroke-plane deviation angles are typically about an order of magnitude smaller than stroke amplitude (i.e. about 10 degrees compared to 100 degrees peak-to-peak), this also seems like a suitable application for separation of power and control actuators. Using previously developed fabrication techniques [94], a two-input transmission system consisting of two orthogonal flexure-based four-bars for actuation of stroke angle and deviation angle is constructed. Mechanism design, kinematic and dynamic analysis, and experimental results are presented in the following sections.

B.3 Mechanism Design and Fabrication

The original HMF transmission is a symmetric four-bar that converted a single linear actuator input into rotational motion of two wings. The flexure-based transmission, made from a layered combination of rigid carbon fiber sheets and flexible polymers, is laser-micromachined in two dimensions and then assembled into a three dimensional structure (Fig. B.3). Flexures can either be fixed at 90 degrees using an adhesive, or left free to function as revolute joints. Previous modifications of this design to allow stroke amplitude modulation required additional actuator inputs but no topological changes to the transmission [43, 42], however this design does not allow for stroke-plane deviation. It is desired to add a controlled degree of freedom with a rotation axis orthogonal to the ϕ rotation axis, while keeping the structure as simple as possible. This can be accomplished by adding a second flexure-based four-bar orthogonal to the original four-bar (Fig. B.4). The two primary benefits of this design are that (a) it does not require any additional 90-degree folds, thus keeping fabrication simple and (b) if the flexures are stiff enough to off-axis loads (off-axis compliance must be considered when designing flexure-based mechanisms [50]), it gives decoupled control of stroke amplitude and deviation angle through two actuator inputs. It also only requires the addition of several linkages that are small relative to the overall structure (including airframe and actuators), so the added mass is negligible. Rotation of the wing remains passive as in the original HMF design, as opposed to previous MAV designs with direct control over both flapping and rotation [40, 78]. While there is still some debate as to the level of active or passive control of insect wing rotation, evidence exists to show that rotation is at least partially, if not wholly passive [14].

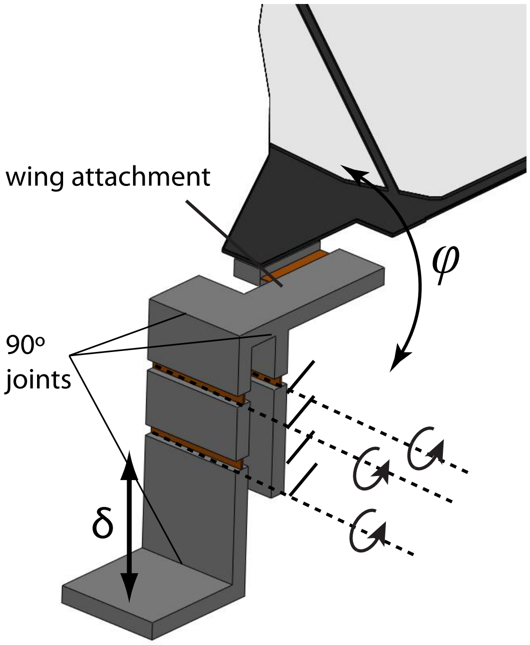

Figure B.3: Illustration of one-half of the original HMF transmission. In this drawing, δ is an actuated input and ϕ is the wing flapping as defined in Fig. B.1.

B.4 Kinematics and Dynamics

B.4.1 Kinematics

The kinematics of the four-bar mechanisms can be derived using a pseudo-rigid body model, assuming that all carbon fiber links are rigid and that flexures act as ideal revolute joints. This has been shown previously in [43], and the kinematics are reproduced here. The stroke angle ϕ can be written as a function of actuator input δ_1 and link geometry L_i (see Fig. B.5):

$$L_y = L_1 + L_2 - L_4 \tag{B.1}$$

$$C_1 = L_3^2 + (L_2 - L_4)^2 - L_1^2 + L_3^2 \tag{B.2}$$

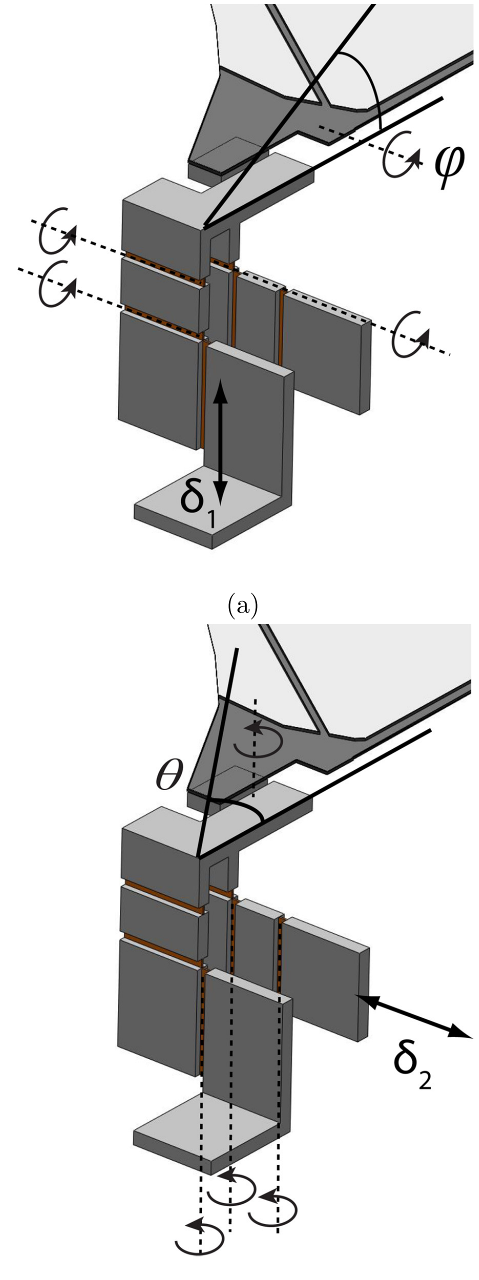

(a)

(b)

Figure B.4: Illustration of the stroke plane deviation transmission. Linear actuator inputs δ_1 and δ_2 are converted to (a) stroke angle ϕ and (b) deviation angle θ respectively. Note that this design does not require any additional 90 degree folds than the transmission in Fig. B.3.

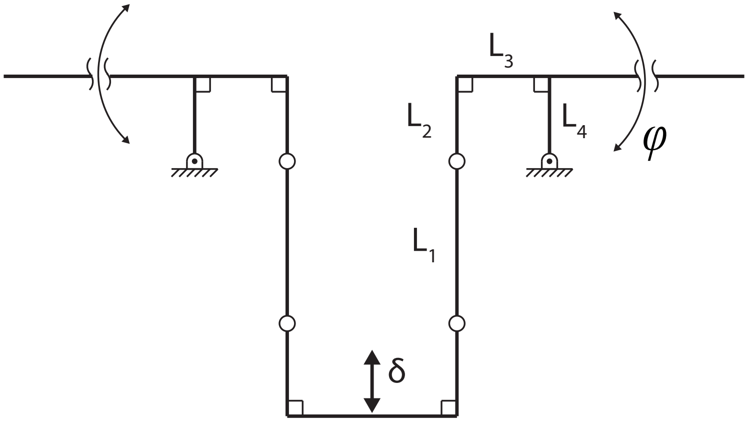

Figure B.5: A pseudo-rigid body model of the original HMF transmission.

Table B.1: Actuator drive signals for different stroke trajectories

Trajectory	$\delta_1(t)$	$\delta_2(t)$
Flat	$\frac{A}{T}\sin(\omega t)$	0
Oval	$\frac{A}{T}\sin(\omega t)$	$\frac{B}{T}\sin(\omega t + \frac{\pi}{2})$
figure-of-eight	$\frac{A}{T}\sin(\omega t)$	$\frac{B}{T}\sin(2\omega t)$

$$C_2 = 2\sqrt{L_3^2 + (L_2 - L_4)^2} \tag{B.3}$$

$$\phi = cos^{-1}\left(\frac{(L_y - \delta_1)^2 + C_1}{C_2\sqrt{L_3^2 + (L_y - \delta_1)^2}}\right) + tan^{-1}\left(\frac{L_3}{L_y - \delta_1}\right) + tan^{-1}\left(\frac{L_2 - L_4}{L_3}\right) - \frac{\pi}{2}. \tag{B.4}$$

An equivalent formulation can be used to give θ as a function of actuator input δ_2 and the geometry of the second four-bar. Although Eq. B.4 is nonlinear, geometry

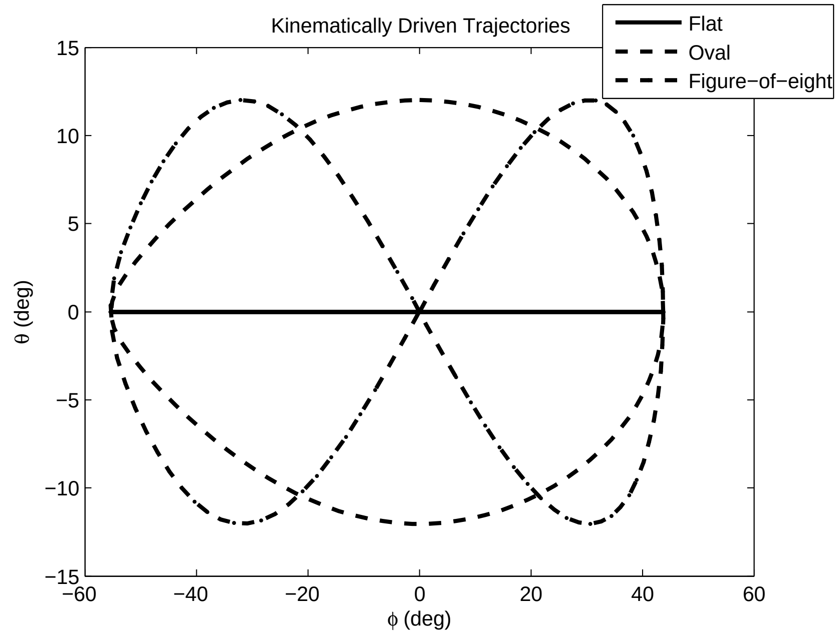

Figure B.6: Wing trajectories using the full nonlinear kinematics, with actuator inputs $\delta_1 = \pm 350\mu m$, $\delta_2 = \pm 100\mu m$, and transmission geometry $L_1 = 500\mu m$, $L_2 = 500\mu m$, $L_3 = 480\mu m$, $L_4 = 500\mu m$ for both the flapping and deviation transmissions.

can be selected to give an approximately linear response [91] such that:

$$\phi \equiv T\delta_1 \tag{B.5}$$

where $T \approx 1/L_3$. Assuming an approximately linear relationship between input displacement and output angle allows the drive signals in Table B.1 to be used to generate the baseline trajectories shown in Fig. B.2, where A and B are the desired amplitudes for stroke angle and deviation angle respectively. Actual trajectories in $\phi - \theta$ space are shown in Fig. B.6 for given sinusoidal actuator inputs using the full nonlinear kinematics. It is important to note that these trajectories are not perfectly symmetric in ϕ or θ since the transmission kinematics are nonlinear and not symmetric about $\delta_i = 0$.

B.4.2 Dynamics

A linearized, lumped parameter dynamic model of the system is shown in Fig. B.7. Each of the two actuator/transmission systems acts as a force source in parallel with a spring and damper element, which provide a linear input to a transmission that converts motion to wing rotation. Aerodynamic lift and drag forces (discussed below) act on the wing as the wing moves through a fluid (air). It is important to note that, due to the orientation of the flexure hinge that allows the wing to passively rotate, the wing will not passively rotate when only δ_2 is actuated. Actuation of δ_1 is required to generate both lift and drag forces. The model used in this work is only a subsystem of the full dynamic model (inside the dashed box in Fig. B.7), equivalent to assuming full kinematic control of δ_1 and δ_2 as control inputs. This allows focus on desired wing trajectories and resulting passive wing rotation. However, while the motions ϕ and θ are *kinematically* decoupled, it will be seen that they are not *dynamically* decoupled since actuation of δ_1 causes a force in the direction of δ_2. While beyond the scope of this work, future dynamic modeling will incorporate the spring-damper elements, with actuators modeled as force, not displacement sources, as well as incorporate feedback control of actuator motion.

The aerodynamic model is a quasi-steady blade element model, meaning that (a) lift and drag forces corresponding to the instantaneous wing velocity (derived empirically in [31]) are used and (b) aerodynamic forces and moments are calculated on thin chordwise strips of the wing, then integrated over the length of the wing to arrive

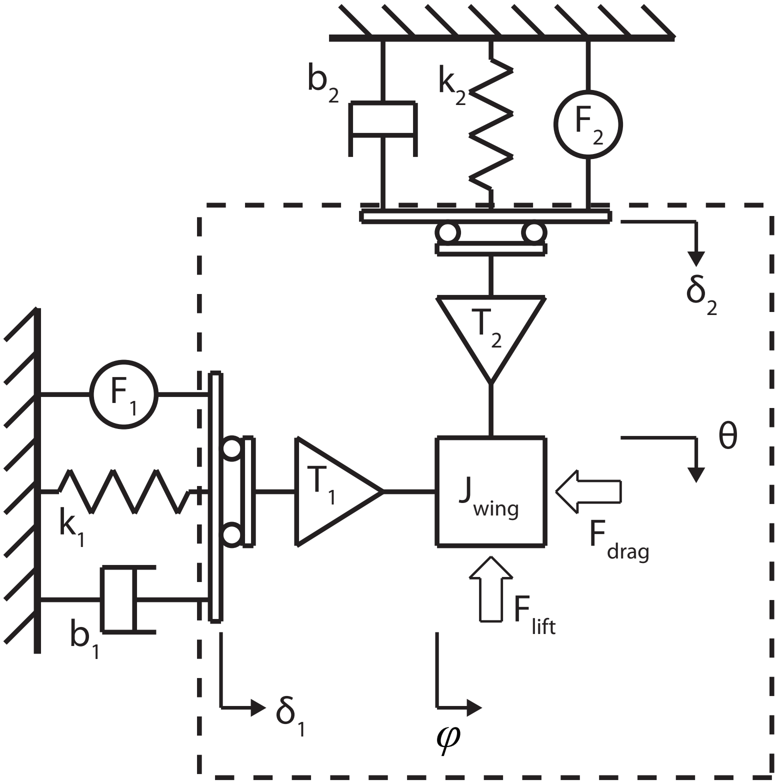

Figure B.7: A schematic of the system dynamic model. Only the subsystem within the dashed box is considered for purposes of this paper. Note that the motions δ_1 and δ_2 are (and therefore ϕ and θ) are kinematically decoupled.

at total forces and moments. Aerodynamic forces and moments are therefore functions of instantaneous wing velocity, angle of attack α (defined as the angle between the local translational velocity vector and the wing chord), and wing geometry. The wing is assumed to be a rigid flat plate attached to a torsional spring on the ψ-axis, rotations about the ϕ and θ axes are driven kinematically. A differential equation for ψ can then be written as a function of inertial, spring and aerodynamic terms and the driving (ϕ, θ) trajectory, of the form

$$\ddot{\psi} = f\left(\phi, \dot{\phi}, \theta, \dot{\theta}, \psi, \dot{\psi}, \mathbf{I}, M\right) \tag{B.6}$$

where $\mathbf{I}$ is the wing's inertia tensor and M is the term including aerodynamic moments, which are functions of both normal and tangential force coefficients, wing geometry, and proportional to the square of wing velocity and rotation rate. The normal and tangential force coefficients C_N and C_T themselves are functions of α, thus the moment terms are of the form

$$M = f\left(C_N(\alpha), C_T(\alpha), \dot{\phi}^2, \dot{\theta}^2, \dot{\psi}^2, y(r), c(r)\right) \tag{B.7}$$

where $y(r)$ and $c(r)$ define the position of the leading edge and chord length of the wing as a function of radial position, thus fully defining the planar wing shape. The the reader is referred to [89] for detailed derivation and explanation of the exact form and individual terms in Eqs. B.6 and B.7.

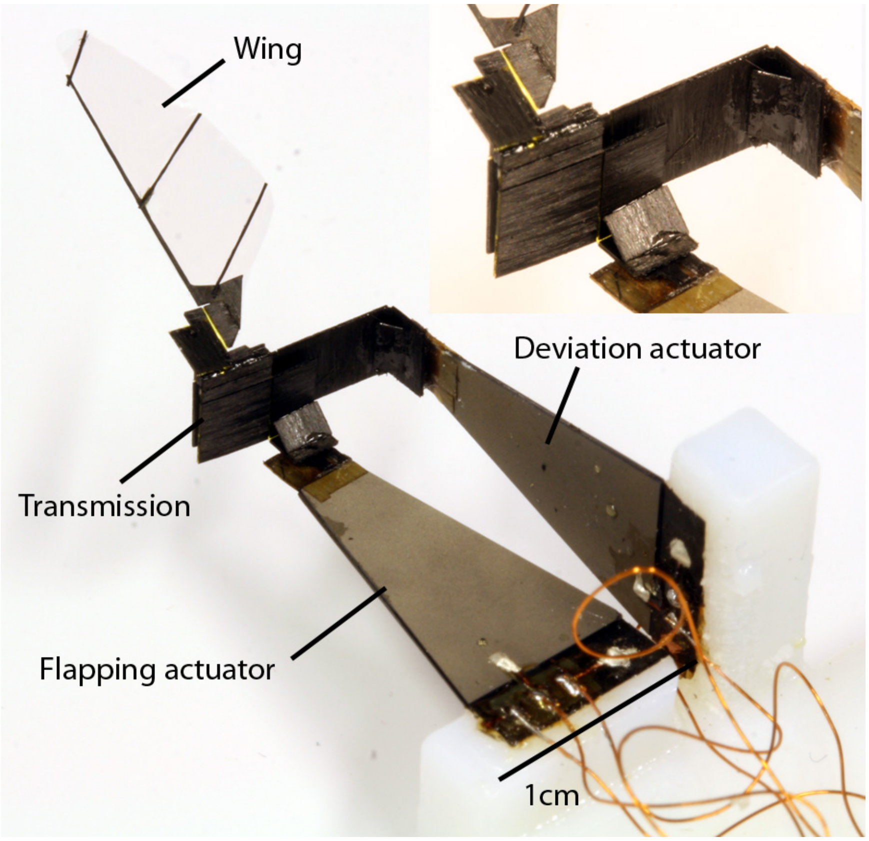

Figure B.8: The test structure used to collect data. Actuator control signals are supplied externally. (inset) A closer view of the transmission.

B.5 Experiment

B.5.1 Methods

A test device using the transmission shown in Fig. B.4 with two externally powered piezoelectric actuators and a wing connected to the output link was constructed (Fig. B.8). Note that on-board power supply and electronics for the HMF are ongoing research areas [53, 54], but not considered for the tests presented here. Piezoelectric actuators were driven with a custom Matlab program (Mathworks Inc.). 0-5V range analog signals output from the computer were amplified to levels required to drive the actuators (200-300V) with a high-voltage amplifier (Trek Inc.). Wing motion was filmed using two Phantom V7.3 high-speed cameras (Vision Research) oriented at approximately 90° to each other. Two-dimensional coordinates of points on the wing were extracted from the left and right camera views separately using 2D motion tracking software (ProAnalyst from Xcitex Inc.). The use of two cameras allowed stereoscopic reconstruction of full three-dimensional wing kinematics [20]. Note that the calibration procedure calculates the relative camera positions and orientations, so the camera positions need not be exactly known *a priori*. Still images from two sample videos are shown in Fig. B.9.

B.5.2 Results

Three trajectory types are tested: flat, oval, and figure-of-eight. Trajectories are driven open-loop with the actuator signals presented in Table B.1. For each trajectory type, the wing angles ϕ, θ and ψ are plotted as functions of time in Figure

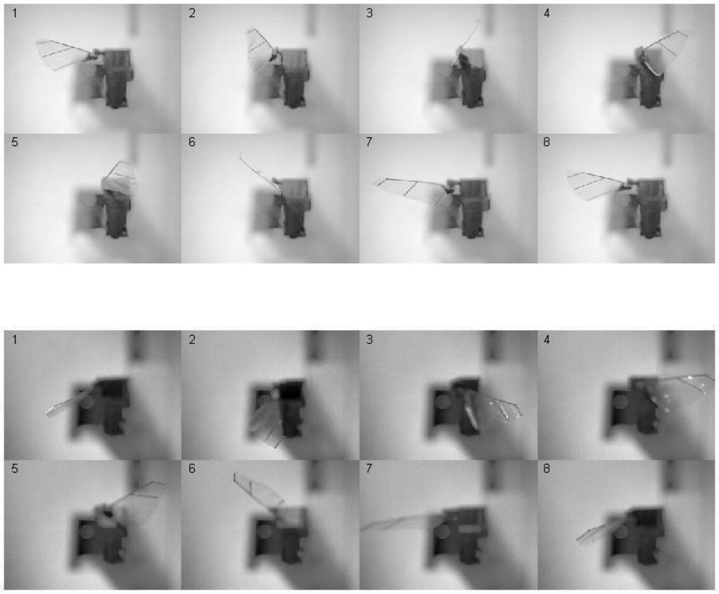

Figure B.9: Still images from one camera for flat (top) and oval (bottom) stroke trajectories. Data was recorded at 5000fps, so 50 data points were collected per cycle flapping at 100Hz. Every 7th frame for one cycle is shown, the time between images is 1.4msec.

B.11, however visualizing the shape of each trajectory is easier when viewing a plot of θ vs. ϕ (Fig. B.10). One can imagine this as approximately the wingtip trajectory that would be seen with an edge-on view of the wing mapped from the surface of a sphere.

It is immediately evident from Fig. B.10 that when driven at high frequencies, the wing trajectories do not match those predicted from kinematics (Fig. B.2). However, when driven at low frequencies - i.e. when aerodynamic and inertial forces are negligible - reasonable flat, oval and figure-of-eight trajectories can be obtained (Fig. B.10b,c,e). There are two possible sources of error. First, the compliance of the stroke-plane-deviation actuator and transmission (k_2 in Fig. B.7) allows undesired vertical motions of the wing due to coupling of the lift force, as there is no feedback

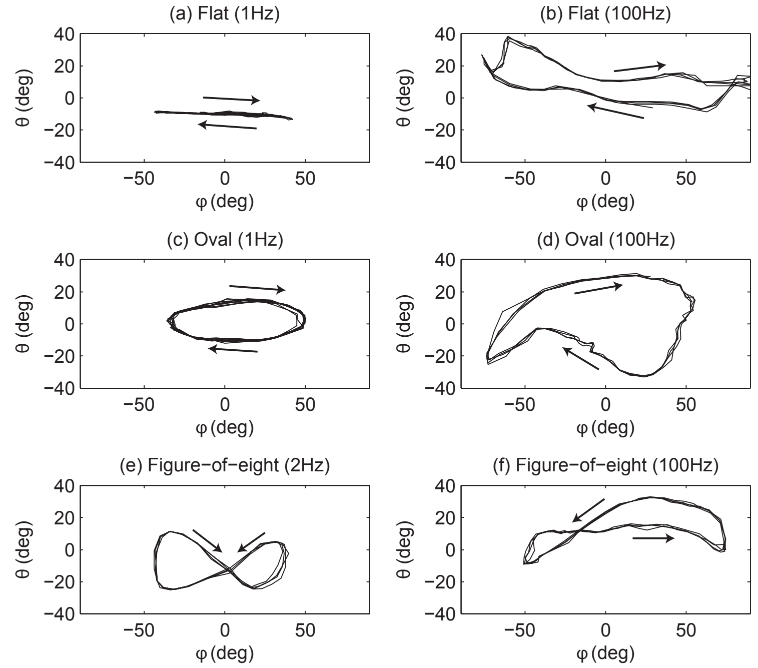

Figure B.10: θ vs ϕ for flat , oval and figure-of-eight trajectories at high and low frequencies. Actuation at low frequencies can achieve kinematically predetermined wing trajectories (left column), while actuation at higher frequencies appears to excite oscillations in the stroke plane deviation direction (right column). Direction of motion is indicated with arrows.

system in place to reject disturbances in this direction. Second, the transmission design relies heavily on the idea that flexure joints will act as ideal revolute joints, with one axis of rotation and infinite off-axis stiffness. In practice this is not true [50], and off-axis compliance of the flexure joints can lead to undesired motion. Future revisions of the design will address both of these issues.

Despite the fact that the observed trajectories are not as consistent as hoped, experimental results can still be compared to the aerodynamic model in [89] in order to make a preliminary comparison of efficiency. The model takes the time history of ϕ and θ as inputs and calculates expected passive rotation ψ and resulting average aerodynamic lift and power. Fig. B.11 shows experimental and predicted passive

Table B.2: Theoretical aerodynamic lift, power and efficiency for three observed wing trajectories

Stroke	Avg. Lift (mN)	Avg. Power (mW)	Lift/Power (N/W)
Flat	2.7	23.2	0.12
Oval	1.59	14.0	0.11
Fig. 8	1.54	10.4	0.15

rotation for the recorded flapping and deviation kinematics. Average lift, average aerodynamic power, and lift/power (all theoretical values, as lift and aerodynamic power are not measured directly) as a measure of efficiency are compared for each trajectory (Table B.2). Despite having the largest value of average lift, the flat trajectory consumes more power and thus has a lift/power ratio roughly the same as the oval trajectory. The figure-of-eight, while it has the lowest lift value, also has the lowest aerodynamic power and therefore the combination of these two terms gives it the best lift/power ratio. However, the data presented here is preliminary and *not* conclusive enough to make the claim that a figure-of-eight stroke is more efficient under all circumstances. Further testing on a larger number of stroke trajectories is required. Automation of testing and data collection, i.e. automatically generating actuator drive signals, collecting force data, extracting wing kinematics, and measuring actuator power consumption will allow a significant increase in the amount of data that can be collected.

B.6 Discussion

The work presented here is intended as a preliminary exploration into actuated stroke-plane deviation for flapping-wing MAVs, specifically the RoboBee, since the

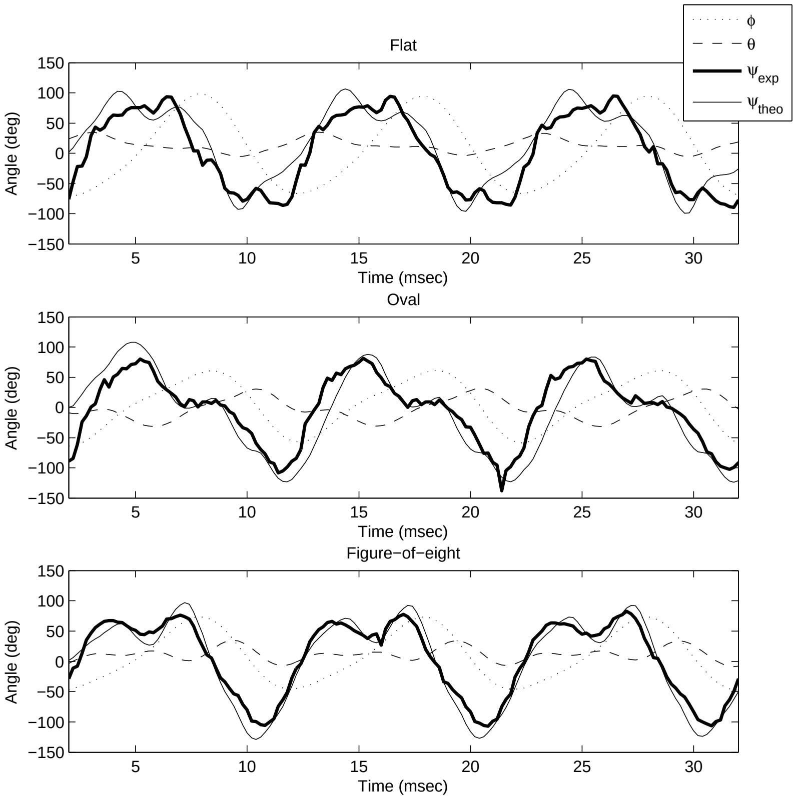

Figure B.11: Experimental flapping and deviation angles ϕ and θ plotted with experimental and theoretical rotation angles ψ_{exp} and ψ_{theo}; for flat, oval and figure-of-eight wingstrokes. There is good agreement between observed and prediction passive wing rotation.

vast majority of MAVs utilize flat stroke planes. While investigated here due to potential gains in efficiency over a flat stroke, stroke plane deviation also has promise for vehicle maneuvering and stability, and this will be the subject of future work. The authors do *not* make the claim that a given trajectory type is more efficient than another based on the preliminary results presented here. Much further work, both theoretical and experimental, will be required to make any claim of an optimal trajectory. Most aerodynamic studies, such as [15] and [89] assume kinematic control of wing flapping and deviation, without considering actuator or transmission dynamics. While the device presented here can achieve direct kinematic control of wing trajectory at low frequencies with no feedback system in place, results at high frequencies show that actuator/transmission dynamics and compliance play a vital role in resultant trajectories and cannot be neglected. Future work will include actuator position feedback in order to follow kinematically predetermined trajectories. Additional experimental measurements may also be made to further evaluate the lift/power criteria. Lift force can be measured directly as in [89, 95] and compared to theoretical values. While it is difficult to experimentally measure aerodynamic power, electrical power input to the actuators can be measured directly and used as a criteria. Additional work in all of these areas will allow development of wing trajectories and thorax designs for increased maneuverability and flight times of insect-sized MAVs.

Appendix C

Optimal energy density piezoelectric twisting actuators

The use of piezoelectric materials as actuators or sensors is widespread, and numerous actuator topologies and models have been developed. However, many of these applications do not place stringent requirements on actuator mass or energy density. Motivated by applications that do have strict requirements in these areas such as flapping-wing microrobots, a torsional piezoelectric actuator is developed. A model is presented that predicts output rotation, torque and energy density values; and allows optimization of these values based on actuator geometry. An emphasis is placed on actuator fabrication and testing for empirical validation of the model.

C.1 Introduction

Piezoelectric actuators are commonly arranged as stacks or benders. Stacks provide small, high precision linear displacements while benders rely upon a cantilever configuration to transform curvatures into displacements (e.g. clamped-free cantilevers [63, 61, 97], "moonies" [32], and disks [87, 62]). Other than a means of applying an electrical field, stacks require no additional structures. Benders require an antagonist to generate a curvature; either an antagonistic piezoelectric layer (in the case of a bimorph) or a passive compliant layer. Twisting actuation has also been achieved through use of anisotropic composite materials or skewed orientation of piezoelectric plates [16, 23]. This paper describes the use of anisotropic passive layers laminated to a piezoelectric material to create a rotational actuator. The rotation is a function of in-plane anisotropy and anti-symmetric layering which combines to exploit extension-twisting coupling. Analytical models of such actuators have been presented previously for varying ply angles [99], here a model is presented which considers ply angles and geometries of the actuator as well as how induced strain from the piezoelectric layer couples into output torque.

The figures of merit of twisting angle and blocked torque are derived and the product is used tto produce rotary actuators with maximal energy density. However, the same modeling procedure can be used to design rotary actuators of any twist-torque value within the constraints allowed by the constituent materials and the converse piezoelectric effect. Using a meso-scale fabrication paradigm [94], we fabricate a variety of actuator geometries and measure twist and torque for model verification. Results prove the validity of the model as well as the value of this class of piezoelectric actuators. Such actuators could be used for a variety of applications from precision micro manipulation to high bandwidth power delivery.

C.2 Actuator Model

Twisting motion is achieved with a single piezoelectric layer by laminating anti-symmetric top and bottom fiber-reinforced composite (FRC) layers (Fig. C.1a). Thus an actuator of length L and width W can achieve a rotation angle of θ_{twist} (Fig. C.1b) by applying a voltage across the piezoelectric layer (for d_{31} mode actuation), using the conductive FRC layers as electrodes (Fig. C.1c). The following section presents derivation of the theory that predicts output twist angle, blocked torque and energy density based on the geometry and arrangements defined in Fig. C.1.

C.2.1 Laminate Plate Theory

The model for a clamped-free piezoelectric cantilever actuator consisting of an arbitrary number of active piezoelectric and passive composite layers in arbitrary orientations is originally presented in [97], derived from the information in [52]. Here we use the same approach to derive the constitutive equations for unimorph twisting actuators.

First, assuming a state of plane stress for each layer (i.e. stresses act only in the

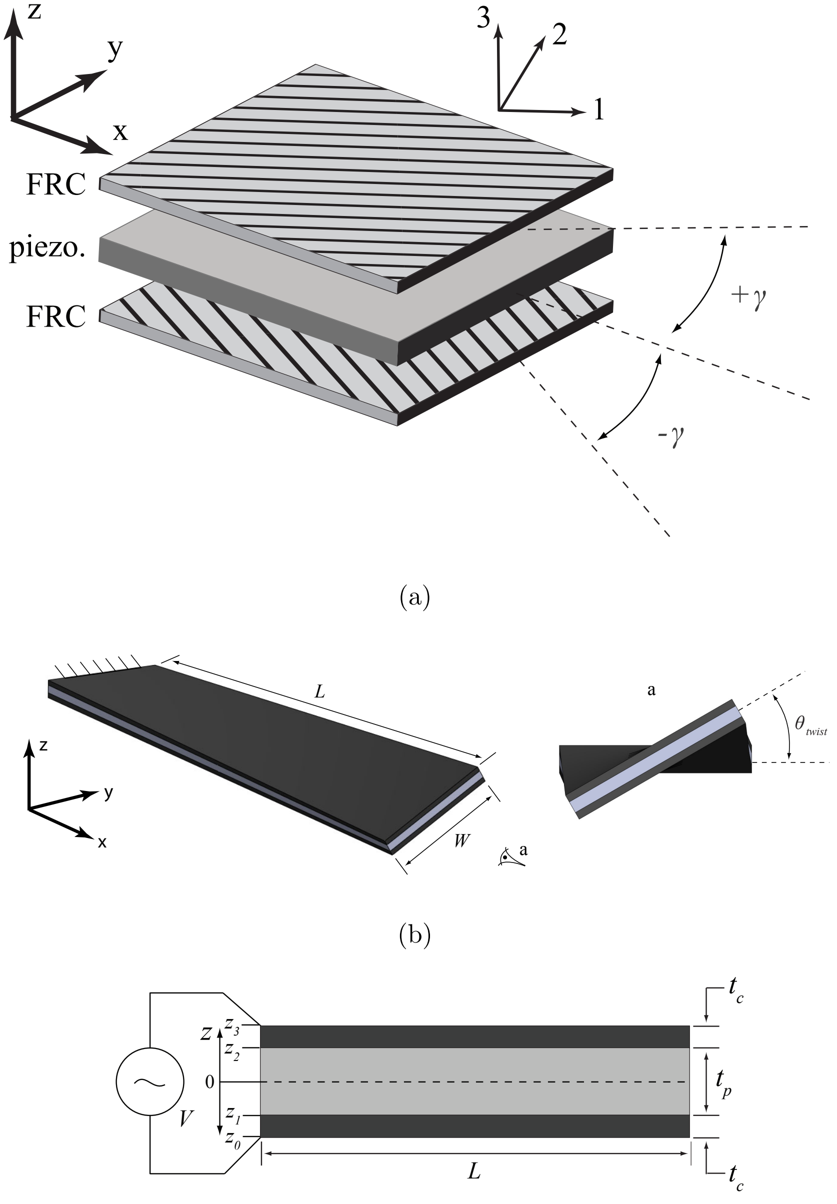

Figure C.1: (a) The fiber directions of the two fiber-reinforced composite (FRC) layers are oriented at angles of $\pm\gamma$ to the longitudinal axis of the actuator. This creates anisotropy in the compliance matrix and allows exploitation of extension-twisting coupling to create a twisting actuator. (b) A three-dimensional and end-on view of a twisting actuator with length L, width W, and twist angle θ_{twist}. (c) A cross-sectional view of an actuator, showing piezo layer thickness t_p, composite layer thickness t_c, the z-axis defined with $z = 0$ at the midplane, and electrical connections to the top and bottom composite layers.

$x - y$ plane since there are no surface tractions), the in-plane stresses are given by

$$\begin{bmatrix} \sigma_1 \\ \sigma_2 \\ \tau_{12} \end{bmatrix} = \begin{bmatrix} Q_{11} & Q_{12} & 0 \\ Q_{12} & Q_{22} & 0 \\ 0 & 0 & Q_{66} \end{bmatrix} \left(\begin{matrix} \epsilon_1 \\ \epsilon_2 \\ \gamma_{12} \end{matrix} - \begin{matrix} d_{31} \\ d_{32} \\ 0 \end{matrix} E_3 \right) \tag{C.1}$$

where the subscripts 1, 2 and 3 correspond to a local coordinate system oriented with the fiber direction (Fig. C.1a), E_3 is the electric field in the piezoelectric layer, and d_{31} and d_{32} are the electromechanical coupling coefficients of the piezoelectric material. Elements of the stiffness matrix $[Q]$ are defined as follows for an isotropic material (the piezoelectric layer in this case):

$$Q_{11} = Q_{22} = \frac{E}{1-\nu^2} \tag{C.2}$$

$$Q_{12} = \frac{E\nu}{1-\nu^2} \tag{C.3}$$

$$Q_{66} = \frac{E}{2(1+\nu)} = G \tag{C.4}$$

where E is the Young's modulus, G is the shear modulus and ν is the Poisson's ratio. For an anisotropic material (the FRC), elements of $[Q]$ are defined as

$$Q_{11} = \frac{E_1}{1-\nu_{12}\nu_{21}} \tag{C.5}$$

$$Q_{12} = \frac{\nu_{12}E_2}{1-\nu_{12}\nu_{21}} \tag{C.6}$$

$$Q_{22} = \frac{E_2}{1-\nu_{12}\nu_{21}} \tag{C.7}$$

$$Q_{66} = G_{12} \tag{C.8}$$

where E_1 is the Young's modulus in the fiber direction, E_2 the modulus in the cross-fiber direction, and the following relationship holds:

$$\frac{\nu_{12}}{E_1} = \frac{\nu_{21}}{E_2} \tag{C.9}$$

To account for arbitrary orientation of anisotropic material layers, the stiffness matrix is modified:

$$\begin{bmatrix} \sigma_x \\ \sigma_y \\ \tau_{xy} \end{bmatrix} = \begin{bmatrix} \bar{Q}_{11} & \bar{Q}_{12} & \bar{Q}_{16} \\ \bar{Q}_{12} & \bar{Q}_{22} & \bar{Q}_{26} \\ \bar{Q}_{16} & \bar{Q}_{26} & \bar{Q}_{66} \end{bmatrix} \left(\begin{matrix} \epsilon_x \\ \epsilon_y \\ \gamma_{xy} \end{matrix} - \begin{matrix} d_{31} \\ d_{32} \\ 0 \end{matrix} E_3 \right) \tag{C.10}$$

where $[\bar{Q}_{ij}]$ is the adjusted stiffness matrix with the property

$$[\bar{Q}_{ij}] = [T]^{-1}[Q_{ij}][T]^{-T} \tag{C.11}$$

with the transformation matrix [T] defined as

$$[T] = \begin{bmatrix} m^2 & n^2 & 2mn \\ n^2 & m^2 & -2mn \\ -mn & mn & m^2 - n^2 \end{bmatrix} \tag{C.12}$$

where $m = \cos(\gamma)$ and $n = \sin(\gamma)$ (Fig C.1a).

To calculate overall deflections (displacements and/or rotations of the output), midplane strains and curvatures are integrated over the appropriate dimension. These strains and curvatures are given by

$$\begin{bmatrix} \epsilon^0 \\ \kappa \end{bmatrix} = \begin{bmatrix} A & B \\ C & D \end{bmatrix}^{-1} \left(\begin{matrix} N^{ext} \\ M^{ext} \end{matrix} + \begin{matrix} N^p \\ M^p \end{matrix} \right) \tag{C.13}$$

where $\epsilon^0 = [\epsilon_x \quad \epsilon_y \quad \epsilon_{xy}]^T$, and $\kappa = [\kappa_x \quad \kappa_y \quad \kappa_{xy}]^T$. A, B and D are elements of the stiffness matrix defined as

$$A_{ij} = \sum_n [\bar{Q}_{ij}]_n \left(z_n - z_{n-1}\right) \tag{C.14}$$

$$B_{ij} = \frac{1}{2} \sum_n [\bar{Q}_{ij}]_n \left(z_n^2 - z_{n-1}^2\right) \tag{C.15}$$

$$C_{ij} = \frac{1}{3} \sum_n [\bar{Q}_{ij}]_n \left(z_n^3 - z_{n-1}^3\right) \tag{C.16}$$

where z_n is the height of the nth laminate layer with respect to the midplane of the structure (Fig. C.1b).

N^{ext} and M^{ext} are the external forces and moments per unit width (i.e. $N = [N_x \quad N_y \quad N_{xy}]^T$, $M = [M_x \quad M_y \quad M_{xy}]^T$), and N^p and M^p are the piezoelectric forces and moments per unit width, defined as:

$$[N_i(E_3)]^p = \sum_n \int_{z_n-1}^{z_n} [\bar{Q}_{ij}]_n d_{3j} E_3 dz \tag{C.17}$$

$$[M_i(E_3)]^p = \sum_n \int_{z_n-1}^{z_n} [\bar{Q}_{ij}]_n d_{3j} E_3 z dz \tag{C.18}$$

Given Eq. C.13, the maximum angle of twist, blocked torque, and energy density can be calculated for a given actuator geometry. The curvature element κ_{xy} is related to the vertical displacement of the actuator z as $\kappa_{xy} = \frac{\delta^2 z}{\delta x \delta y}$, therefore the angle of twist is calculated by evaluating the slope $\frac{\delta z}{\delta y}$ at the end of the beam:

$$\theta_{twist} = \tan^{-1}\left(\frac{\delta z}{\delta y}|_{x=L}\right) \tag{C.19}$$

where L is the actuator length. Given the piezoelectric forces and moments from the converse piezoelectric effect (Eqs. C.17 and C.18) and assuming no external forces and moments, κ_{xy} is calculated from Eq. C.13, and $\frac{\delta z}{\delta y}$ at $x = L$ is calculated by integrating the curvature along the length of the beam:

$$\frac{\delta z}{\delta y}|_{x=L} = \int_0^L \kappa_{xy} dx \tag{C.20}$$

Since κ_{xy} is not a function of x, it is constant along the length of the beam. Combining Eqs. C.19 and C.20 yields a final expression for the angle of twist:

$$\theta_{twist} = \tan^{-1}(\kappa_{xy} L) \tag{C.21}$$

The blocked torque is defined as the external torque required to maintain zero twist angle when the piezoelectric material is activated. For convenience, the matrix C is defined as

$$C = \begin{bmatrix} A & B \\ B & D \end{bmatrix}^{-1} \tag{C.22}$$

From Eq. C.13, assuming only an external M_{xy} is imposed and that piezoelectric moments are zero due to symmetry:

$$\kappa_{xy} = C_{66} M_{xy}^{ext} + C_{61} N_x^p + C_{62} N_y^p + C_{63} N_{xy}^p \tag{C.23}$$

This curvature can be broken down into two components: that due to the external moment and due to the piezoelectric forces. In order to maintain zero total twist, the superposition of these two curvatures must be zero, so Eq. C.23 is used to solve for M_{xy}^{ext} by setting $\kappa_{xy} = 0$, and thus the blocked torque is:

$$\tau_b = -\frac{W}{C_{66}} \left(C_{61} N_x^p + C_{62} N_y^p + C_{63} N_{xy}^p \right) \tag{C.24}$$

where W is the actuator width (noting that M_{xy} is a moment per unit width).

Finally, given a maximum torque and maximum displacement, actuator energy density is calculated as the area under the torque-angle curve, normalized to actuator mass:

$$E_d = \frac{1}{2} \frac{\tau_b \theta_{max}}{m} \tag{C.25}$$

C.3 Experiments

C.3.1 Parameters

The model presented above can be used to design actuators with the best performance characteristics given certain metrics. For example micro grippers or manipulators may require a specific torque or rotation value, or a flying microrobot [93] may require optimal energy density given payload constraints. Several parameters of interest that can be varied experimentally are selected, namely

- Fiber layer orientation γ
- Actuator width W and length L
- Fiber layer thickness t_c

and the effects of varying these parameters on the following performance characteristics are examined:

- Output twist angle θ_{twist}
- Blocked torque τ_b
- Energy density E_d

These values can be calculated numerically with Eqs. C.21, C.24 and C.25 respectively, and are compared to experimentally measured values. There are many additional experimental possibilities, such as application of an external load to determine actuator stiffness, frequency-domain analysis to determine resonant behavior, or use of a dynamometer to measure hysteresis effects, however those are beyond the scope of this work. A brief discussion of actuator fabrication and the experimental setup is presented here.

C.3.2 Fabrication

Actuators are fabricated using the techniques presented in [94]. Raw materials are cut with a custom-built laser micromachining system (355nm diode-pump solid state laser, Photonics Industries DC150H-355). Laser cut-files are made with a 2D CAD program (DWGEditor, Dassault Systems) and the laser system is operated with ProLase XP (American Laserware Inc.). Rectangular pieces of desired length, width, and angle in the case of the composite layer, are cut from bulk piezoelectric and carbon fiber composite sheets available in discrete thicknesses from the manufacturer (PZT-5H from Piezo Systems Inc. and M60J from Toray America respectively). Two carbon fiber layers and one piezoelectric layer are stacked to form the layup shown in Fig. C.1 and vacuum bagged. The carbon fiber is pre-impregnated with a heat-curing epoxy, and the structure is cured under heat and pressure (with a Cascade TEK TFO-1 oven), bonding the layers together.

C.3.3 Experimental Setup

Actuator blocked torques (torque at zero rotation) were measured in a clamped-clamped configuration with a 6-axis Nano 17 force/torque sensor (ATI Industrial Automation). Data was recorded with data acquisition (DAQ) hardware and software supplied by ATI with the Nano17. Custom mechanical mounts were used to connect the actuators to mechanical ground and to interface with the sensor, and an XYZ micrometer stage and Labjack (Thorlabs Inc.) were used to allow precise alignment of the actuator's axis of rotation with the sensor's Z-axis. A custom Matlab script was used to generate actuator control signals which were conditioned through a high-voltage amplifier (Trek Inc.). The actuators were driven open-loop with no feedback. For information on feedback control of a voltage-driven piezoelectric actuator attached to a load, see [72].

Angle of twist was measured in a clamped-free configuration, using 2D motion tracking software (ProAnalyst, Xcitex Inc.) to calculate θ_{twist} from an edge-on view of the actuator (videos recorded with a PixeLink camera). A photograph and diagram of the experimental setup are shown in Fig. C.2.

C.4 Results

C.4.1 Fiber orientation

For fiber orientation tests, we expect a change in extension-twisting coupling due to changes in the compliance matrix (Eq. C.22). These compliance changes give rise to varying torque/displacement to voltage relationships as predicted in Sec. 2.1. For a fixed actuator width of $W = 2$mm, length of $L = 10$mm, and fiber layer thickness of $t_c = 80\mu$m, the orientation of the fiber layer was varied from 0 to 90 degrees. Test actuators were fabricated with 15 degree intervals in orientation (0, 15, 30, 45, 60, 75, 90), and the experimental results are compared to predictions in Fig. C.3. The theoretical model predicts maximum performance at $\gamma = 45°$, with zero twist and torque at $\gamma = 0°$ and $\gamma = 90°$ (consistent with other models [99]). While the the model over-predicts rotation angle and under-predicts torque, the important figure of merit is that the experimental results follow the theoretical trend with maximum performance at $\gamma = 45°$.

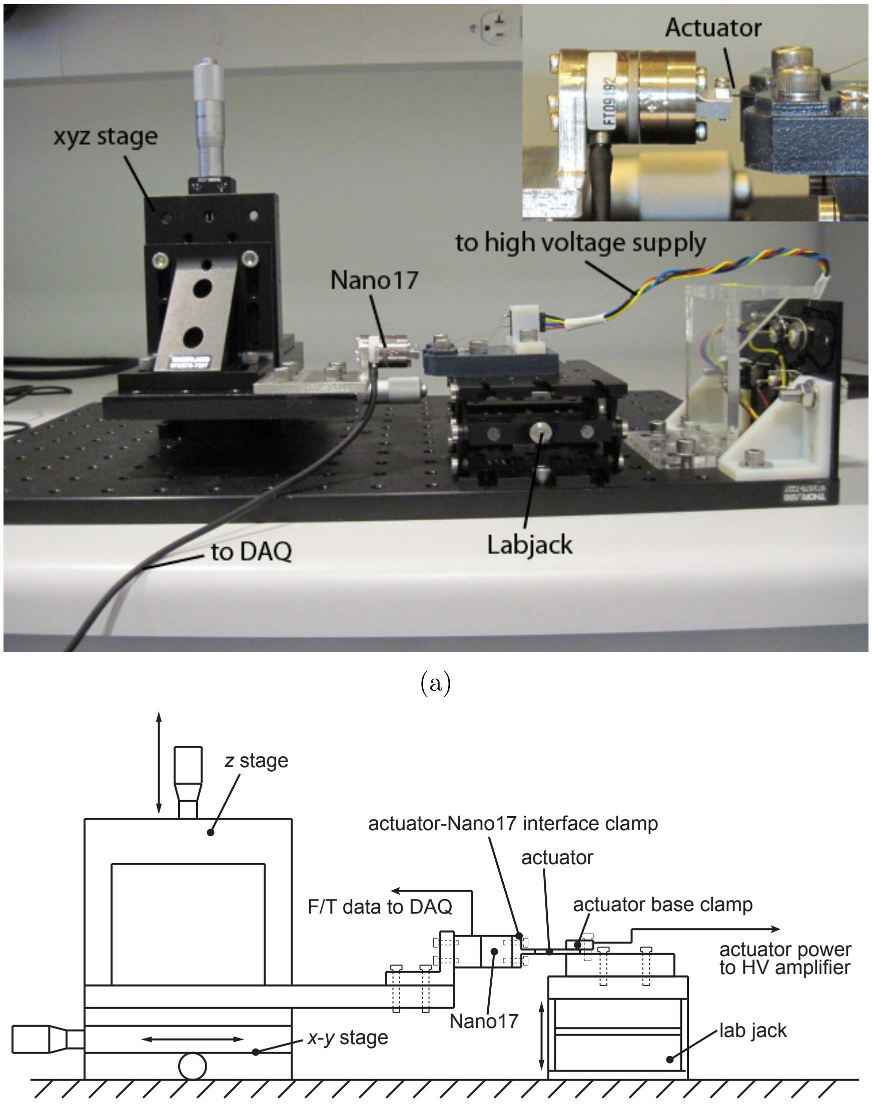

(a)

(b)

Figure C.2: (a) Photograph of experimental setup and (b) labeled diagram (not to scale).

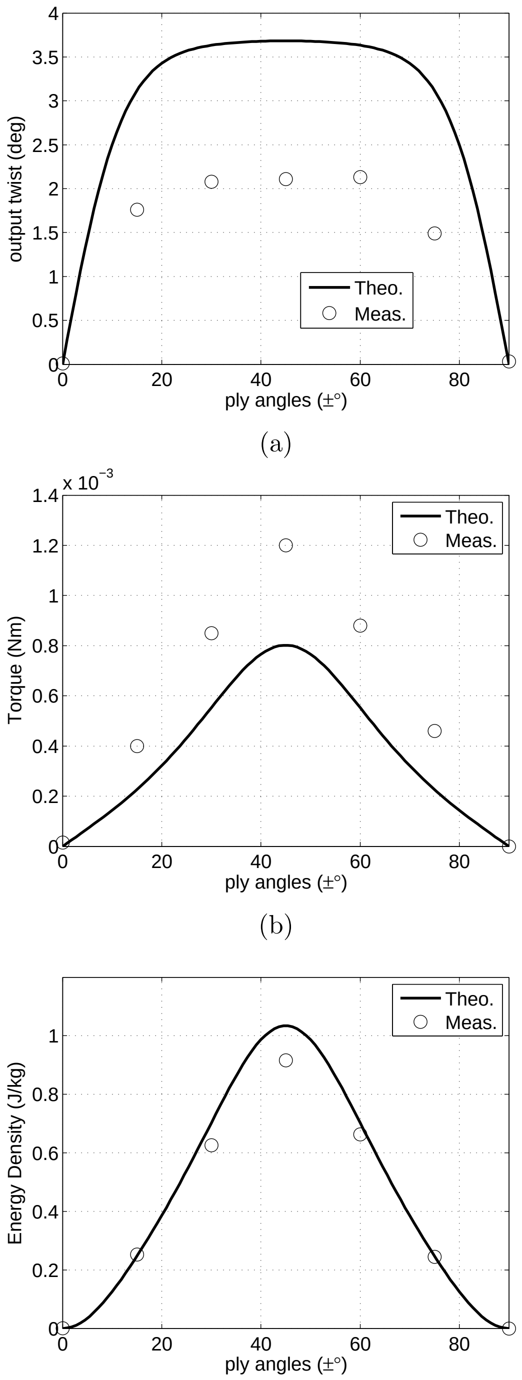

(a)

(b)

(c)

Figure C.3: (a) Theoretical and measured actuator rotation vs. fiber layer orientation, (b) blocked torque vs. fiber orientation, and (c) energy density vs. fiber orientation. The maximum performance occurs at $\gamma = 45°$.

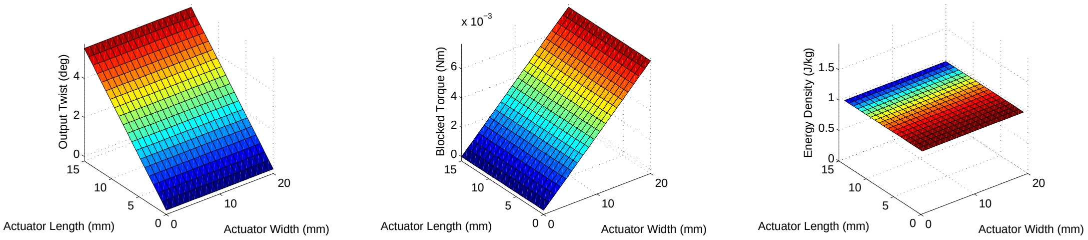

(a) (b) (c)

Figure C.4: (a) Actuator rotation vs. length and width, (b) blocked torque vs. length and width, and (c) energy density vs. length and width. All values are theoretical.

C.4.2 Aspect ratio

Having determined that the optimal fiber orientation is 45°, actuator length L and width W were varied for a fixed $\gamma = 45°$ and fiber thickness of 80μm. The model predicts that actuator rotation scales linearly with length but is independent of width, and vice versa for torque, leading to an energy density that is independent of both length and width (Figure C.4). The constant energy density is roughly 1.0J/kg assuming an applied electric field of 1.57V/μm (200V applied across 127μm thick piezoelectric layer). Compare this to 0.15J/kg for a typical commercially available piezoelectric bending actuator [3] and 4.0J/kg as the maximum strain energy density for a bulk free plate of piezoelectric material [97]. Increasing the applied field to 2.36V/μm (300V across the same thickness) increases the predicted energy density to over 2.0J/kg, consistent with the results for bending actuators in [97]. Actuators of discrete lengths $L = 5$, 10 and 15mm and widths $W = 2$, 4 and 6mm were tested. The experimental results, presented in Figure C.5, confirm that rotation depends only on length and torque depends only on width.

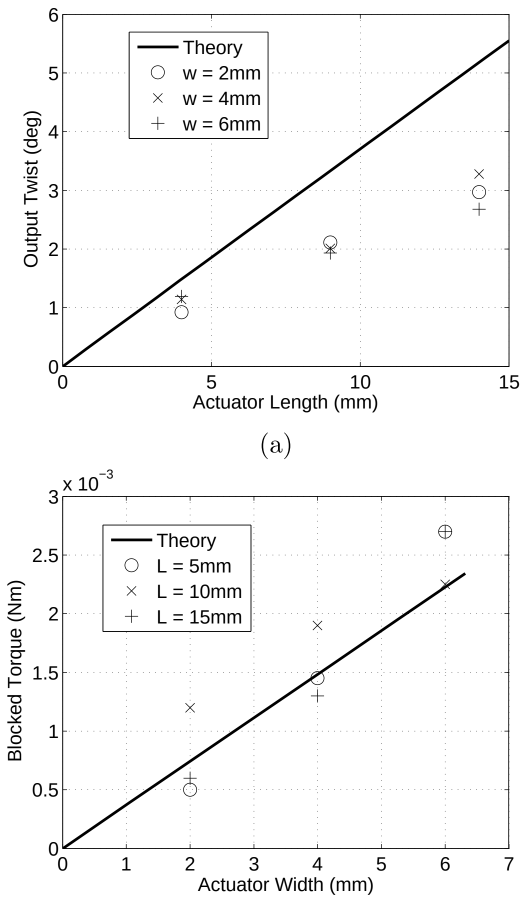

(a)

(b)

Figure C.5: (a) Actuator rotation vs. length and (b) blocked torque vs. width.

C.4.3 Fiber layer thickness

Finally, the effect of varying fiber layer thickness was investigated. Ability to manufacture actuators with variable thickness fiber layers is limited by the availability of materials from the manufacturer in discrete thicknesses (integer multiples of the thickness of a single sheet of material can be achieved by laminating multiple composite layers). As seen in Figure C.6, there is a theoretical maximum rotation around $t_c = 25\mu$m, however carbon fiber sheets of this thickness were not available. Blocked torque increases indefinitely with increasing fiber thickness. Energy density depends on the product of these two terms, and Figure C.6c shows that the rotation term dominates, i.e. the energy density has a global maximum and then decreases to zero. Fortunately this maximum occurs close to the range of commercially available thicknesses (50-80μm).

C.4.4 Optimal Performance

The analytical and empirical analyses determine fiber layer orientation γ and composite thickness t_c to be the most influential parameters when the primary performance criteria is energy density. Energy density is independent of actuator length and width, but since twist angle and torque scale linearly with these two values respectively, they can be adjusted as needed for the intended application.

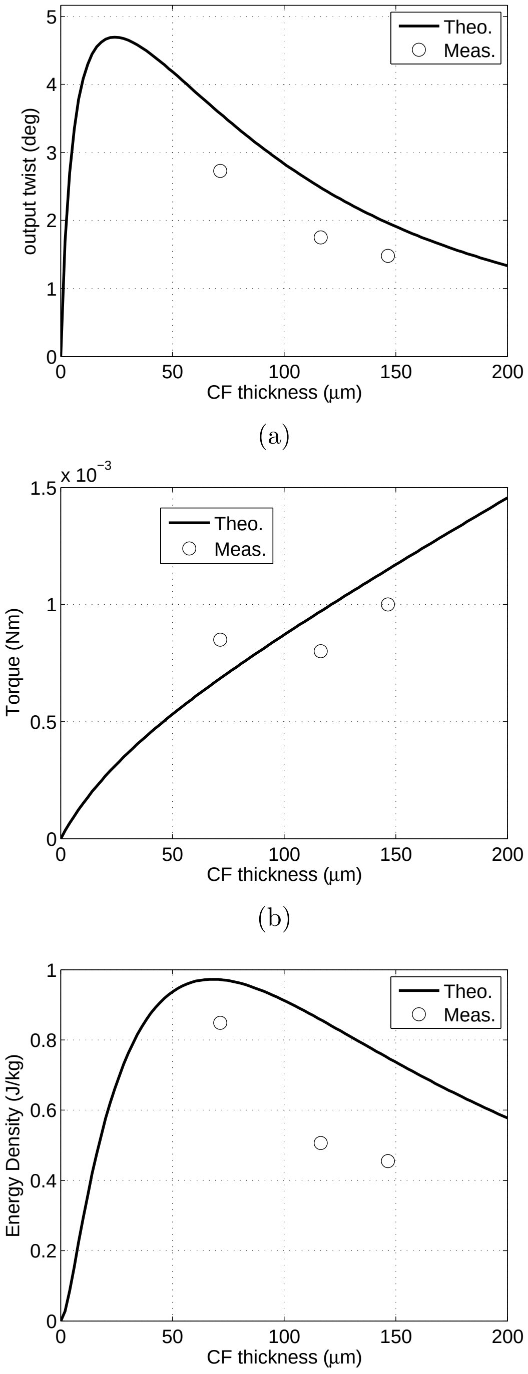

(a)

(b)

(c)

Figure C.6: (a) Actuator rotation vs. carbon fiber layer thickness, (b) blocked torque vs. thickness, and (c) energy density vs. thickness.

C.5 Discussion

We have presented a theoretical model for a piezoelectric twisting actuator that utilizes an antisymmetric composite layup to exploit extension-twisting coupling. The model is used to predict actuator performance based on geometric parameters that can be varied experimentally, and these predictions are consistent with previous models. More importantly, empirical validation of the model shows that physical actuators do indeed have similar twist, torque and energy density magnitudes and follow trends predicted by the model for variation of geometric parameters. Actuator twist and torque are shown to scale linearly with length and width respectively, while both of these quantities are maximized at a composite layer orientation of $\pm 45°$. Energy density is shown to be independent of length and width but is maximized for composite orientation of $\pm 45°$ and composite layer thickness of 70μm, allowing optimization of energy density, which will be essential to high-performance, demanding applications.